FIELD EMISSION ELECTRON SOURCE BASED ON SILICON CARBIDE NANOPILLARS

A Thesis Submitted to
Graduate School of Engineering and Sciences of
İzmir Institute of Technology
in Partial Fulfilment of the Requirements for the Degree of

MASTER OF SCIENCE

in Materials Science and Engineering

by
Damla YEŞİLPINAR

July 2017
İZMİR

We approve the thesis of **Damla YEŞİLPINAR**

Examining Committee Members:

Assoc. Prof. Dr. Cem ÇELEBİ
Department of Physics
İzmir Institute of Technology

Asst. Prof. Dr. Gökhan UTLU
Department of Physics
Ege University

Asst. Prof. Dr. Umut ADEM
Department of Materials Science and Engineering
Izmir Institute of Technology

30.05.2017

Assoc. Prof. Dr. Cem ÇELEBİ
Supervisor, Department of Physics
İzmir Institute of Technology

Prof. Dr. Mustafa Muammer Demir
Co-advisor, Department of Materials
Science and Engineering
İzmir Institute of Technology

Prof. Dr. Mustafa Muammer Demir
Head of the Department of Materials
Science and Engineering

Prof. Dr. Aysun SOFUOĞLU
Dean of the Graduate School of
Engineering and Sciences

ACKNOWLEDGEMENTS

I would like to express my gratitude to my advisor Assoc. Prof. Dr. Cem Çelebi for accepting me as a M.Sc. student, giving me a chance to study with brilliant people in the Quantum Device Laboratory, his invaluable advice and his support throughout this thesis work. I would like to thank every member of the Quantum Device Laboratory for their endless support throughout this research. I would also like to thank Dilce Özkendir for her artsy SEM images, for never letting me down whenever I needed SEM measurements and of course for her invaluable help in optimizing the nanosphere self-assembly procedure; and also to thank Sırrı Batuhan Kalkan for his help building the experimental set-up for the field emission experiments, without his expertise, it would have been much harder to obtain these results. During this thesis work, I have had the chance to work with Dr. Cenk Yanık from Sabancı University for the ICP-RIE processes. I would like to thank him for his inestimable knowledge and help throughout the etch processes.

I would like to acknowledge the financial support from Scientific and Technological Research Council of Turkey (TÜBİTAK) for this thesis.

Lastly, I would also like to thank my family, who always supported me in every aspect of my life, for their love and patience.

ABSTRACT

FIELD EMISSION ELECTRON SOURCE BASED ON SILICON CARBIDE NANOPILLARS

In this thesis work, I studied the fabrication and the field emission characteristics of SiC nanopillar based electron field emitters. The first objective of this thesis was to fabricate a large area nanopillar array on bulk 6H-SiC substrate. Accordingly, a nanosphere assisted technique was developed to create a conventional Cr/Ni hard mask to acquire desired etch mask pattern on the C-terminated face of 6H-SiC. The nanopillars were then fabricated by ICP-RIE. Two sets of nanopillars with different aspect ratios and geometries were fabricated for two different ICP-RIE durations. 1 min long etch resulted in nanopillar arrays with blunt tip apex and an aspect ratio of 3.4, where 2 min long etch produced nanopillar arrays with an aspect ratio of 4.9 and a sharp tip apex with an estimated radius of curvature of about 18 nm.

As the second objective; the electron field emission characteristics of the produced nanopillars with two different aspect ratios and geometries were investigated and the obtained results were compared with each other. We found that the nanopillars with sharp tip apex produced field emission currents up to 240 $\mu A/cm^2$ under 17.4 V/μm applied electric field, as the nanopillars with blunt tip apex produced an emission current of 70 $\mu A/cm^2$. The threshold electric fields were found to be 9.1 V/μm and 7.2 V/μm for the nanopillars with blunt and sharp tip apex, respectively. Time dependent stability measurements yielded stable electron emission without any abrupt change in the respective current levels of both samples.

ÖZET

SİLİSYUM KARBÜR NANOSÜTUN BAZLI ALAN EMİSYON ELEKTRON KAYNAĞI

Bu tez çalışmasında Silisyum Karbür nanosütun bazlı elektron alan emisyon kaynağının fabrikasyonu ve alan emisyon karakteristiklerini inceledim. Bu tezin ilk amacı, 6H-SiC alttaşının üzerinde geniş alan nanosütun dizilerinin oluşturulmasıydı. Bu nedenle, nanoküre litografisine dayanan bir teknik geliştirilerek konvansiyonel Cr/Ni sert aşındırma maskesinin istenen dizilimde 6H-SiC alttaşın C-termine yüzünde oluşturulması sağlandı. Daha sonra nanosütunlar ICP-RIE işlemi ile üretildi. Farklı boy-en oranına ve uç şekillerine sahip olan iki set örnek, farklı sürelerde ICP-RIE uygulanarak elde edildi. 1 dakika boyunca aşındırılan örnekte nanosütunların boy-en oranının 3.4 olduğu ve düz bir uç noktasına sahip olduğu görüldü. 2 dakika boyunca aşındırılan örnekte nanosütunların yaklaşık 18 nm eğrilik yarıçapına sahip ve keskin uca sahip olduğu, boy-en oranlarının ise 4.9 olduğu görüldü.

İkinci amaç olarak, elde edilen farklı boy-en oranına ve geometriye sahip iki set nanosütunun elektron alan emisyon karakteristikleri incelendi ve elde edilen sonuçlar birbirileri ile karşılaştırıldı. Keskin uca sahip nanosütunların 17.4 V/μm elektrik alan altında 240 $\mu A/cm^2$ akıma ulaştığı, düz uca sahip nanosütunların ise bu elektrik alan değerinde 70 $\mu A/cm^2$ akım ürettiği görüldü. Eşik elektrik alan değerleri düz uca sahip örnek için 9.1 V/μm, keskin uca sahip örnek için 7.2 V/μm olarak bulundu. Zamana bağlı durağanlık ölçümleri kararlı bir alan emisyon akımı elde edildiğini gösterdi; alan emisyon akımınlarında ani bir değişim gözlenmedi.

TABLE OF CONTENTS

LIST OF FIGURES viii

LIST OF TABLES xii

LIST OF ABBREVIATIONS xiii

CHAPTER 1. INTRODUCTION 1
1.1. Field Emission Electron Sources 1
1.1.1. Applications of Field Emitters 3
1.1.2. Designing Field Emitter Structures 5
1.2. Silicon Carbide 7
1.2.1. Crystal Structure and Polytypes of Silicon Carbide 8
1.2.2. Properties of Silicon Carbide 10
1.3. Outline 11

CHAPTER 2. FIELD EMISSION PHENOMENON 12
2.1. Fowler-Nordheim Tunnelling 12
2.1.1. Field Enhancement 14
2.2. Field Emission from Semiconductors 15
2.2.1. Image Charge Effect in Semiconductors 19
2.3. Field Emission from Silicon Carbide Nanostructures 20

CHAPTER 3. FABRICATION OF SiC NANOPILLARS 24
3.1. Nanosphere Lithography Fabrication Technique 24
3.2. Fabrication of SiC Nanopillars by Nanosphere Assisted Etch Mask 27
3.2.1. Step One: Self-Assembly of PS Nanospheres on C-Terminated Face of 6H-SiC 30
3.2.1.1. Effects of Particle Concentration 39
3.2.1.2. Effects of Spin Coating Parameters 40
3.2.2. Step Two: Modification of PS Nanosphere Diameter 41
3.2.3. Step Three: Preparation of Gold Template 44
3.2.4. Step Four: Evaporation of Cr/Ni Etch Mask Material on Au Template 48

3.2.5. Step Five: Removal of the Template and the Production of the Cr/Ni Etch Mask 49
3.2.6. Step Six: Fabrication of 6H-SiC Nanopillars by Inductively Coupled Plasma Reactive Ion Etching Technique 51

CHAPTER 4. FIELD EMISSION FROM SiC NANOPILLARS 56
4.1. The Experimental Set-up 56
4.2. Field Emission Measurements of SiC Nanopillars 60
4.3. Results and Discussion 66

CHAPTER 5. CONCLUSIONS 68

REFERENCES 70

LIST OF FIGURES

Figure **Page**

Figure 1. The schematic illustration of a field emission electron source. A cathode that emits electrons into the vacuum and an anode that collects the emitted electrons. 2

Figure 2. (a) The schematics of CNT FED panel by Samsung (b) The SEM image of the CNT emitters used for FED (c) The FED prototype made by Samsung (Source: Choi, Chung, Kang, et al. 1999) 4

Figure 3. (a) The hexagonal basal plane of SiC crystal (b) The model of a SiC molecule (c) SiC molecule 180° rotated with respect to its initial state.......... 8

Figure 4. Representations of stacking orders for topmost popular polytypes of SiC (Source: E. Kusdemir 2015).......... 9

Figure 5. The schematic illustration of the potential barrier of a metal (a) without external electric field (b) under high external electric fields 12

Figure 6. The schematics, simplified band diagrams and charge carrier concentrations for (a) intrinsic (b) n-type (c) p-type semiconductors in equilibrium conditions (Source: Sze 1981).......... 16

Figure 7. Schematics of a simplified model for electron field emission from semiconductors.......... 18

Figure 8. The band bending effect in an n-type semiconductor (a) for low electric fields (b) for high electric fields.......... 19

Figure 9. SiC NW based field emitters acquired by bottom-up methods (a) β-SiC nanowires (Source: Shen et al. 2006), (b) α-SiC nanorods (Source: T. H. Yang et al. 2003) (c) β-SiC nanorods (Source: X. T. Zhou et al. 2000), (d) Needle-shaped SiC (Source: Z. S. Wu et al. 2002) (e) Aligned SiC porous NWs (Source:Y. Yang et al. 2008) (f) Quasi-aligned β-SiC NWs (Source: X. Zhang et al. 2010) 21

Figure 10. SEM images of different SiC emitter structures reported by Kang et. al (a) mesa structure (scale bar 50 μm) (b) fin array (scale bar 4 μm) (c) pillar arrays (scale bar 10 μm) (Source: Kang et.al. 2012) 22

Figure 11. A typical schematic illustration of NSL lithography (a) Nanospheres used as an etch mask (b) Nanospheres used as a template.......... 25

Figure 12. The diameter reduction of nominally 200 nm PS nanospheres via oxygen plasma treatment reported by Zhang et. al. (Source:Y. J. Zhang, Li, and Chen 2008) (a) 0 sec (b) 30 sec (c) 45 sec (d) 60 sec 27
Figure 13. PS nanospheres as the etch masks for aggressive etch procedures of robust structures (a) 1 min after SF_6 plasma etching (b) 5 min after SF_6 plasma etching 28
Figure 14. Nanosphere assisted fabrication steps for silicon carbide nanopillar structures 29
Figure 15. Schematic representation of spin coating process (a) dropping the solution on the substrate (b) spin coating (c) self-assembly of monolayer PS nanospheres (d) Large area self-assembly pattern after spin coating process (inset) the hexagonal packing of the PS nanospheres and the unit cell. The sample was prepared at Quantum Device Laboratory and SEM measurements were done at the Centre for Materials Research in IZTECH.. 31
Figure 16. (a) Our plasma system (Diener Zepto RIE, 50 W) in the Quantum Device Laboratory (b) The gas inlets on the lid (c) Schematic representation of an RIE system 33
Figure 17. (a) Polos SPIN 150i Spin Coater System in the Quantum Device Laboratory (b) 6H-SiC sample placed inside the spin coater 35
Figure 18. (a) Large area optical microscope image of the sample surface (b) the grain boundaries (c) a small multilayer formation (d) crystal lattice defects 37
Figure 19. SEM measurements at different magnifications taken from the self-assembly structure formed on C-terminated face of 6H-SiC 38
Figure 20. Optical microscope images of the surface concentration of the spheres after spin coating the solution with an initial suspension:ethanol volume ratio of (a) 1:2 (b) 1:1 (c) 3:1 (d) 7:1 (e) 1:0 39
Figure 21. Optical microscope image of the surface of (a) Sample 1 (b) Sample 2 (c) Sample 3 41
Figure 22. SEM images of the nanospheres after (a) 0 sec (b) 150 sec (c) 300 sec (d) 450 sec of O_2 plasma treatment. 42

Figure 23. The change of PS nanosphere diameter as a function of O_2 plasma exposure time. 43
Figure 24. NVTH-350 Thermal Evaporation System in Quantum Device Laboratory (a) the system as a whole (b) inside the vacuum chamber 44
Figure 25. (a) The schematics of Au template production (b) Optical microscope image of Au coated PS nanospheres on the C-terminated face of 6H-SiC (c) After 90 sec of sonication (d) SEM image of the Au template.......... 47
Figure 26. The (a) optical microscopy and (b,c,d) SEM images of Cr/Ni nanoisland based shadow mask on the 6H-SiC surface. 50
Figure 27. Oxford PlasmaLab 100 ICP 300 ICP-RIE System in Sabancı University Nanotechnology Research and Application Center (SUNUM) used for dry anisotropic etching of 6H-SiC based samples retaining Cr/Ni nanoisland hard mask on their surfaces 53
Figure 28. The SEM images taken with 70° angle fom (a) sample etched for 60 sec (NPL) low magnification (b) the sample surface of NPH at high magnification (c) sample etched for 120 sec at high magnification. 54
Figure 29. UHV system in Quantum Device Laboratory (a) The vacuum chamber (b) The pumps (c) The controller unit. 56
Figure 30. The schematic illustration of the sample stage for the electron field emission characterization of SiC nanopillar array (a) top view (b) side view.......... 57
Figure 31. (a) The PTFE sample stage retaining the two electrodes (b) The feedthrough with the sample stage (c) The feedthrough mounted inside the UHV chamber (d) The view of the sample inside the UHV chamber from the viewport. 58
Figure 32. (a) The schematics and (b) the actual picture of the experimental set-up that was constructed for conducting the field emission experiments. 59
Figure 33. The change in the field emission current density with respect to the applied electric field for NPL and NPH samples. 61
Figure 34. FN characteristics of the NPL and NPH samples. (Inset) Step like change observed between electric field values 8.7 V/µm and 9.1 V/µm. 62

Figure 35. Time dependent measurements of the field emission current stability for NPL and for NPH samples acquired under an applied electric field of 8.7 V/μm. 65

LIST OF TABLES

Table: **Page:**

Table 1. Crystal structure parameters of 3C-, 4H- and 6H-SiC 9

Table 2. Comparison of SiC and other semiconductors (Harris 1995) 10

Table 3. The field emission properties of different SiC based NWs (Source: X. Zhang et. al. 2010) 21

Table 4. The electron field emission characteristics of etched SiC micro-structures presented in Figure 10. 22

Table 5. Optimized O_2 plasma treatment parameters for surface hydrophilicity of C-terminated face of 6H-SiC wafers. 35

Table 6. The spin coating parameters for self-assembly of 450 nm PS nano-spheres on C-terminated face of 6H-SiC wafer 37

Table 7. The spin coating parameters used for the samples 41

Table 8. The statistics on the diameters of the nanospheres after the oxygen plasma treatment up to 3 sets. 42

Table 9. The Au evaporation parameters 47

Table 10. The oxygen plasma treatment parameters for surface cleaning. 48

Table 11. Evaporation parameters for Cr and Ni 48

Table 12. Statistical data on the Cr/Ni nanoislands 50

Table 13. The ICP-RIE parameters used to fabricate the nanopillar structures on the surface 53

Table 14. The statistical data obtained from the SEM images of nanopillars 54

Table 15. The slopes and the corresponding field enhancement factors for NPL and NPH samples 63

Table 16. The statistical data obtained from the stability measurements of the NPL and NPH samples for a duration of 3 hours. 65

LIST OF ABBREVIATIONS

Abbreviation	Description
1D	One Dimensional
2D	Two Dimensional
CB	Conduction Band
CNT	Carbon Nanotube
CRT	Cathode Ray Tube
EBL	Electron Beam Lithography
NPH	Nanopillar High
NPL	Nanopillar Low
NSL	Nanosphere Lithography
NW	Nanowire
FED	Field Emission Display
FN	Fowler-Nordheim
HE	High Electric Field
ICP-RIE	Inductively Coupled Plasma Reactive Ion Etching
IMG	Inverted Magnetron Gauge
IPA	Isopropanol
LCD	Liquid Crystal Display
LE	Low Electric Field
MEMS	Microelectromechanical System
MOSFET	Metal-Oxide-Semiconductor Field Effect Transistor
PLA	Polylactide
PMMA	Poly-methyl-methacrylate
PS	Polystyrene
RF	Radio Frequency
RIE	Reactive Ion Etching
SEM	Scanning Electron Microscope
TMP	Turbo Molecular Pump
UHV	Ultra High Vacuum
VB	Valance Band

CHAPTER 1

INTRODUCTION

1.1. Field Emission Electron Sources

Electron field emission is the phenomenon where the electrons are injected into the vacuum in the presence of high electrical fields. This purely quantum mechanical effect arises from the fact that the probability of finding an electron out of the material becomes a finite number due to bending of the potential barrier by the applied field. In other words, the electrons do not jump over, but tunnels through the bent potential barrier. Field emission electron sources differ from other electron sources, such as thermionic electron sources and photoemission electron sources in this aspect. In the latter two, extra energy is given to the electrons, such as heat or photons, and the electrons with higher energy jump over the potential barrier to free from the material into the vacuum. The field emission phenomenon will be discussed in detail in the following chapter of this thesis work.

Since their discovery, cathode ray tubes (CRTs) based on thermionic emission sources have found a wide variety of applications including but not limited to television and radio. But their high operating temperature and voltage, large size and high power consumption have proved these devices impractical over time, and other solid-state devices took their place over in the last decades in the direction of new trends in the technology for going thinner, smaller and above all, more energy efficient. However, relatively poor operation speed and radiation instability of solid-state devices have turned attention back to vacuum micro- and nano-electronics, especially for devices that will work in harsh environments, such as space or the nuclear plants. The desirable properties of field emission electron sources by all these means, and for both single emitters and field emission arrays, have attracted immense attention in order to integrate these novel electron sources into today's technology.

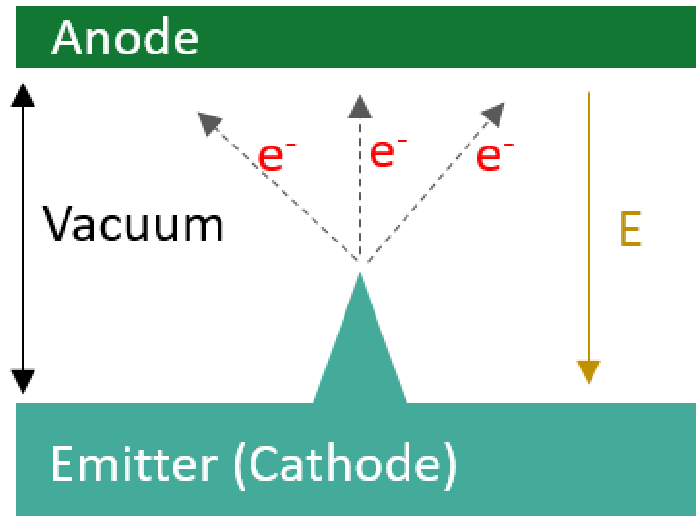

Figure 1. The schematic illustration of a field emission electron source. A cathode that emits electrons into the vacuum and an anode that collects the emitted electrons.

Figure 1 illustrates the basic schematic of field emission electron sources. Electric field is applied between the emitter and the anode, and the electrons tunnel from the emitter tip into the vacuum, where the potential barrier distortion is the highest due to field enhancement properties of sharp structures. Owing to the advances in fabrication processes today, such structures can be created in the range of millimetres or even smaller. Thus giving the field emission electron sources desirable dimensions to be integrated into novel technological devices, such as thin flat panel displays.

Other than the small dimensions, perhaps the most striking property of field emitters is the lack of need of elevated temperatures unlike thermionic sources, since the tunnelling mechanism does not require electrons to have more energies to overcome the potential barrier. This fact allows field emitters to work in room temperature or even below and makes them more suitable for applications where high temperatures are unfavourable. Furthermore, the ability to function at room temperature inside the vacuum promotes the emitter's lifetime and makes them more tolerant to radioactivity and heat exposure during operation.

Field emission electron sources also have higher efficiency when compared to thermionic and photoemission electron sources, since the energy dissipation does not occur during the tunnelling process. In addition, the momentum, energy and spatial spread of the emitted electrons has a narrower band, which is a desirable aspect for high

resolution electron microscopy measurements. Not only field emitters are capable of producing very high current densities but also they allow high frequency and fast operations due to the fact that the electrons move faster in the vacuum than inside a solid material.

All these high-end qualities have attracted researchers all around the globe to investigate the field emission properties and to design field emitters that could replace the conventional thermionic emitters, as well as some solid-state devices currently being used.

1.1.1. Applications of Field Emitters

One of the many possible application areas of field emitter arrays is flat panel displays, which currently is dominated by the liquid crystal display (LCD) technology that has overthrown the CRT displays. The CRT displays have been deserted by a number of reasons, where the main two is large space occupation and high power dissipation of the thermionic emission tube. LCD panels, however, is based on a liquid crystal that modulate the light coming from the background illumination source and can be made into a flat panel that occupies far less space than CRT displays. Other than being thinner, LCD panels also require less power consumption and promises a longer life time. Although many advances have been carried out to improve their performances, LCD panels still have shortcomings in areas such as brightness, image quality, viewing angle and providing adequate operation speed for fast-motion videos. It is thought that successful integration of field emitter arrays into display technology will not only reinstate the favourable properties of CRT displays such as wide viewing angle, high brightness, good image quality and fast operation speed at a degree LCD displays fail to provide, but also have a low power consumption and a high working temperature range without the bulky appearance. Furthermore, unlike LCD panels, field emission display (FED) panel technology does not need using additional diffuser and polarizer films or filters, thus the thickness of the panel will be only determined by the anode-cathode distance and thicknesses. Thus, by proper engineering, designing even thinner panels than currently acquired will be possible.

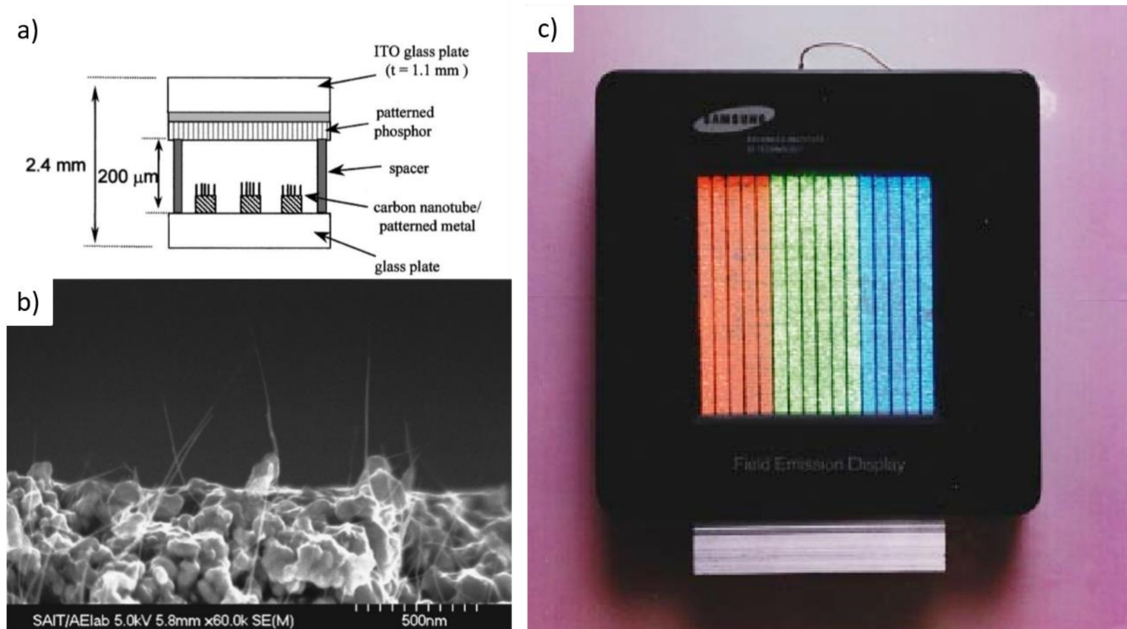

Figure 2. (a) The schematics of CNT FED panel by Samsung (b) The SEM image of the CNT emitters used for FED (c) The FED prototype made by Samsung (Source: Choi, Chung, Kang, et al. 1999).

A lot of research have been focused on fabricating field emitter arrays that could meet the needs for a field emission display (H. Chang et al. 2013; Uemura et al. 2003; de Heer, Châtelain, and Ugarte 1995). As early as 1999, Samsung demonstrated a 4.5 inch prototype of FED panel based on carbon nanotube (CNT) field emitters shown in Figure 2 (Choi, Chung, Park, et al. 1999). Yet, the need for more robust field emitters capable high and stable current densities are still to be met to conventionally integrate this technology into our lives.

Another prospective application of field emitters is integrating them into spacecraft neutralizers. Such neutralizer systems are required for prevention of spacecraft charging from satellite ion propulsion. Energy efficiency, capability to produce high current densities, light weight and low power consumption of field emission electron sources make them excellent candidates for charge neutralizer systems. Silicon tip field emitter arrays (Aplin, Collingwood, and Kent 2004) and CNT based field emitter arrays (Aplin et al. 2009) are both studied to be used as spacecraft neutralisers. Long lifetime and repeatable emission characteristics of the carefully designed emitters with no manufacturing defects demonstrate promising results to be deployed in space propulsion technology.

Field emitters are also a promising candidate for microwave power amplifiers. Conventionally, thermionic emitters and solid state transistors are used for power amplifiers. Vacuum tubes containing thermionic cathodes are easier to integrate to high power applications, where the solid state transistors need complex equipment to be used. But thermionic cathodes have high power consumption and short lifetime associated with elevated working temperatures. Solid state microwave power amplifiers have longer life-time, but they are hard to integrate into high frequency applications. Field emitter arrays are a promising candidate to replace both types of amplifiers for high frequency applications up to 1 THz (Ganguly, Phillips, and Gray 1990) with their low power consumption and long lifetimes (W. Zhu 2001).

The dependence of electric field on the separation distance between anode and the emitter cathode also promises a novel application of field emitters as pressure sensors. By utilizing a flexible anode that could be bent as a response to applied pressure, the change in the emission current with respect to deformation of the collector anode can be used to determine the pressure applied on the sample. Both Si emitter arrays (Schreiner et al. 2011; Lee and Huang 1992) and CNT based field emitters (Abdi, Malekan, and Darbari 2013) have shown favourable results by means of pressure sensing. When high temperature endurance and radiation stability of the electron field emission sources are taken into account, these novel sensors seem to be a promising candidates to acquire high accuracy and high frequency measurements even in harsh environments.

1.1.2. Designing Field Emitter Structures

Different materials, both metals and semiconductors, in various forms such as nanowires (R. Wu et al. 2012; W. M. Zhou et al. 2006; Shen et al. 2006), nanotubes (Bonard et al. 2001; H. Chang et al. 2013; Yahachi Saito and Uemura 2000), micro- and nanopillars (Y. M. Chang et al. 2012; W. Li et al. 2008; Kang et al. 2012), have been investigated for their field emission properties and potential applications to technology. There are three fundamental criteria that should be met in order to determine whether the field emitter arrays could be integrated to practical applications.

a. Low threshold and turn-on fields

The prospective field emitters are desired to start emitting electrons at low applied electric fields for practical applications. Although there may be found different notations in the literature, the well accepted definition of threshold field for field emitter arrays is the electric field where the emitter arrays start emitting 10 μA/cm^2 electric current. The definition of turn-on field is even more debatable, and is mentioned for current densities as low as 1 nA/cm^2. Throughout this thesis, turn-on field defines the electric field where the emitter array supplies a current of 1 μA/cm^2.

The turn-on and threshold fields of field emitters are directly correlated with the emitter material, as well as the aspect ratio and the shape of the emitter structures. Within the scope of this thesis, the effect of aspect ratios and different geometries of nanopillars on turn-on and threshold field of the silicon carbide field emitter arrays are investigated.

b. Emission efficiency

Emission efficiency is defined as the magnitude of the current density acquired from the emitters under different applied electrical fields. It is related to many aspects such as the emitter material's work function, the aspect ratio and the geometry of the emitters. As mentioned above, the emission efficiencies of silicon carbide nanopillars with different aspect ratio and geometry are investigated in further chapters.

c. Emission current stability

The ability of field emitter arrays to produce stable currents for long periods of time is a crucial property for technological applications. There are a number of reasons of current instabilities in the field emitter arrays. The most common mechanism of emission current failure on carbon based field emitters, such as graphene acquired by chemical vapour deposition or CNTs is relocating or tearing of these structures from the surface under high applied fields (Babenko, Dideykin, and Eidelman 2009). For field emitters made up of other materials, emission failure occurs due to joule heating at high emission current densities. These two mechanisms result in abrupt changes and discontinuities in the field emission currents.

Field emission currents also tend to fluctuate temporally and spatially. These fluctuations arise from small changes in the work function on the emitter array. Spatial fluctuations can be minimized by well controlled shape and spacing of the emitter array structures. There are also studies on how to reduce the temporal fluctuations in the field emitter currents (Gray 1994). But these mechanisms are not within the scope of this thesis thus will not be discussed further.

There are also other factors that needs to be taken into account when engineering prospective commercial field emitter arrays, such as long life time of the emitters, ease and controllability of fabrication and the coherence of the emitted electrons.

1.2. Silicon Carbide

Silicon Carbide (SiC) is a IV-IV binary compound, wide gap semiconductor composed of silicon and carbon atoms. Its excellent properties including outstanding mechanical strength, resistance to thermal shock and radioactivity, and excellent thermal conductivity makes SiC a widely pronounced candidate for semiconductor based devices that are meant to work in extreme environments, where conventional semiconductors such as silicon or gallium arsenide cannot endure. There have been a significant number of research (Kusdemir et al. 2015; Sheppard et al. 1996; Slater et al. 1996) over the decades to implement this extraordinary material into electronic components, and a vast number of electronic devices based on SiC have been proposed with gradually increasing performances. Yet the number of commercialized SiC based products have remained low due to the expense of the substrate.

SiC rarely occurs in the nature and firstly discovered in the 19th century during the attempts of synthesizing diamond. Thus the high price of the substrate arises from the difficulties of the growth procedure of single crystalline wafers and the rare abundance of the material itself. Optimistically, many methods have been proposed to synthesize substrates with increasing crystalline quality and diameter; hence it would not be wrong to predict an increase in the quantity of SiC based commercialized devices in the near future.

Recently disseminating high quality SiC wafers have led to more research on the practical applications of the substrate and to the development of advanced techniques on device fabrication procedures (Evans and Beheim 2006; The et al. 2014). In the vicinity of such control over the robust SiC has paved the way to use this substrate in many applications of semiconductor industry including metal-oxide-semiconductor field effect transistors (MOSFETs) (Narasimhamorti 1976) and electron field emitters (W. Li et al. 2008).

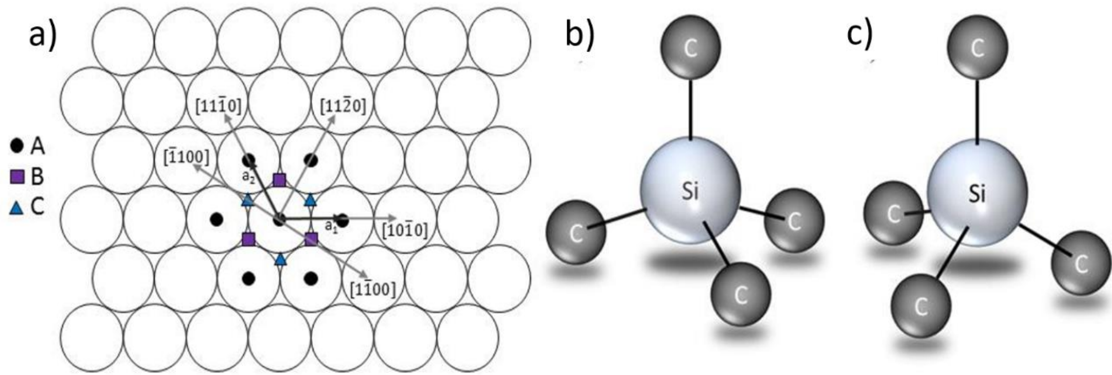

Figure 3. (a) The hexagonal basal plane of SiC crystal (b) The model of a SiC molecule (c) SiC molecule 180° rotated with respect to its initial state.

Other than bulk SiC wafers, chemically synthesized SiC nanowires have also attracted attention over decades to be applied as electron field emitters (Shen et al. 2006; R. Wu et al. 2012; W. M. Zhou et al. 2006), which will be discussed in detail later in this thesis.

1.2.1. Crystal Structure and Polytypes of Silicon Carbide

Si and C atoms in SiC are strongly bonded by sp^3 hybridization of C atoms with a Si-C bond length of 1.89 Å (Shur, Rumyantsev, and Levinshte 2005). The tetrahedron formed by one silicon atom at the center bonded to 4 carbon atoms consists of 88% covalent and 12% ionic bonds and the distance between Si-Si or C-C atoms are found to be 3.08 Å (Figure 3.*b*).

Different stacking orders and crystal lattices of these tetrahedron structures gives rise to over 250 different types of SiC. Figure 3.*a* represents the basal hexagonal plane and denoted as A, the centres of the sequent molecules are either placed in the crystal direction defined as B or C. It is also possible that the sequent SiC molecules are turned by 180° with respect to their initial states (Figure 3.*c*). Those molecules are called twinned and the stacks of those twinned molecules are then presented as A', B' and C'. In order to distinguish these structures Ramsdell (Ramsdell 1946) proposed a naming system, including the number of their stacking layers and crystal type; C (cubic), H (hexagonal)

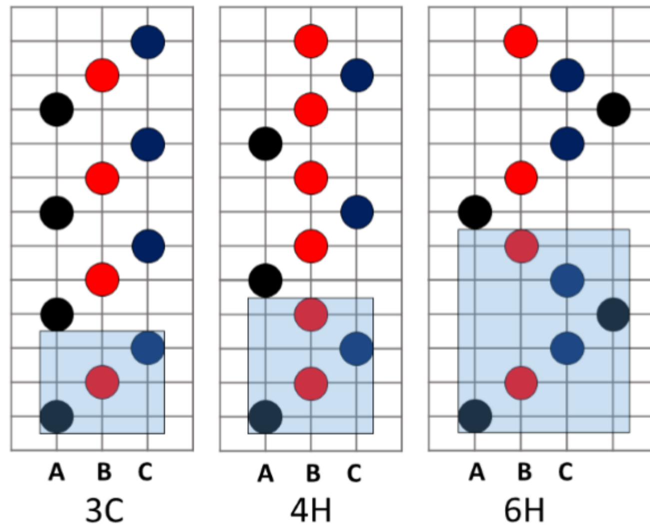

Figure 4. Representations of stacking orders for topmost popular polytypes of SiC (Source: E. Kusdemir 2015).

and R (rhombohedral). Each polytype has slightly different electrical and physical properties. The stacking order schematics are shown in Figure 4 for topmost studied SiC crystals, namely cubic 3C-SiC, and hexagonal 4H- and 6H-SiC.

Table 1. Crystal structure parameters of 3C-, 4H- and 6H-SiC.

Polytype	**3C**	**4H**	**6H**
Structure	Zinc-blende	Wurtzite	Wurtzite
Hexagonality	0%	50%	33.3%
Atoms per unit cell	2	8	12
a (Å)	3.08	3.08	3.08
c (Å)	7.55	10.05	15.12
d (g/cm^3)	3.21	3.24	3.22

3C-SiC has a stacking sequence given as ABCABC as shown in Figure 4. Unlike other polytypes, only cubic form of SiC, 3C-SiC crystal structure possesses an isotropic morphology. This isotropy results in stationary electrical properties that is independent of the crystal orientation. That is one of the reasons that make 3C-SiC polytype desirable. Another reason is the ease of acquiring this crystal structure as it can be grown on Si substrates. Although this property makes it easier to grow larger sized and lower priced

substrates, the quality of such grown wafers are low due to high thermal coefficient and lattice mismatch between these two materials.

Table 2. Comparison of SiC and other semiconductors (Source: Harris 1995).

Semiconductor	Si	3C-SiC	4H-SiC	6H-SiC	Diamond
Bandgap (eV)	1.12	2.4	3.2	3.0	5.5
Bandgap Type (D: direct, I indirect)	I	I	I	I	I
Thermal Conductance ($Wcm^{-1}K^{-1}$)	1.5	3.5-5.0	3.5-5.0	3.5-5.0	20.0
Critical field (E_c) ($MVcm^{-1}$)	0.25	2.0	2.2	2.5	5.0

4H- and 6H- SiC both has hexagonal structures but their stacking sequences, and thus the degree of hexagonalities are different from each other. 4H-SiC consists of 50% hexagonal and 50% of cubic bonds, where 6H-SiC has 33.3% hexagonality. The stacking of these structures are ABCB and ABCACB for 4H and 6H-SiC respectively. Given to the distinctions between different directions in hexagonal lattice, the electrical properties of these substrates differ for each direction of the plane. The crystal structure parameters of these three polytypes are given in Table 1.

1.2.2. Properties of Silicon Carbide

One of the properties that makes SiC a hotspot for research is its wide bandgap ranging from 2.3 to 3.3 eV depending on the polytype. Such large bandgap limits the thermal generation of electron-hole pairs, thus allows SiC based devices to work under higher temperatures, where other semiconductor materials fail. In addition, the same property causes SiC to have very high breakdown field in the range of 3-5 MV/cm^{-1}, which is an order of magnitude higher than silicon. High breakdown field causes SiC based devices to have much higher power efficiencies; that paves the way for creating smaller, high power devices with relatively low resistivity.

The thermal conductivity of SiC, given to be in the range of 350-490 $Wm^{-1}K^{-1}$, is quite high, even superior to that of copper and much higher than other conventional semiconductors like silicon. Thus, SiC based devices are able to dissipate the heat more efficiently, and are suitable to work in extreme environments. The thermal shock resistance of SiC, coupled with high thermal conductivity, makes the material the best candidate for high power applications.

SiC also possesses a high chemical inertness. Although this property makes SiC based devices hard to fabricate either with wet-etching or dry etching processes, it also makes the material desirable for microelectromechanical systems (MEMS) that are meant to work in aggressive and corrosive medium.

A summary and comparison of different polytypes of SiC, Si and diamond are given in Table 2.

1.3. Outline

This thesis covers the fabrication of nanopillars on bulk SiC substrate by using nanosphere lithography and the field emission characterizations of these fabricated structures. The remainder of this thesis is structured as given below.

In Chapter 2, fundamental phenomena about electron field emission from metals and semiconductors are discussed. Field emission characteristics of SiC nanostructures are covered.

In Chapter 3, nanofabrication techniques are briefly presented. The nanosphere lithography technique was discussed. The fabrication steps of the etch mask in this work are covered in detail.

In Chapter 4, the field emission characterizations of fabricated nanopillars are investigated.

In Chapter 5, summary of the thesis work.

CHAPTER 2

FIELD EMISSION PHENOMENON

2.1. Fowler-Nordheim Tunnelling

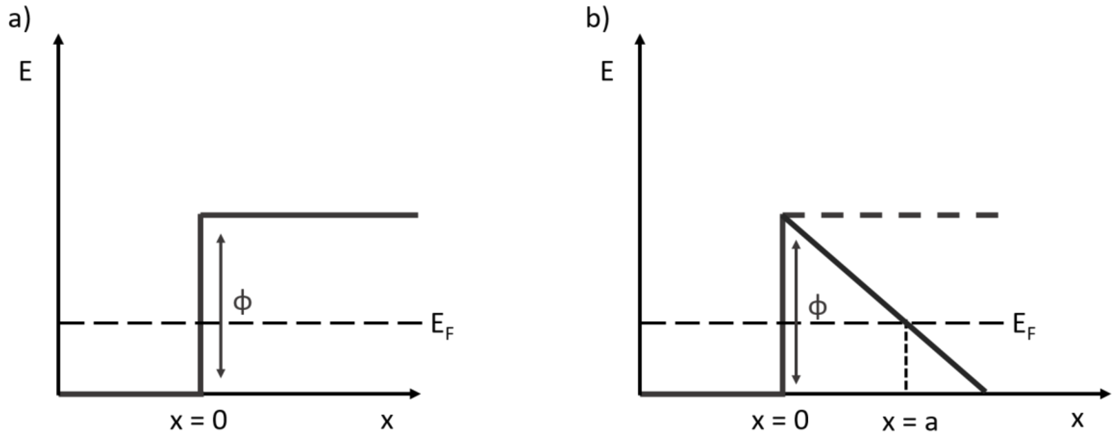

Figure 5. The schematic illustration of the potential barrier of a metal (a) without external electric field (b) under high external electric fields.

We can think of electrons in a metal under vacuum is just like the illustration at Figure 5.*a*. The step height, in this case, is equal to the metal's work function. For simplicity, we can assume the potential energy inside the metal is equal to zero; which corresponds to the free electron model, thus no force is acting on the electrons. For T = 0 K, the electrons fill all the energy levels from $E_p = 0$ to $E_p = E_F$ where E_F is the Fermi energy level and is smaller than the work function of the metal. In this case, the solution of Schrödinger equation for both $x > 0$ and $x < 0$ reveals that transmission of the electrons becomes zero, and all the electrons are reflected back from the step potential after a certain depth.

Under strong electrical fields ($F > 10^7$ V/cm) perpendicular to the metal's surface, the barrier becomes distorted and takes the shape of a triangle (Figure 5.*b*). Thus, the probability of finding electrons outside the metal, in other words, in the vacuum, becomes a finite number. It is important to note that for metals, the electric field cannot penetrate inside the metal, thus the distortion happens only at the outside. As the applied field

increases, the barrier gets narrower, thus the tunnelling probability of electrons becomes a larger number. This phenomenon of tunnelling of electrons through such a triangular potential barrier formed in the surface of metals was investigated by R. H. Fowler and L. Nordheim in 1928.

The Fowler-Nordheim (FN) method calculates the transmission coefficient from a triangular barrier shown in Figure 5.*b* as in the following manner:

$$T(E) = \exp\left(-\frac{4}{3eF\hbar}\sqrt{2m}\phi^{\frac{3}{2}}\right) \tag{2.1}$$

And the field emission current density from the transmitted electrons is given as:

$$J_{FN} = \frac{AF^2}{\phi}\exp\left(-B\frac{\phi^{\frac{3}{2}}}{F}\right) \tag{2.2}$$

where the parameters A and B are known as FN constants (Mihalcea and Piot 2008) given as 1.54×10^{-6} AeV/V^2 and 6.83×10^7 V/(eV$^{3/2}$cm), respectively.

The analytical expression of FN tunnelling equation relies on some assumptions to explain the electron field emission phenomenon, those assumptions are (Forbes 2004):

a. The field emission happens at the emitter tip, because this is where the distortion of potential barrier is higher, thus the substrate effects are unimportant.
b. Due to the abovementioned fact, the field emission is a one-dimensional problem, since the emission happens at the tip of a very sharp emitter.
c. The emitter material is compatible with the Sommerfeld free electron model.
d. The field emission current is derived from a single, metallic emitter.
e. The geometry of the field emitter plays no role in the field emission. The emitter surfaces are free of defects and impurities. Thus the emitter has the same characteristics as the bulk material.
f. The vacuum potential barrier is a triangular barrier, with no distortions. In other words, image potential effects are not taken into account.

g. The work function of the emitter material does not change with respect to applied electric field.
h. The electron emission is in equilibrium state; thus electrons obey the Fermi-Dirac distribution function f(E).
i. The field emission happens at T = 0 K.

Those assumptions are feasible for metallic, single emitters; thus FN theory can explain the field emission behaviour in such cases. Even the zero temperature approximation provides excellent results for field emission from metallic emitters at room temperature.

2.1.1. Field Enhancement

As mentioned above, the field emission currents are observed under large applied fields in the range of 10^7 V/cm. If we consider an emitter system with flat electrodes similar to Figure 1, the electric field is given by $E_0 = V/d$, where V is the voltage applied between the anode and the cathode (emitter), and d is the distance between them. By using sharp field emitters, it is possible to reduce the required electric field to observe electron field emission currents, owing to field enhancement properties at the tips of sharp structures.

The local electric field at the tips of each emitter is estimated by Vibrans (Vibrans 1964) to be:

$$E = \left(\frac{h}{r} + 2\right) E_0 \tag{2.3}$$

where h is the height of the emitter structure, r is the radius of the emitter tip and E_0 is the field applied between the anode and the cathode. The factor $\left(\frac{h}{r} + 2\right)$ is known as field enhancement factor and it has no units.

In order to include these effects in the field emission currents, field enhancement factor (β) is introduced in FN formula, such as:

$$J_{FN} = \frac{A\beta^2 E^2}{\phi} \exp\left(-B\,\frac{\phi^{\frac{3}{2}}}{\beta E}\right) \tag{2.4}$$

2.2. Field Emission from Semiconductors

The ease of fabrication of semiconductor structures, especially in the vicinity of recent advances in nanofabrication techniques, have attracted a lot of attention by means of using these materials as field emitters (Shen et al. 2006; W. Li et al. 2008; Y. M. Chang et al. 2012). There have been a growing number of researches by means of field emission characteristics of various semiconducting materials. Yet the field emission from semiconductors were firstly theoretically investigated by Stratton (Stratton 1955; Stratton 1962) in 1955, and then experimentally studied by Allen (Allen 1957) and D'Asaro (D'Asaro 1958).

Fowler-Nordheim approach for electron field emission have crucial shortcomings to explain the electron emission from semiconductor structures, due to some main assumptions it covers. The effect of field penetration and presence of surface states affects field emission phenomenon in semiconductor structures. In addition, the effect of temperature becomes more pronounced due to thermally generated electron-hole pairs. The doping of semiconductors also plays an important role in the field emission characteristics.

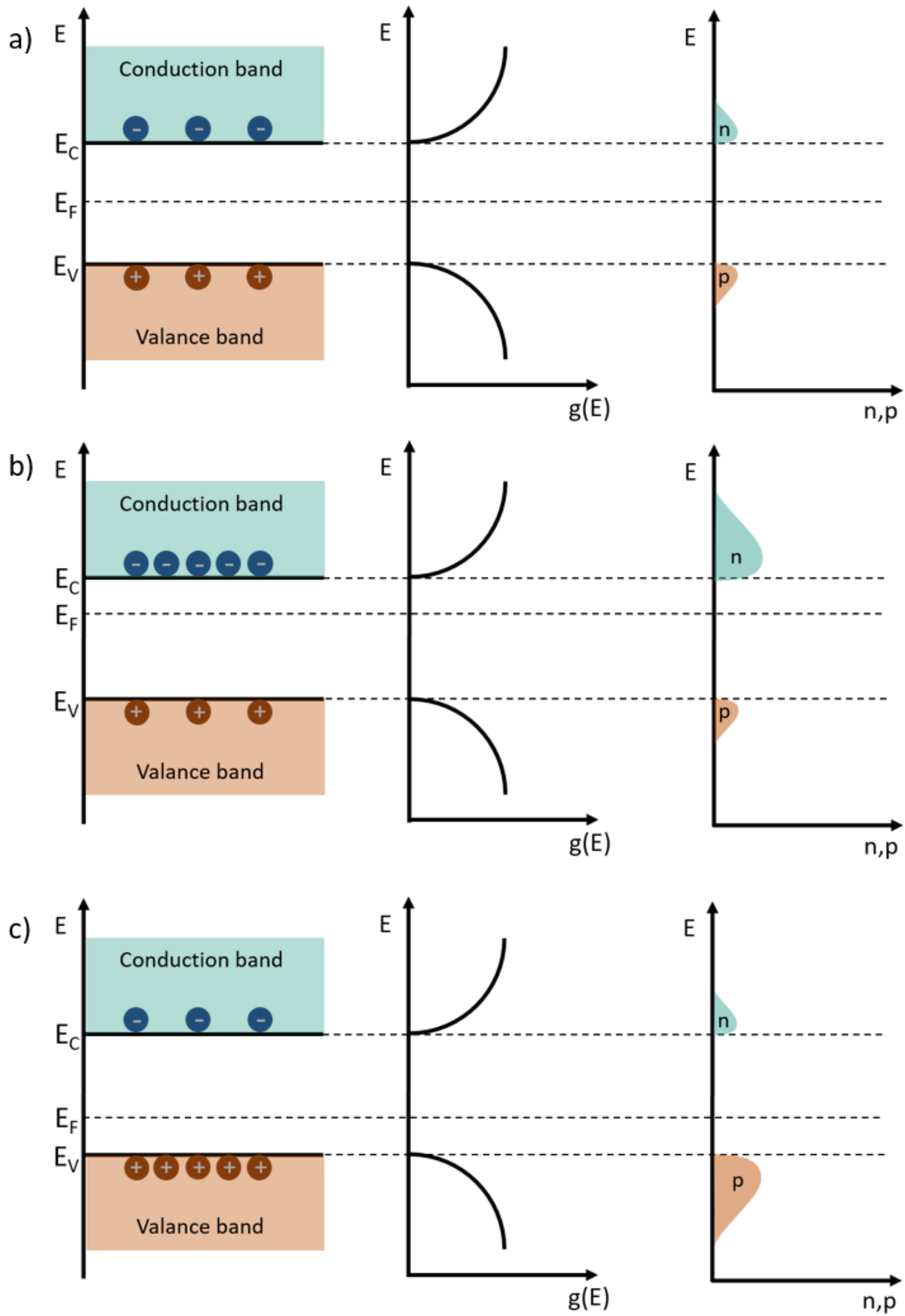

Figure 6. The schematics, simplified band diagrams and charge carrier concentrations for (a) intrinsic (b) n-type (c) p-type semiconductors in equilibrium conditions (Source: Sze 1981).

Figure 6 shows the schematics, simplified band diagrams and charge carrier concentrations of intrinsic, n-type and p-type semiconductors in equilibrium conditions where the temperature is higher than absolute zero. It can be seen from the Figure 6 that the Fermi level of the semiconductors shifts according to the doping concentration to preserve the charge neutrality. For each type of semiconductor, there are charges in the conduction band that can tunnel to the vacuum under high electric fields when the temperature is larger than 0 K. Theoretically, if the potential barrier can be narrowed enough, field emission also occurs from the top of the valance band, where there are no free electrons. The tunnelling of the bound electrons, in such case, leaves a hole behind, which is then balanced by another electron supplied from the bulk (Gomer 1994).

Figure 7 illustrates the basic mechanism of field emission from an n-type semiconductor. The field emission firstly occurs from the valance band, where the barrier width reaches a certain point, denoted as a. The electrons tunnelling from the conduction band comes across to a barrier height of χ, the electron affinity of the semiconductor, defined from the bottom of the conduction band to the vacuum level. At higher applied electric fields, the barrier narrows enough to allow field emission from the valance band. In this case, the tunnelling electrons comes across to a barrier height of $\chi+E_g$. For n-doped semiconductors, the contribution to field emission current is supplied mainly from the electrons in the conduction band, thus, for practical purposes, the work function (ϕ_s) of the semiconductor, which is defined as the potential difference between the Fermi and the vacuum levels ($E_C - E_F + \chi$).

Unlike metals, the external electric field can penetrate into semiconductors and causes a certain bending in the conduction band (CB) and the valance band (VB). Thus, the abovementioned model does not represent a realistic situation for the observed field emission phenomenon.

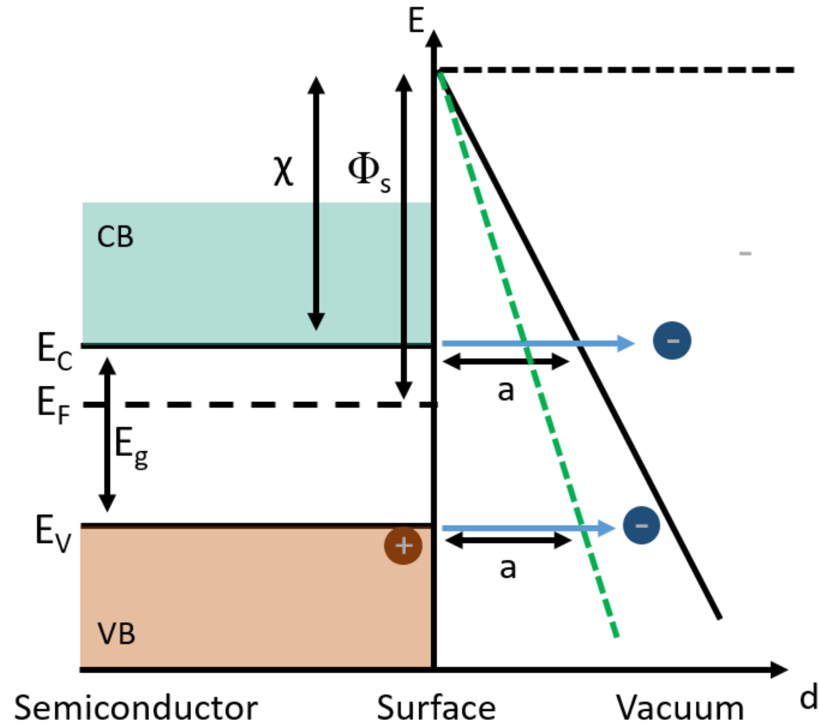

Figure 7. Schematics of a simplified model for electron field emission from semiconductors.

The band bending effect for two cases in an n-type semiconductor can be seen in Figure 8. At lower external electric fields, the bending is not sufficient enough to bring the bottom of the conduction band below E_F. In this case, electron concentration in the bottom of the conduction band increases (Gomer 1994), thus more electrons can tunnel through the barrier, but the work function stays intact. This situation is observed at low electric fields, intrinsic and/or lightly n-doped semiconductors, where E_F lays away from the conduction band edge. At higher electric fields, the penetrated electric field causes the bottom of the conduction band to bend below E_F. In this case, the work function of the material reduces, and more electrons are collected at the accumulation region. For this case, the work function in the FN equation should be changed with a calculated effective work function.

As can be seen from the Figure 8.*a* and *b*, the band bending phenomenon in semiconductors only affects the electrons at the conduction band. The band bending also occurs in the valance band, but the effective work function does not change. Thus the field emission from valance band stays unaffected.

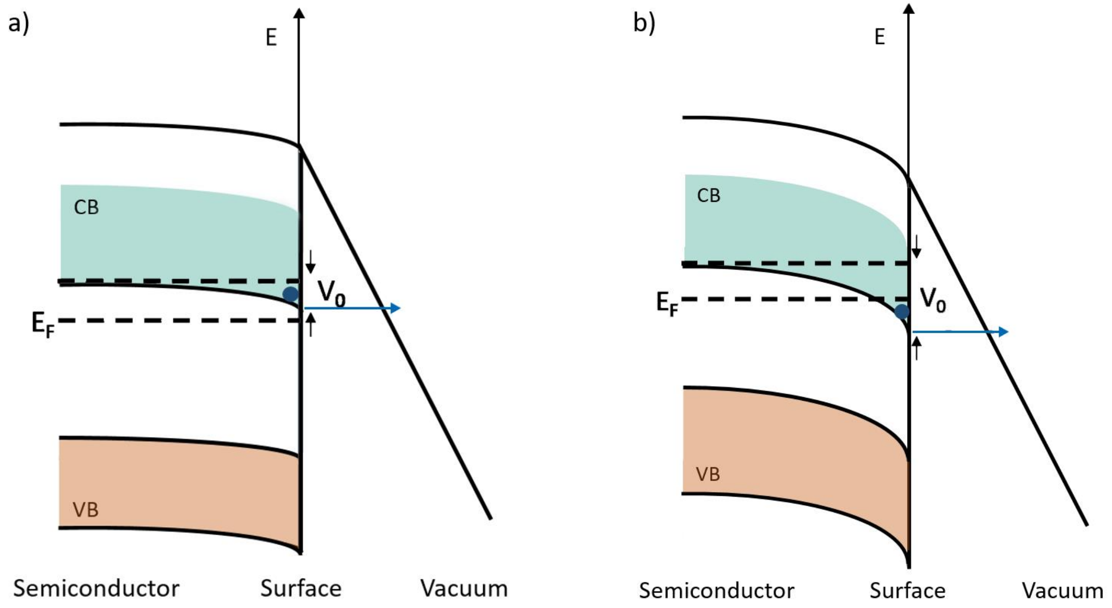

Figure 8. The band bending effect in an n-type semiconductor (a) for low electric fields (b) for high electric fields.

2.2.1. Image Charge Effect in Semiconductors

Image charge theorem in electrostatics proposes that a particle with a charge q at a distance d from an infinite conductive plate experiences a force on itself, such as there is an equal but negatively charged (-q) particle at a distance d behind the plate (Solymar and Walsh 2009). This phenomenon is also observed for electron field emission. The image charge effects cause a lowering in the potential barrier, which is known as Schottky lowering effect (Nordheim 1928).

The barrier height adjustment factor due to image charge effects for semiconductors is proportional to $\sqrt{\frac{\varepsilon_s-1}{\varepsilon_s+1}}$ where ε_s is the dielectric constant of the semiconductor (Stratton 1955). For example, if the semiconductor used is 6H-SiC, where $\varepsilon_s = 9.66$, the adjustment factor becomes:

$$\sqrt{\frac{\varepsilon_s - 1}{\varepsilon_s + 1}} = 0.90 \qquad (2.5)$$

Since the value given in Equation 2.5 is close to 1, it would be feasible to say that the image potential effects for field emission from 6H-SiC samples can be neglected for the practical applications.

2.3. Field Emission from Silicon Carbide Nanostructures

Electron field emission properties of silicon carbide structures are widely studied thanks to the advances in growth and etching techniques in recent years. Most of the research has been centred around chemically synthesized nanowires (NWs) of SiC, due to high aspect ratios of these 1-dimensional (1D) structures.

The topmost pronounced 1D field emitter candidate has been carbon nanotubes (CNTs), due to high aspect ratio of these nanostructures (Xianqi et al. 2014; S. Y. Chen et al. 2003; Bonard et al. 2001; de Heer, Châtelain, and Ugarte 1995; Xu et al. 2013). Such high aspect ratios provide low turn-on and threshold fields due to the field enhancement at the tip apex. It has been also shown that CNT based emitters (H. Zhang et al. 2007) can produce high current densities up to 2 mA/cm^2. But in terms of stability of the field emission currents (Kim et al. 2017) and life-time (Williams et al. 2010) of the emitter arrays, CNT based emitters have failed to provide desirable results. However, given to their extraordinary properties and good field emission characteristics, SiC nanowire based emitters propose a more feasible alternative. Outstanding mechanical endurance and chemical inertness of the SiC NWs provide a longer life-time and more stable field emission even under extreme environments (X. Zhang et al. 2010). In addition, superior thermal stability of SiC makes these emitters more stable under Joule heating effect, where the CNT based emitters show a gradual shortening (Y Saito 2010).

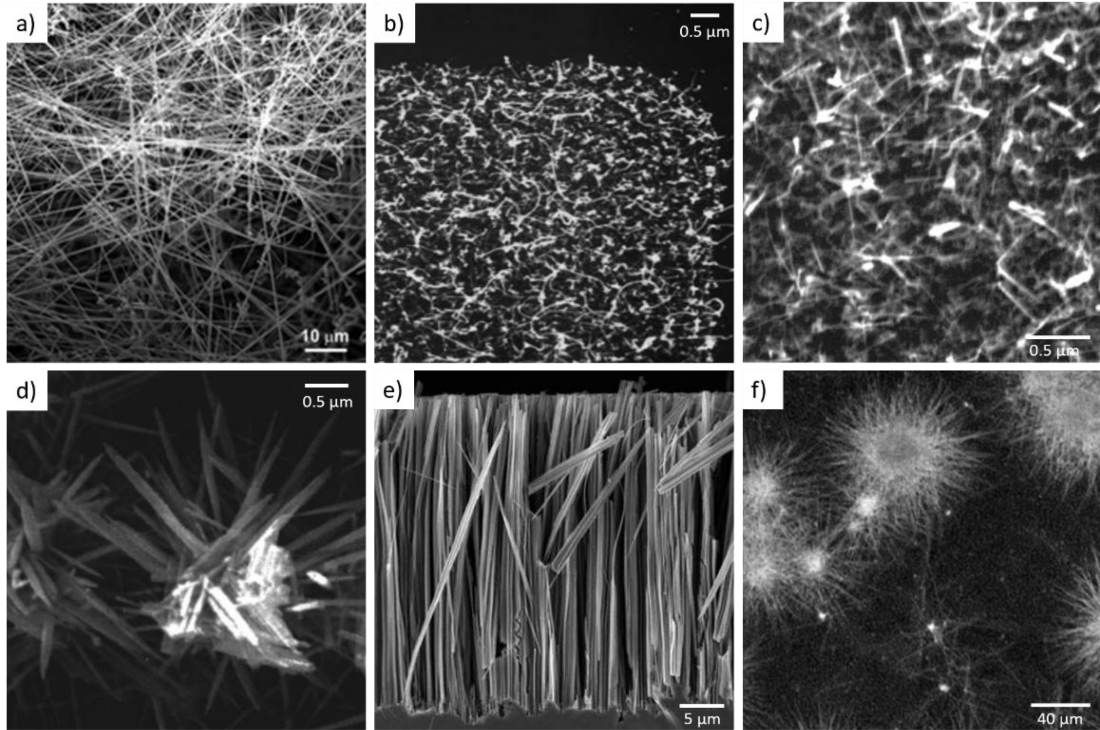

Figure 9. SiC NW based field emitters acquired by bottom-up methods (a) β-SiC nanowires (Source: Shen et al. 2006), (b) α-SiC nanorods (Source: T. H. Yang et al. 2003) (c) β-SiC nanorods (Source: X. T. Zhou et al. 2000), (d) Needle-shaped SiC (Source: Z. S. Wu et al. 2002) (e) Aligned SiC porous NWs (Source:Y. Yang et al. 2008) (f) Quasi-aligned β-SiC NWs (Source: X. Zhang et al. 2010).

Table 3. The field emission properties of different SiC based NWs (Source: X. Zhang et al. 2010).

	Emitter Type	Turn-on Field (V/μm)	Reference
a	β-SiC nanowires	10.1	Shen et. al. 2006
b	α-SiC nanorods	27	Yang et. al. 2003
c	β-SiC nanorods	13-17	Zhou et. al. 2000
d	Needle shaped SiC	5	Wu et. al. 2002
e	Aligned SiC porous NWs	2.3-2.9	Yang et. al. 2008
f	Quasi-aligned β-SiC NWs	0.55-1.4	Zhang et. al. 2010

Figure 9 shows 6 different types of SiC nanowires, whose field emission characteristics are presented in Table 3. As can be seen from the results provided, the vertical alignment of SiC nanostructures drastically improve the turn-on fields for field emission currents.

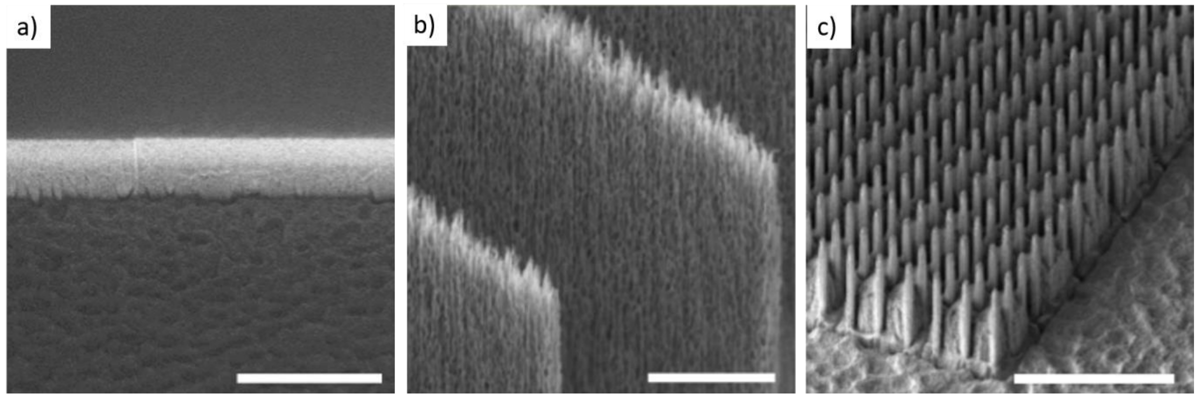

Figure 10. SEM images of different SiC emitter structures reported by Kang et. al. (a) mesa structure (scale bar 50 µm) (b) fin array (scale bar 4 µm) (c) pillar arrays (scale bar 10 µm) (Source: Kang et.al. 2012).

Table 4. The electron field emission characteristics of etched SiC microstructures presented in Figure 10.

Subletter	Emitter Type	Turn-on Field (V/µm)	Field Enhancement (β)
A	SiC mesa	9.6	1640
B	SiC fin	6.5	(not provided)
C	SiC pillar	4.4	3636

Although the results are satisfying, it is hard to maintain a large area, vertically well-aligned nanostructure arrays by using nanowires grown by bottom-up methods. In addition, acquiring a homogenous surface distribution of these structures remains a challenge. These issues can be resolved basically by etching these nanostructures directly from the bulk SiC wafer, by dry etching technique via well-defined hard etch masks.

Kang et. al. (Kang et al. 2012) has shown that field emission from n-doped 6H-SiC wafers etched in different microstructures provide outstanding field emission current densities and field enhancement, that are given in Figure 10 and Table 4.

It is clearly seen that the pillar structure provides the most feasible results by means of field emission due to its high aspect ratios. In this work, the pillar structures etched by focused ion beam technique has a width of 1.5 µm and a height of 20 µm. In this case, the field enhancement factor (β) should have been ~15, according to Equation 2.3. But the experimentally acquired value is 303 times larger than the calculated one. This abrupt change is attributed to good aspect ratios, well organized large emitter array structure and the n-doping of the sample.

Unfortunately, due to difficulties of dry etching such a hard substrate as SiC, field emission characteristics of dry-etched structures are not widely studied. Especially, the field emission from etched nanostructures of SiC have not been proposed, yet. In this thesis work, the field emission behaviours of SiC nanopillar structures etched from bulk n-type 6H-SiC are investigated for two sets of emitters with different aspect ratios and tip geometries.

CHAPTER 3

FABRICATION OF SiC NANOPILLARS

3.1. Nanosphere Lithography Fabrication Technique

Since the famous lecture of Richard Feynman "There is plenty of room at the bottom" in 1959, there have been a vast number of breakthroughs in nanoscale researches. The nanometre scale of these structures are found to possess unique properties unlike their bulk counterparts and the novel properties of nanostructures have attracted a great deal of attention from scientists from every discipline such as materials science, physics and chemistry. Such tremendous attention resulted in the development of new and unique techniques to fabricate nanoscale structures. The more prevalent the nanostructures have gotten, the more information could be gathered about their nature, and as an inevitable result these distinctive structures have yet started finding their grounds in contemporary technological applications.

The main challenge of nanofabrication is to develop new techniques that proposes high controllability, low cost and flexibility by means of processing. There have been developed countless techniques to fabricate nanoscale structures, yet they can be grouped under two main headlines according to the way they approach to the problem: bottom-up fabrication and top-down fabrication techniques.

Bottom-up approach resides on the way nature works to grow nanometre-size structures. In other words, each building block is introduced one by one to form the desired structure, in ways to satisfy a self-assembly process. Such method is well-covetable as in the vicinity of new trends of smaller devices; as it makes possible to acquire finer structures than many lithography techniques. It also proposes a favourable and relatively more cost-effective way to grow a wide range of nanomaterials, including complex heterostructures.

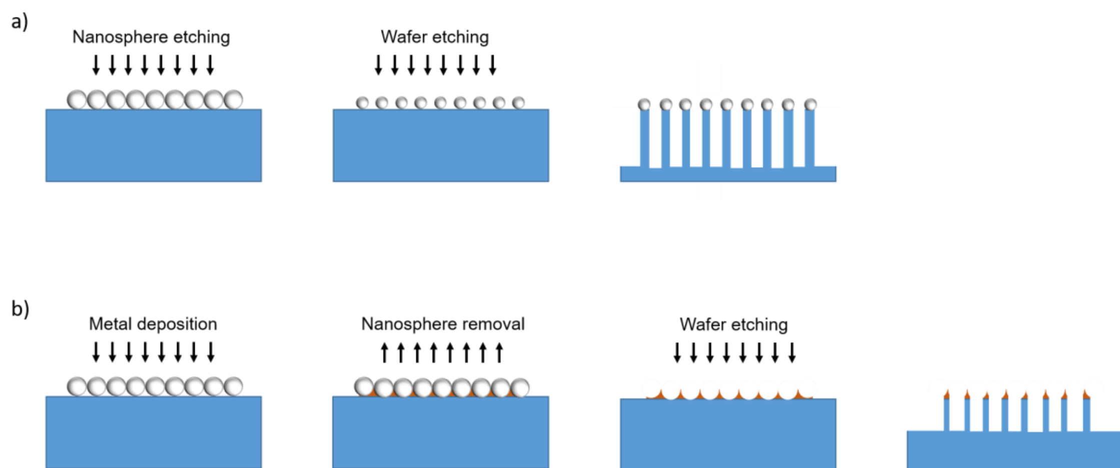

Figure 11. A typical schematic illustration of NSL lithography where (a) Nanospheres used as an etch mask (b) Nanospheres used as a template.

Bottom-up methods (Bechelany et al. 2007; Attolini et al. 2010; Seong et al. 2004; Hao et al. 2006) promises the ability to cheaply and directly grow nanowires of a vast range of materials, which can be used as field emitters. However, there are two obstacles that should be overcome to fabricate reliable structures by using this technique: the grown structures possess structural defects such as twinning (Huczko et al. 2005), furthermore it is very difficult to control the doping concentrations (Seong et al. 2004) of the grown structures. An additional challenge is to grow well aligned structures on the surface, which is a crucial parameter for field emitters.

The second nanofabrication technique, namely top-down fabrication, resides on etching structures on bulk substrates until the desired size is reached. In this approach, various lithography techniques in combination with etching procedures are applied to fabricate nanostructures on the wafer surface. Those processes are more difficult, time consuming and require expensive equipment when compared to bottom-up techniques; but they allow fabrication of highly ordered structures with precisely controlled orientations. Etching procedures require suitable etch masks that defines the shape of the resulting structure. For dry etching procedures, nanoscale etch masks are conventionally created by photolithography and electron beam lithography (EBL). Both techniques are time consuming and require expensive equipment.

Nanosphere lithography (NSL) (Hulteen 1995; Colson, Henrist, and Cloots 2013; Kosiorek et al. 2004; Haynes et al. 2002), also known as colloidal lithography or natural lithography is a powerful, alternative technique that promises large-area production of

nanostructures in a fast and cost-effective manner. 2D-arrays of these nanospheres have started being used as a masking or surface patterning of different substrates for etching (L. Liu et al. 2011; W. Li et al. 2008) or as a template to deposit different materials (Hsieh et al. 2007). The simplicity of acquiring this two dimensional (2D) pattern on the surface, low cost, the lack of need for expensive equipment and the flexibility to apply in a wide variety of substrates have attracted immense attention on this technique in the last decades. The ease of fabricating large area array of structures below 100 nm has placed this technique one step ahead of conventional lithographical approaches.

NSL resides on the naturally occurring self-assembly pattern known as colloidal crystal pattern to etch highly organized, large area structures on wafer surfaces. Depending on which wafer and what kind of material the nanospheres are made of, the colloidal crystal structure can be used directly as an etch mask (Figure 11.*a*), or can be used as a template to acquire the desired etch mask pattern on the surface (Figure 11.*b*).

The term nanosphere is used to define spherical particles with diameters ranging between tens of nanometres up to a few microns. Those particles made up of various materials including various polymers such as polystyrene (PS), poly-methyl methacrylate (PMMA), polylactide (PLA), inorganic substances like silica, alumina, gold, silver and platinum, are commercially available at different sizes and qualities to be used for a great number of purposes. Among them, PS nanospheres are widely used for a vast range of applications owing to the ease of modifying their shape and surface. The ease of surface modification allows functional groups to be attached on the PS sphere surface, thus makes them possible to be used in biological applications. Additionally, the ease of shape modification is a desirable property for nanolithography applications. The diameters of PS nanospheres can be easily reduced by applying O_2 plasma for defined periods of time (Cheung et al. 2006; Y. J. Zhang, Li, and Chen 2008) (Figure 12).

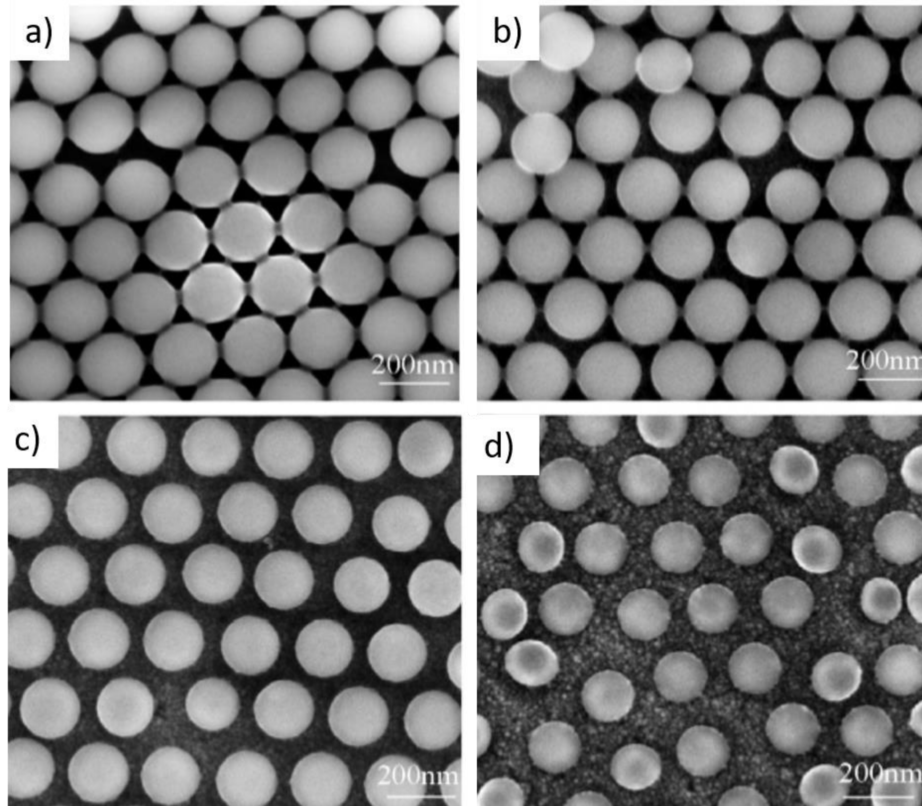

Figure 12. The diameter reduction of nominally 200 nm PS nanospheres via oxygen plasma treatment reported by Zhang et. al. (Source: Y. J. Zhang, Li, and Chen 2008) (a) 0 sec (b) 30 sec (c) 45 sec (d) 60 sec.

3.2. Fabrication of SiC Nanopillars by Nanosphere Assisted Etch Mask

The colloidal crystals of PS nanospheres have demonstrated favourable results as etch masks for dry-etching processes of easy-to-fabricate materials such as silicon. The field emission characteristics of large arrays of nanoscale silicon field emitters fabricated by nanosphere lithography have also been studied by different groups (W. Li et al. 2008; Cheung et al. 2006). However, PS nanospheres are not suitable etch masks for robust materials that require harsh etching procedures, for example the ICP-RIE processes where SF_6 gas is used. It has been shown that the PS nanoparticles completely disappear after a relatively short time of etching. Our experiments, where we used PS nanospheres directly as an etch mask yielded similar results reported in the literature (Cheung et al. 2006).

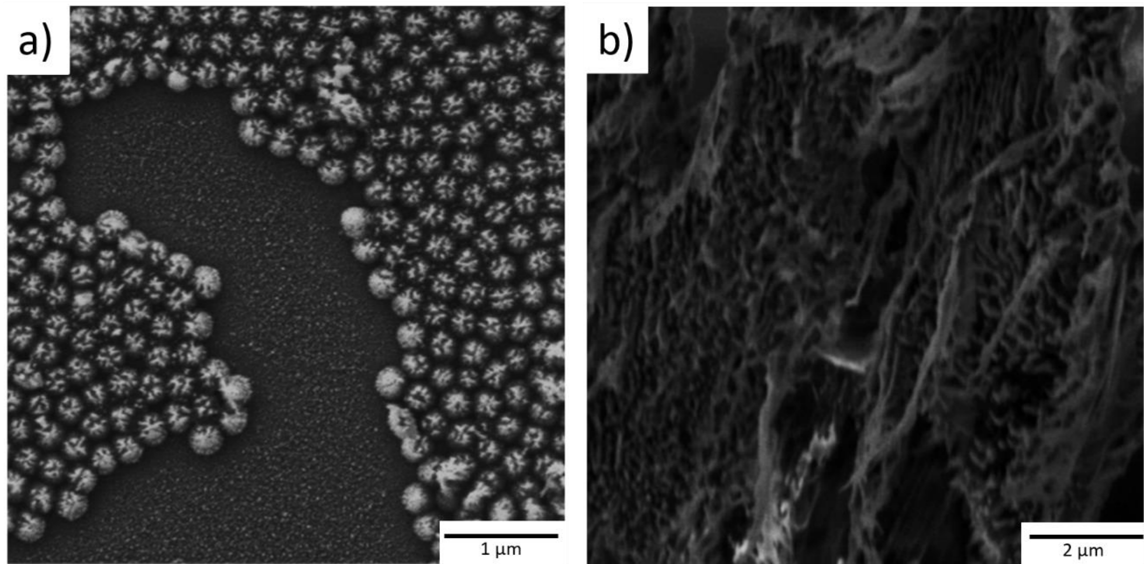

Figure 13. PS nanospheres as the etch masks for aggressive etch procedures of robust structures (a) 1 min after SF_6 plasma etching (b) 5 min after SF_6 plasma etching.

Figure 13 shows that the structure of the PS nanospheres start being destroyed in the first 60 seconds of SF_6 reactive ion etching, thus they are not suitable for the process. Due to its extraordinary chemical inertness, SiC is a robust material that is very hard to fabricate and is conventionally masked by Ni for dry etching applications. In such cases, the colloidal structures formed on the surface can be used as a template to deposit the desired material on the surface. In this work, we have proposed a way to print the colloidal crystal lattice acquired by PS nanospheres into Cr/Ni mask by a simple, mechanical method. The fabrication steps of the etch mask are illustrated in Figure 14.

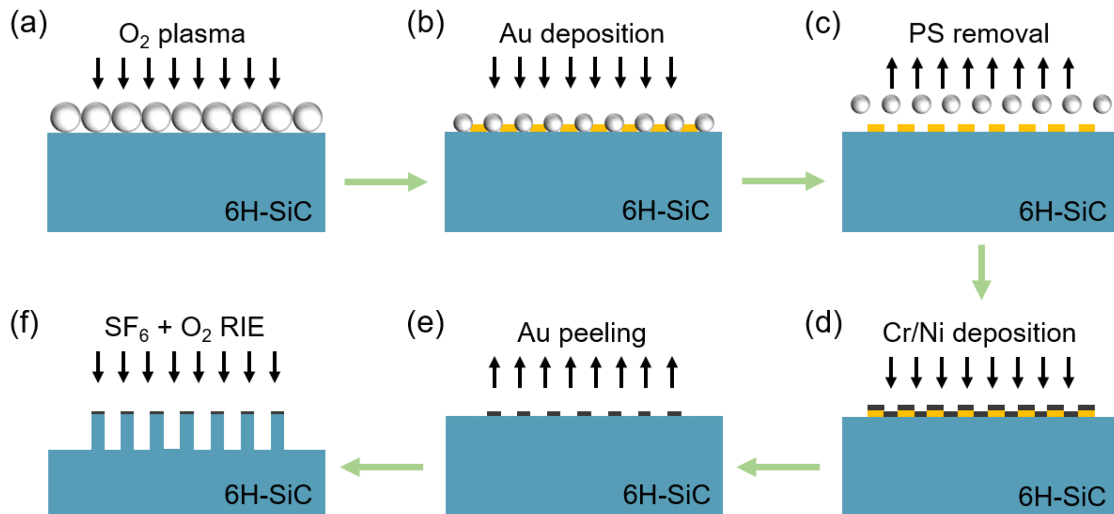

Figure 14. Nanosphere assisted fabrication steps for silicon carbide nanopillar structures.

SiC nanopillars were fabricated using a combination of NSL and inductively coupled plasma reactive ion etching (ICP-RIE) techniques. In the experiments, we used nominally n-type doped single crystal 6H-SiC wafer. As-received wafer was diced into 4 x 10 mm^2 rectangular substrates. Prior to the deposition of PS nanospheres, the substrates were cleaned chemically by solvents in an ultrasonic bath. Following the cleaning procedures, the samples were exposed to O_2 plasma in order to convert the hydrophobic character of the SiC surface into hydrophilic. The hydrophilicity of the surface is necessary for binding the hydroxyl group of PS nanospheres onto the SiC substrate. A solution of nominally 450 nm diameter PS nanospheres with 10% wt/v density in DI water is diluted by ethanol to get a volume ratio of 7:1. The prepared solution of PS nanospheres were spin coated on the surface of SiC substrate similar to that depicted in Figure 14.*a*. The diameter of the nanospheres was reduced by O_2 plasma with the parameters of 30 W power and 8.5 sccm O_2 flowrate (Figure 14.*a*). As the buffer layer which loosely attach on the SiC surface, a 40 nm thick Au thin film was thermally deposited on the samples (Figure 14.*b*) Then the samples were immersed in IPA and sonicated for 2 min to remove the nanospheres with reduced diameters, leaving behind an array of nanoholes on the SiC substrate (Figure 14.*c*). Following the nanosphere removal process, 10 nm/ 30 nm thick Cr/Ni film was deposited onto the samples (Figure 14.*d*). The Cr/Ni regions with soft Au base were peeled out of the SiC surface simply by a sticky tape. Thereby cylindrically shaped approximately 162 nm diameter Cr/Ni based nanodots were obtained (Figure 14.*e*)

to serve as a local hard-mask to protect the SiC regions underneath during the ICP-RIE process. The SiC substrate with Cr/Ni nanodots on its surface was etched by $SF_6 + O_2$ gas mixture in a ICP-RIE system. By means of the ICP-RIE process, nanopillars were successfully produced on the C-face surface of the SiC substrate (Figure 14.*f*). Every step during the SiC nanopillar fabrication process was verified by scanning electron microscopy (SEM) measurements. After the SiC based nanopillar fabrication, the samples were immersed into a conventional cheric ammonium nitride/perchloric acid based Cr etchant solution to remove any remaining traces of Cr/Ni mask.

The SiC nanopillar fabrication steps that are discussed in detail in the rest of this chapter are:

1. Self-assembly of PS nanospheres on C-terminated face of 6H-SiC
2. Modification of PS nanosphere diameter by O_2 plasma treatment
3. Preparation of the Au template
4. Evaporation of the desired etch mask material on Au template
5. Removal of the template and the creation of the etch mask
6. Fabrication of 6H-SiC nanopillars by ICP-RIE technique

3.2.1. Step One: Self-Assembly of PS Nanospheres on C-Terminated Face of 6H-SiC

NSL, which is a top-down technique, resides on highly ordered, 2D-pattern of these nanoscale spherical particles that forms via a bottom-up process, known as colloidal crystals. The formation of these structures on the surface is a self-assembly process, which by definition is the formation of an organized structure or pattern due to local interactions between the particles of an initially disorganized system. In other words, the special interactions between these nanospherical particles form a 2D hexagonally packed crystal structure when the required conditions are met. The nanospheres require some external forces such as gravity, interfacial forces and electric or magnetic fields to form self-assembled structures. This need is the result of inter-particle interactions (Zeng, Yu, and Lu 2010; J. Liu et al. 2017), such as van der Waals forces, electrostatic forces, capillary forces, and slow diffusion times.

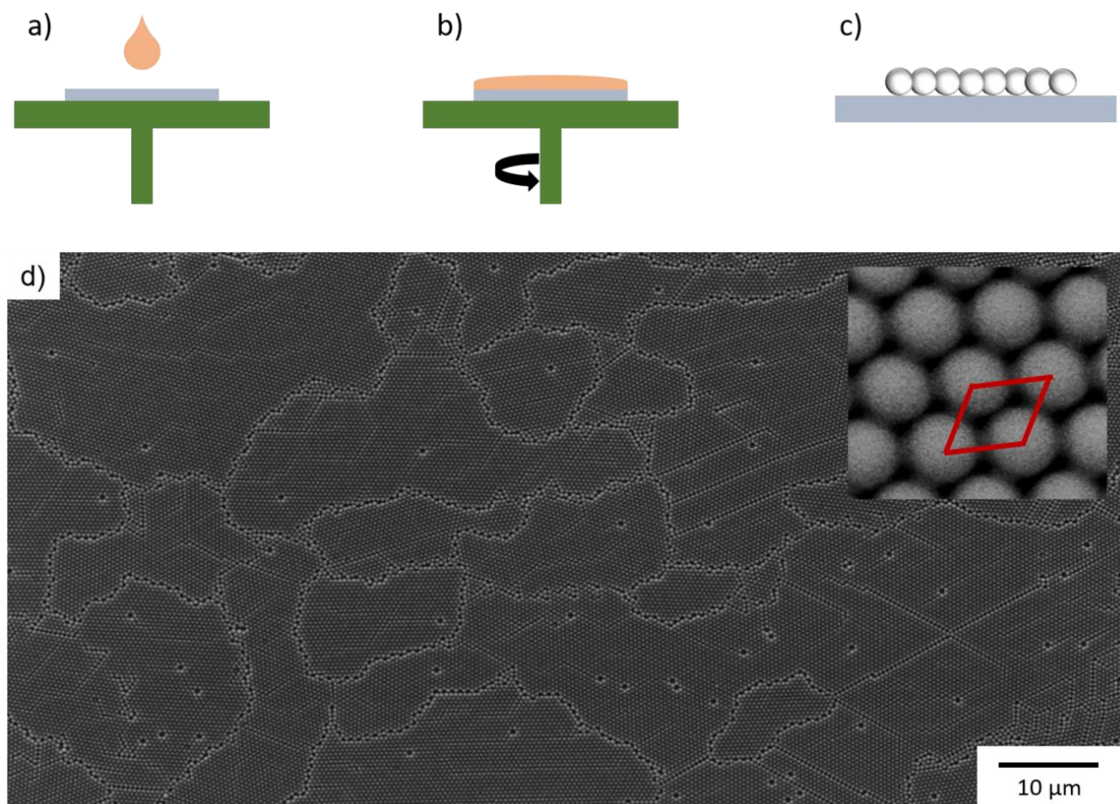

Figure 15. Schematic representation of spin coating process (a) dropping the solution on the substrate (b) spin coating (c) self-assembly of monolayer PS nanospheres (d) Large area self-assembly pattern after spin coating process (inset) the hexagonal packing of the PS nanospheres and the unit cell. The sample was prepared at Quantum Device Laboratory and SEM measurements were done at the Centre for Materials Research in IZTECH.

There have been proposed various techniques to acquire the self-assembly pattern that results in hundreds of micrometres squares of colloidal crystal structure on the sample surface. The topmost used techniques are sedimentation (P. N. Pusey 1987; J. Zhu et al. 1997), evaporation methods (Jiang et al. 1999), dip coating (Meng et al. 2002), Langmuir-Blodgett coating (Rybczynski, Ebels, and Giersig 2003; Weekes et al. 2007), electrophoretic deposition (M. Holgado et al. 1999; Rogach et al. 2000) and spin coating (J. Chen et al. 2013).

In our experiments, we have used spin-coating method to form a large area colloidal crystal structure on the C-terminated face of n-type 6H-SiC wafers. This method is chosen because it is the fastest technique to create large area, monolayer 2D crystal structure on the surface.

Spin coating method (Figure 15) is a commonly used, fast and easy method to acquire hexagonally packed arrays of colloidal particles on the substrates. In this technique, a wafer with hydrophilic surface is placed inside a spin coater and an excessive amount of suspension of nanospheres is applied. Then the wafer starts being rotated at high speeds. The rotation disposes the excessive amount and evenly spreads the suspension on the wafer due to centrifugal force. As a very thin film of the suspension remains on the surface, the rotation continues and accelerates the evaporation of the solvent; as a result, increasing capillary forces creates a highly-organized hexagonal 2D crystal structure on the surface. In this technique, layer thickness depends on various parameters. As for the suspension, the concentration of nanospheres inside the solution, the nature and the amount of the solution delivered become important and for the spin coating process, the rotation speeds and times become crucial to define the layer thickness, from monolayer up to a few layers, acquired on the substrate. Last but not least, the wettability of the substrate plays the key role to achieve the self-assembly structure on the substrates.

Prior to the experiments, n-type 6H-SiC substrates with the dimensions of 4 mm x 10 mm were cleaned in acetone, isopropanol (IPA) and deionized water in the given order by sonication for 15 min. to get rid of any unforeseeable effects of possible contaminants on the wafer surfaces, and dried by N_2 airflow. The surface of 6H-SiC is initially hydrophobic, which is unsuitable for self-assembly of PS nanoparticles. Thus, a surface modification is a necessity. Such modification that introduces hydrophilic character on the surface is possible by various wet and dry techniques (Bodas and Khan-Malek 2007; S. Bhattacharya, A. Datta, J. M. Berg 2005). In this thesis work, we have used oxygen plasma reactive ion etching (O_2 RIE) to achieve surface hydrophilicity.

RIE is a dry etching procedure where a combination of mechanical and chemical etching is observed. It is a highly directional procedure that resides on ion bombardment by a chemically reactive plasma to create anisotropic etch profiles which is crucial for manufacturing microelectronic devices. The plasma is created under vacuum by an applied electrical field and high energy ions interacting with the wafer surface etches the substrate. This technique allows faster fabrication of desired structures on the surface with minimal loss in the horizontal direction.

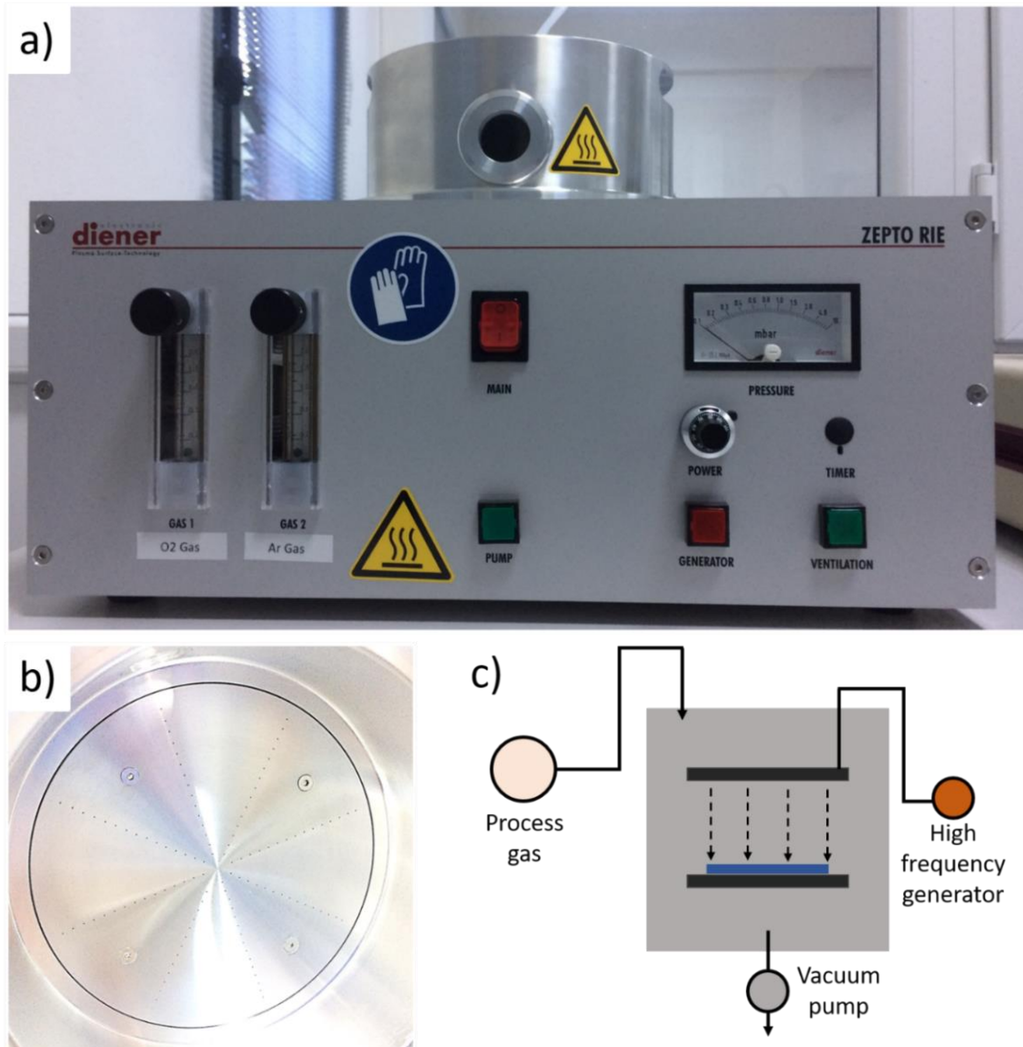

Figure 16. (a) Our plasma system (Diener Zepto RIE, 50 W) in the Quantum Device Laboratory (b) The gas inlets on the lid (c) Schematic representation of an RIE system.

The schematic representation of a typical RIE system is shown in Figure 16.*c*. The system is composed of a vacuum chamber that contains a parallel plate to apply electric field and a wafer holder. The pressure inside the RIE system is adjusted both by the vacuum pump and by the gas flowrate. The gas is introduced to the chamber via small inlets at the top of the chamber and plasma is created by a strong applied electrical field between the parallel plates. The plasma ions are then accelerated under the influence of electric field and collides with the wafer surface. Those high energy ions remove atoms from the surface both by chemical and physical interactions. The removed atoms and the remainder of the plasma are drawn away from the system by the vacuum pump. The process gases should be chosen to meet the requirements of the desired application.

In the Quantum Devices Laboratory, we use Diener Zepto RIE low pressure plasma system for plasma treatment applications (Figure 16.*a*). The cylindrical vacuum system has a diameter of 190 mm and height of 60 mm with 1.7 lt volume. There is a borosilicate glass on the chamber wall that allows us to observe the plasma formation inside the chamber. The process gases are introduced in to the chamber via small openings evenly distributed at the top of the chamber (Figure 16.*b*). Such distribution is required to achieve a homogenous plasma formation everywhere inside the vacuum chamber. There are two channels to introduce the process gases, such as high purity O_2 and Ar in our system, into the vacuum chamber. The pressure at the entrance of the needle valves is manually adjusted below 1 atm to protect needle valves. The gas flow rate into the chamber, thus the process pressure is adjusted by two stainless steel needle valves. The plasma generator has 60 kHz frequency and a power of 50 W. The power of the plasma can be adjusted by 0.5 W precision. Edwards RV-12 rotary pump is connected into the vacuum chamber and the base pressure that can be reached without the process gas flow is 0.15 mbar. The typical pressure range under 0.5 lt/h of oxygen flow into the chamber is 0.3 mbar. When the pressure inside the vacuum chamber exceeds 2 mbar, the self-protection system cuts off generator power and the plasma cannot be created. The pressure inside the chamber is measured by a Pirani sensor.

O_2 RIE is conventionally used to clean wafer surfaces from organic contaminants via chemical reactions and to introduce hydrophilic characteristics on the surface via binding hydroxyl groups. But it has been also shown that O_2 plasma treatment can modify the surface hardness and roughness (Alam, Howlader, and Deen 2014). Surface roughness is a crucial factor for self-assembly procedures and directly affects the quality of the crystal lattice on the surface. Thus, O_2 RIE parameters should be carefully determined. It is important to note that different substrates require different O_2 RIE parameters to reach the desired results; thus the parameters should be revisited once a different surface is being studied.

After the cleaning process, the wafers were placed into Diener Zepto RIE system and the rotary pump was started. When the system reached the base pressure of 0.1 mbar, which is around 15 min. later, the power was adjusted to 40 W and the O_2 gas was introduced to the system. After the gas flow of 0.5 lt/h and the pressure inside the system reached the equilibrium, the generator is started to form oxygen plasma inside the chamber. After 20 min. of treatment, the generator is stopped, the gas flow is cut and the pump was turned off.

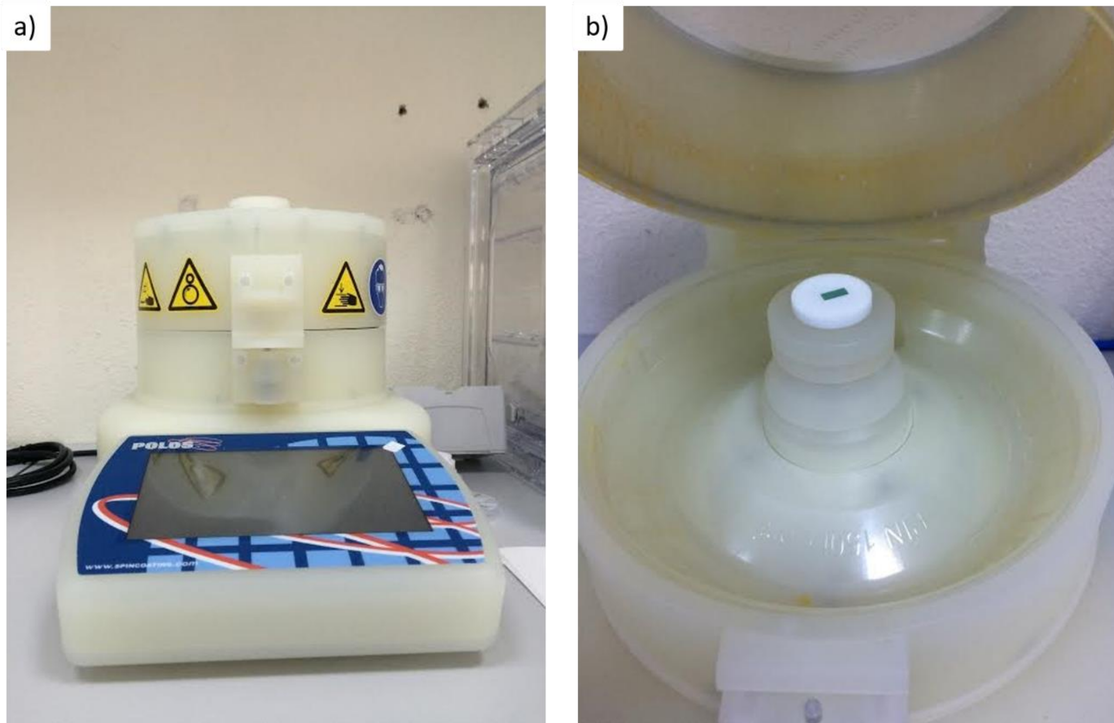

Figure 17. (a) Polos SPIN 150i Spin Coater System in the Quantum Device Laboratory (b) 6H-SiC sample placed inside the spin coater.

Table 5. Optimized O_2 plasma treatment parameters for surface hydrophilicity of C-terminated face of 6H-SiC wafers.

Treatment	**Process Gas**	**Power (W)**	**Gas Flowrate (lt/h)**	**Process Time (sec)**	**Pressure (mbar)**
Surface hydrophilicity	O_2	40	0.5	1200	0.3

The vacuum was broken by introducing N_2 flow and samples were taken outside of the chamber. The optimized parameters for O_2 plasma treatment of the C-terminated face of 6H-SiC are summarized in Table 5.

In order to create the desired mask on the surface, PS nanospheres with nominally 450 nm diameter diluted in 10%wt solution in DI water were used. The suspension is sonicated for 20 min. for even decollement of the particles. The PS suspension was further diluted with ethanol by a volume ratio of 7:1. Introducing ethanol not only dilutes the solution further, but also helps the solution to dry out faster during the spin coating

process; thus influences the formation of the colloidal crystal. This diluted suspension was also sonicated for 5 min. to achieve homogeneity. After that, the wafers were placed inside the spin coater.

The spin coating process was done by table-top Polos SPIN 150i Spin Coater system shown in Figure 17. The spin coater is made of polypropylene which is compatible even for aggressive chemicals. The lid of the spin coater uses an electromagnetic lock that is controlled by the device processor; thus the spin coating process cannot be started if the lid is open. This property adds additional safety in case of using of corrosive chemicals. It is possible to create recipes with infinite number of steps and restoring these created recipes inside the set-up. The integrated touch screen allows an easy control during creation and application of the desired recipes. The rotation speed can be adjusted between 0-12000 rpm, and the acceleration can be set separately between 0-30000 rpm for each step in the recipe. There is also no maximum time limitation for the steps and the minimum time for each step is given low as 0.1 sec. BF-S2500 diaphragm pump is attached to the system to hold the wafers on the chunk during spin coating procedure.

After placing the wafers, the pump was turned on to make sure the wafer is placed well on the chunk and the vacuum can hold the wafer properly (Figure 17.*b*). After that step, the lid was closed and 20 µl of the evenly distributed suspension was drop-casted via a micropipette from the opening on the coater lid. And the recipe was started. We used a three-step spin coating procedure to acquire an evenly distributed, large area self-assembly pattern on the surface. After the solution is dropped, the wafer started being rotated at a speed of 400 rpm with an acceleration rate of 400 rpm/sec. The slow rotating speed at the start of the procedure lets the dropped suspension spread to the surface evenly. After 20 sec., the rotation speed went up to 1000 rpm with an acceleration rate of 1000 rpm/sec. The second step with slightly higher speed helps getting rid of the excess suspension on the surface. This step is crucial, because at higher rotation rates, the amount stays on the surface due to wettability becomes too low to create large area crystallization on the surface. A little more than just the right amount of particles should be resting on the surface at this time. Also here, by the thinning of the coated layer, the evaporation rate increases, which in return, increases the capillary forces that creates the hexagonal lattice. In our case, 20 sec. of 1000 rpm rotation was enough to create the desired structure on the surface. For the 30-second-long last step, the rotation speed was increased to 4000 rpm with 4000 rpm/sec acceleration rate.

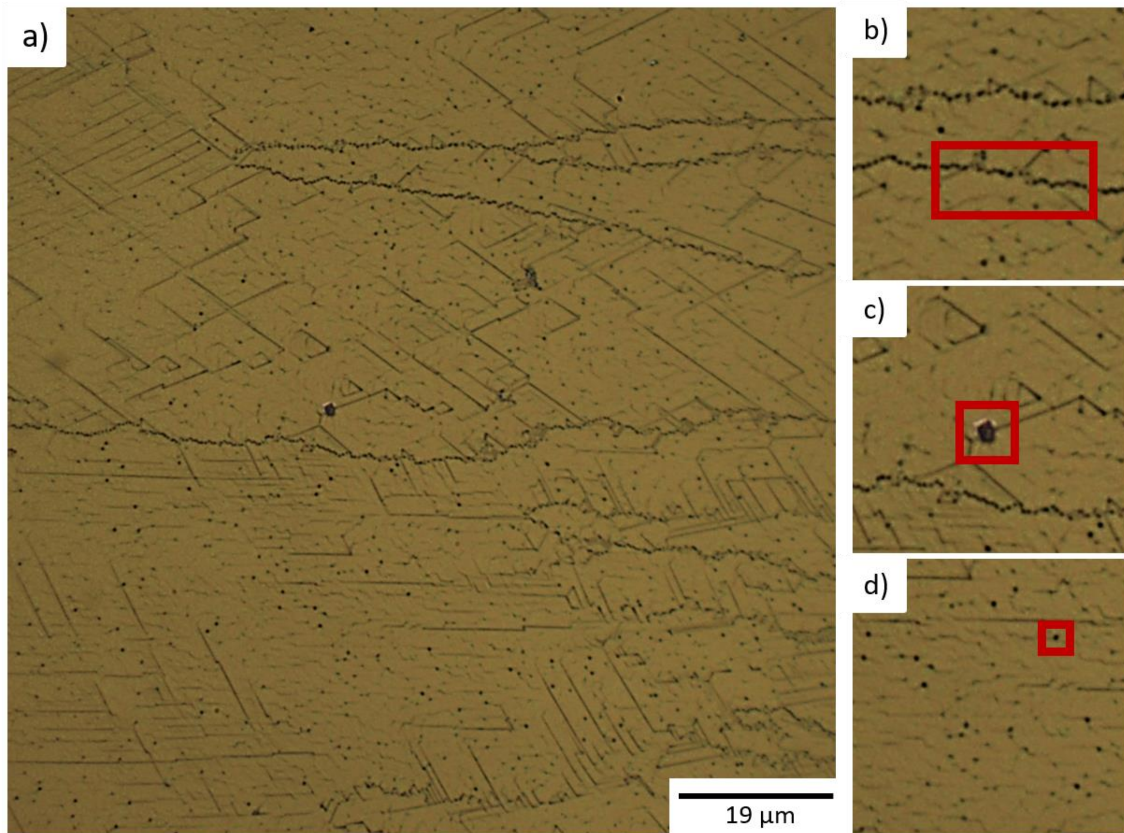

Figure 18. (a) Large area optical microscope image of the sample surface (b) the grain boundaries (c) a small multilayer formation (d) crystal lattice defects.

Table 6. The spin coating parameters for self-assembly of 450 nm PS nanospheres on C-terminated face of 6H-SiC wafer

Step	Rotation Speed (rpm)	Rotation time (sec)	Acceleration (rpm/sec)	Purpose
1	400	20	400	Even distribution of the drop-casted suspension on wafer
2	1000	20	1000	Thinning of the evenly distributed solution and promoting evaporation of the liquid to acquire self-assembly pattern
3	4000	30	4000	Getting rid of multilayer formations on the surface and evaporating the remainder fluid

This high rotation speed is crucial to get rid of most of the multilayer stacking that might occur throughout the surface and to evaporate the remainders of the liquid. A summary of the spin coating parameters is given in Table 6.

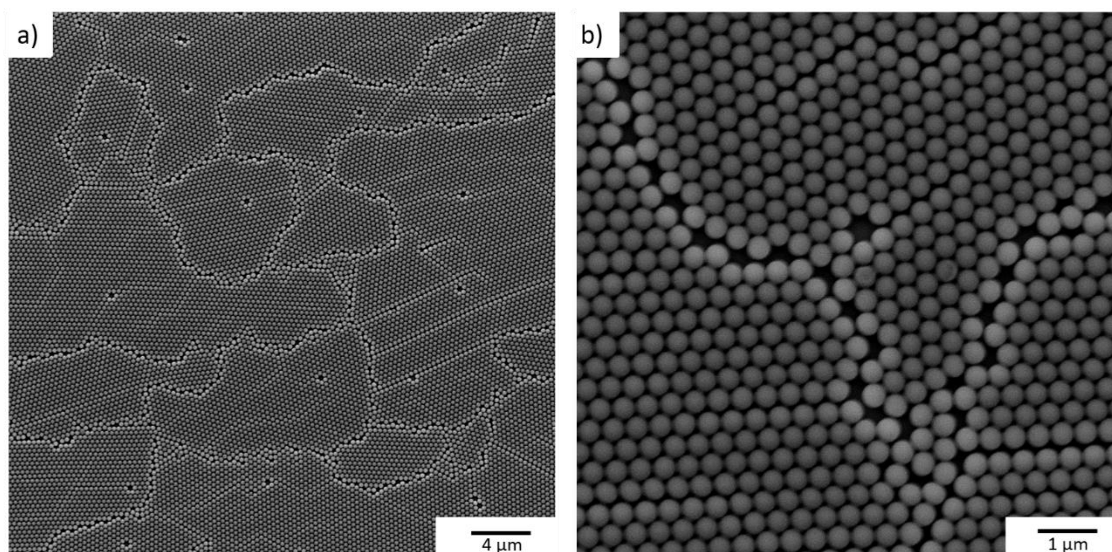

Figure 19. SEM measurements at different magnifications taken from the self-assembly structure formed on C-terminated face of 6H-SiC.

After the spin coating procedure, the wafers were firstly examined under optical microscope, and then, further examination was carried out via a scanning electron microscope (SEM).

For nanospheres with 450 nm diameter, the optical microscope images are capable of providing a solid foresight about the 2D colloidal lattice formed on the surface. Not only the grain boundaries, the empty and multi-layered areas are clearly visible, but also the defects in the crystal lattice can be understood.

First, the self-assembly pattern was observed by using an optical microscope (Figure 18), and then the further examination of the self-assembled PS nanosphere layer was carried out by SEM measurements also proved the foresighted indications right. (Figure 19)

Statistical analyses were done from the acquired SEM images. Our analyses revealed a nanosphere concentration of 3.9 x 10^7 cm^{-2}. The abovementioned steps optimized for our surface has shown that throughout the wafer, hundreds of micrometre squares of continuous 2D-hexagonal crystal lattices are formed on well-prepared wafers via an only 70-second-long spin coating process. The ease and the speed of such large-area fabrication manifests that nanosphere lithography is, indeed, an undoubtedly preeminent nanofabrication technique with high-throughput.

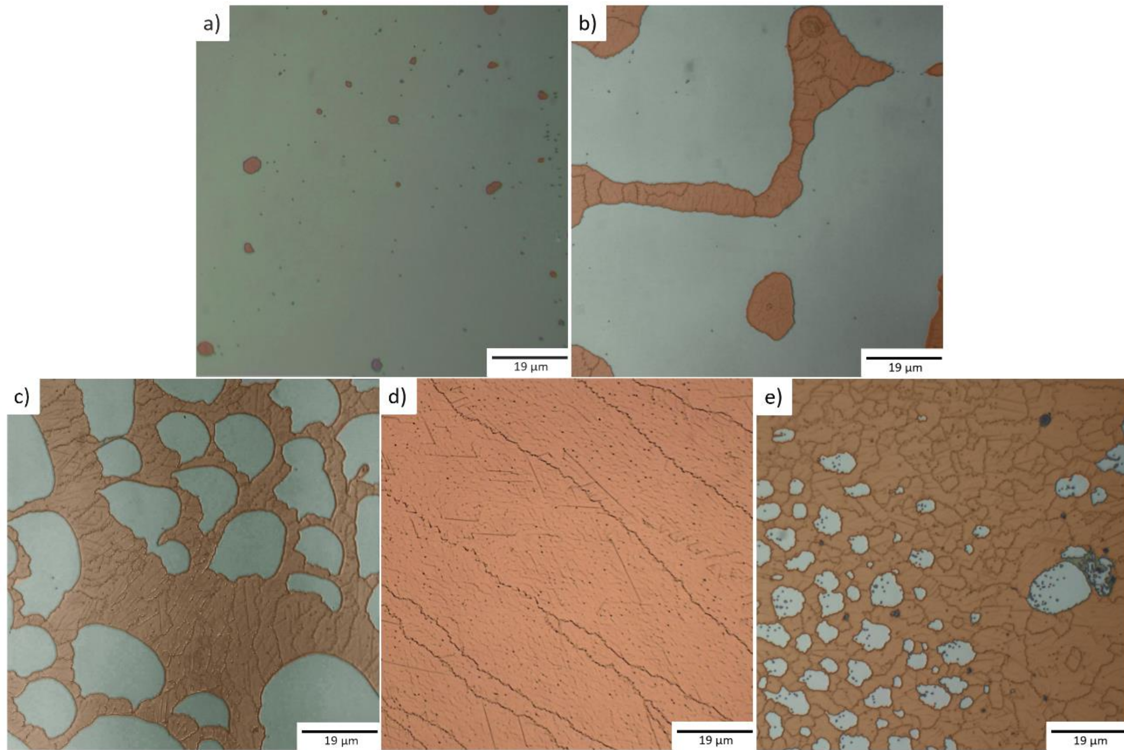

Figure 20. Optical microscope images of the surface concentration of the spheres after spin coating the solution with an initial suspension:ethanol volume ratio of (a) 1:2 (b) 1:1 (c) 3:1 (d) 7:1 (e) 1:0.

We have also examined the effect of particle concentration and the effect of spin rate at the third step of spin coating process on the self-assembly pattern formed on the surface. It is important to note that there are so many parameters that affects the self-assembly formation on the substrates. The decrease in the nanosphere size, for example, increases the interactions between the particles, or the change in the surface properties of the wafer used might have different effects on the colloidal crystal formation. The parameters also are closely connected, thus change in one parameter requires revisiting the rest of the pre-determined parameters.

3.2.1.1. Effects of Particle Concentration

The particle concentration in the drop-casted suspension is an important parameter to acquire large-area crystallization on the surface. Typically, PS nanospheres are sold as a suspension with 10%wt concentration in DI. This concentration is further diluted by

using ethanol or isopropyl alcohol. Introduction of these species inside the suspension also accelerates the evaporation rate of the liquid during the spin coating procedure.

The effect of concentration is studied to acquire the largest area of crystallization on the wafer surfaces for the abovementioned optimized spin parameters because the number of the nanospheres and their distribution are both crucial parameters for fabricating field emitter arrays for practical applications. Figure 20 shows the optical microscope images of surfaces that were spin coated by prepared suspensions with different concentrations.

It is clear from Figure 20 that as the concentration of the suspension increases up to 7:1, the concentration of the particles on the surface increases. But as the concentration reaches to 1:0, there is a decrease in the area of the self-assembly pattern. The reason to this seemingly contrary fact is the increase of the evaporation rate in the presence of ethanol inside the suspension. In 1:0 case, the 20 sec. second step of coating procedure with 1000 rpm was not enough to evaporate enough amount of liquid from the surface. Thus, the third step with 4000 rpm resulted in scattering of the spheres and the liquid out of the wafer. For such instances, the increase in the duration of the second step provides more feasible results.

3.2.1.2. Effects of Spin Coating Parameters

The effect of the spin speed of the third step is also studied by means of optimizing the acquired structure on the surface. Figure 21 displays the optical microscopy images for three samples and the spin coating parameters applied on them for a volume ratio of 7:1 suspension, ethanol solution is given in Table 7.

The third step with 8000 rpm is found to be too aggressive for the self-assembly process to occur on the surface. As can be seen in Figure 21.*a,* the nanospheres are scattered and thus could not assemble together due to high rotation speed. And for 2000 rpm as the last step, the relatively large area monolayer formation on the surface was observed.

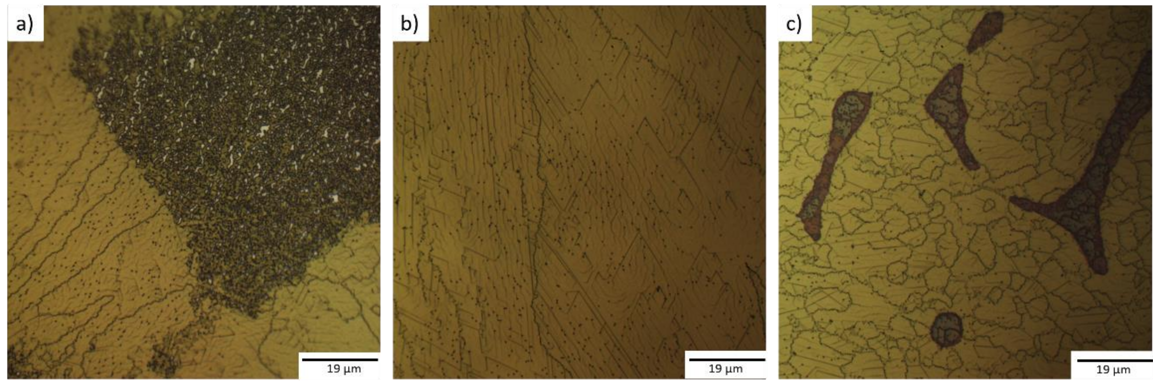

Figure 21. Optical microscope image of the surface of (a) Sample 1 (b) Sample 2 (c) Sample 3.

Table 7. The spin coating parameters used for the samples.

Sample	Spin 1 (rpm)	Time 1 (sec)	Spin 2 (rpm)	Time 2 (sec)	Spin 3 (rpm)	Time 3 (sec)
1	400	20	1000	20	8000	30
2	400	20	1000	20	4000	30
3	400	20	1000	20	2000	30

3.2.2. Step Two: Modification of PS Nanosphere Diameter

In order to create stand-alone structures on the surface that the nanopillars will be formed underneath, the nanospheres that form the colloidal crystal structure on the surface should be etched in a manner to reduce their diameters. Such etch is possible with O_2 plasma treatment, due to its high directionality and the ability to chemically etch the organic materials like PS (Fredriksson et al. 2007). We have carried out a set of experiments to determine the effect of O_2 plasma treatment duration on the reduction of PS nanosphere diameter on the surface. The experiments showed that the sequentially applied sets of O_2 plasma treatment with a predetermined duration allows a better control on the reduction rate of the PS nanosphere diameter. In other words, instead of applying a 5 min. O_2 plasma directly on the substrate, applying two sets of 2.5 min of O_2 plasma allows a more controlled reduction of the sphere diameter.

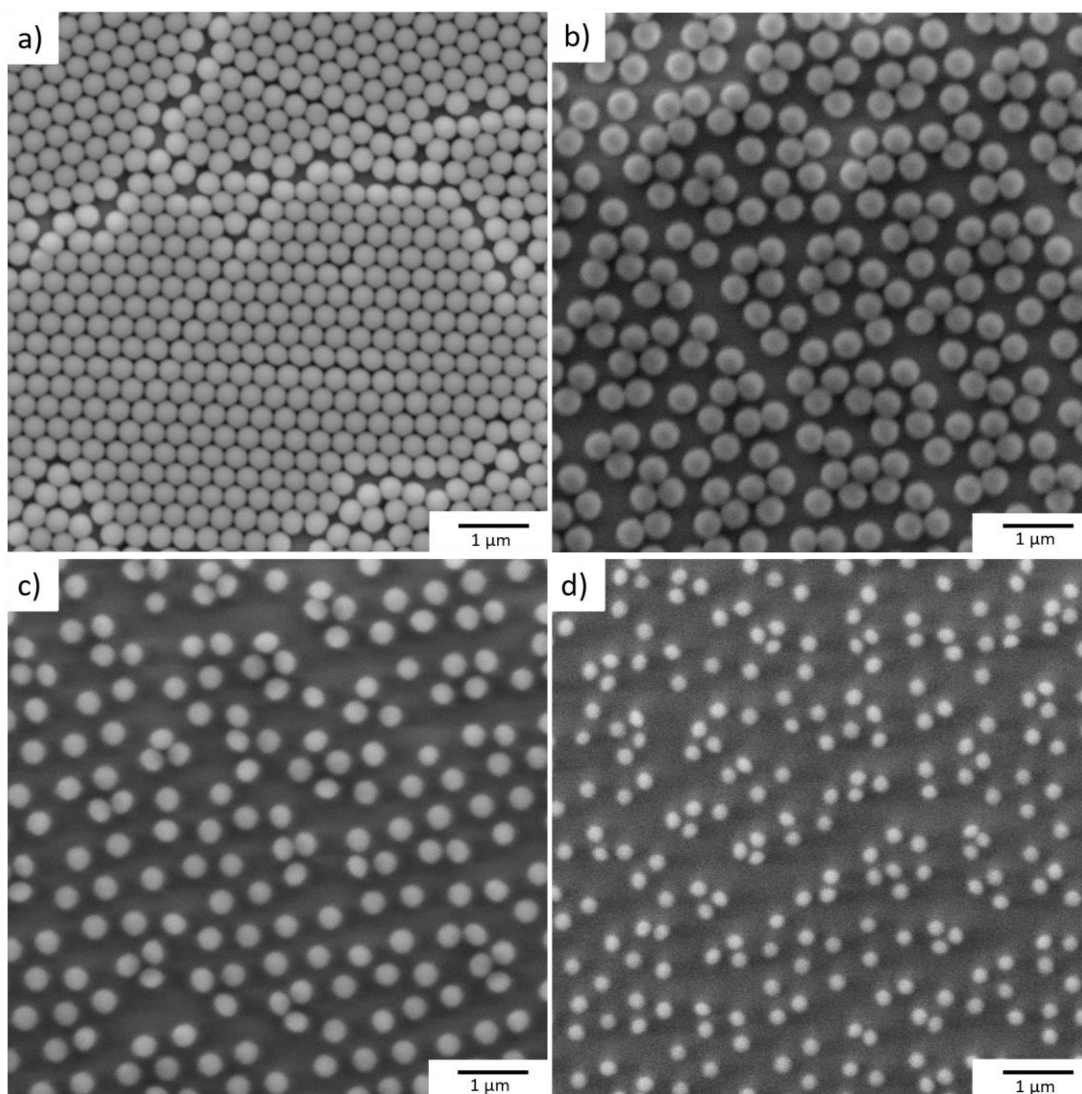

Figure 22. SEM images of the nanospheres after (a) 0 sec. (b) 150 sec. (c) 300 sec. (d) 450 sec. of O_2 plasma treatment.

Table 8. The statistics on the diameters of the nanospheres after the oxygen plasma treatment up to 3 sets.

Time (sec)	**Number of sets**	**Min. Diameter (nm)**	**Max. Diameter (nm)**	**Mean Diameter (nm)**	**Standard Deviation (nm)**
0	0	429	466	452	10
150	1	356	388	378	7
300	2	288	310	300	5
450	3	125	166	146	8

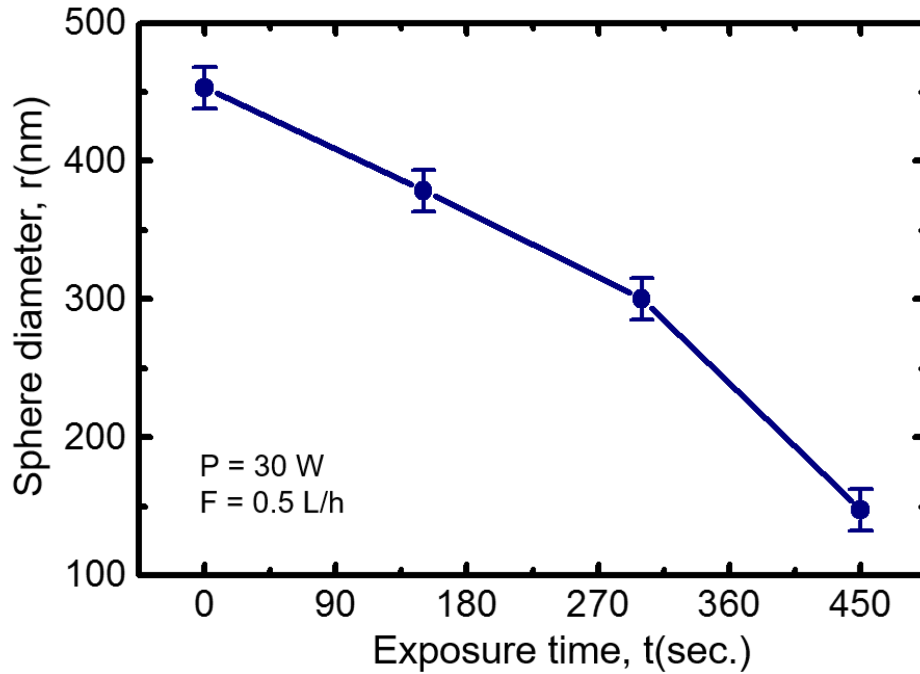

Figure 23. The change of PS nanosphere diameter as a function of O_2 plasma exposure time.

The O_2 plasma etch rate experiments were carried out under 0.3 mbar pressure, at plasma power of 30 W and the oxygen flowrate of 0.5 lt/h. The predetermined treatment duration was set to 2.5 min. The samples were then examined by SEM (Figure 22). It is seen that after 3 sets of O_2 plasma, the sphere diameter was reduced to 146 nm. The fourth set of O_2 plasma was also applied, but the last set cleaned all the nanospheres on the wafer surface.

By using the acquired measurement data from SEM, the statistics of the nanosphere diameters on the surface was studied and the results are given in Table 8. The change of the PS nanosphere diameter as a function of O_2 plasma exposure time was shown in Figure 23.

The best results, by means of the proposed mask production in this work, was obtained via 300 nm PS nanosphere diameter. Thus, after the self-assembly pattern was obtained on the C-terminated face of 6H-SiC, the wafers were exposed to 2 sets of 2.5 min long oxygen plasma with abovementioned parameters, to obtain individual PS nanospheres with diameters of 300 nm.

3.2.3. Step Three: Preparation of Gold Template

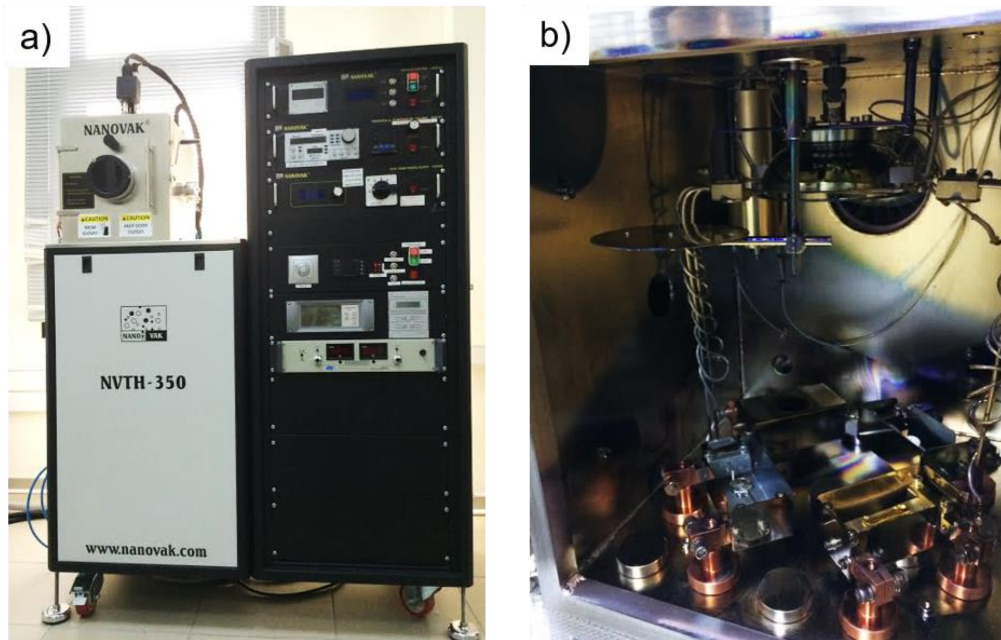

Figure 24. NVTH-350 Thermal Evaporation System in Quantum Device Laboratory (a) the system as a whole (b) inside the vacuum chamber.

For now, the desired etch mask structure where the nanopillars should form is acquired on the surface, but as mentioned above, the PS nanospheres are not suitable for the required etch procedure of SiC wafers. Thus, a sacrificial layer is necessary for being used as a template to produce this exact pattern as a Cr/Ni shadow-mask. Because of this fact, we decided to use Au thin film as a sacrificial layer, since it loosely attaches on the native oxide layer forms on both faces of SiC and it can be easily removed mechanically by the help of a conventional sticky tape.

In order to create the Au template on the surface, a 40 nm thick Au thin film was coated on the surface by using a vacuum thermal evaporation system.

In our laboratory, we use Nanovak NVTH-350 Thermal Evaporator system (Figure 24) for the thermal evaporation experiments. Our thermal evaporator has 4 separate pots that were placed at the bottom four corners of the stainless steel cubic vacuum chamber. The sample holder is placed in the middle of the chamber at the top and can be rotated during the coating process. At each side of the sample holder, there are two quartz microbalance crystals at the same height as the samples to determine the thickness

of the coated material via calculations based on inserted values for the evaporated materials. There are one Edwards RV8 rotary pump and one Edwards nEXT 2400 160 W turbo-molecular pump attached to the system and the base pressure of our system is low as 4 x 10^{-7} mbar. There are three control units, namely vacuum control, thickness and temperature control and power supply. Vacuum control unit measures the initial pressure via INFICON MPG400 vacuum gauge, starts and stops the pumps and controls the venting procedure. The control system is also responsible for initiating the chiller, ISISO MPC 34, 15 min. after the pump button is pushed. The thickness and temperature control unit is composed of a PID temperature controller, attached to a thermocouple placed at the back of the sample holder, and INFICON SQM 160 thin film deposition monitor that reads and converts the values obtained according to the pre-set data for the material being evaporated by the two quartz crystals. The PID controller also controls the light bulbs attached at the back of the sample holder, at the top of the chamber to heat the samples before and/or during the coating procedure. The power supply acquires resistive heating of the one of the four pots inside the chamber and thus the evaporation of the material.

For Au thermal evaporation, tungsten boat is placed at the fourth pot inside the vacuum chamber, 0.27 grams of high purity (99.9%) gold purchased from Istanbul Gold Refinery was cut into small pieces and placed inside the inserted boat. The samples were placed tightly on the sample holder, and the sample holder was mounted to the rotating holder stage. The lid was closed and the rotary pump was started. The system automatically starts the turbo molecular pump after the internal pressure is down to 8.5×10^{-1} mbar, then automatically starts the chiller 15 min. after the pumping process is initiated. When the pressure inside the vacuum chamber reached 2 x 10^{-6} mbar, usually 1 hour after the pump starts, the pre-set program values were introduced to the thickness monitor and the thickness of the gold film was adjusted to 40 nm. After this step, the desired pot (pot 4) was selected via the pot switch and the heating was initiated via applied current. Au usually starts evaporating at an applied current of around 55 A with a rate of 0.1 Å/s. The desired rate for this procedure is 0.6 – 1 Å/s which requires currents high as 70-75 A. The current was risen slowly in order not to break the boat up to 70 A, where the quartz crystals read 0.6 Å/s evaporation rate, the shutter that was covering the samples were opened and the pre-read values when the shutter was closed were erased by “Zero” button on INFICON SQM 160. The shutter was automatically closed after the desired thickness was reached and the current was slowly reduced down to 0. The system was

closed and the samples were taken out after the vacuum was broken with N_2 gas flow. The parameters for the Au evaporation is summarized in Table 9.

In order to create the desired template, the nanospheres should be removed away from the sample. In this case, the Au layer deposited will have the inverse pattern as the removed nanospheres will leave holes behind where they were. In order to remove the nanospheres, the samples were sonicated in IPA for 90 sec. This procedure removed most of the spheres from the surface and left behind the template we desired as shown in Figure 25.*a*. The duration of this procedure is vital, because the gold also loosely attaches to surface and can be removed by prolonged periods of sonication.

Following the PS nanosphere removal process, the examinations were done on the surface by optical microscopy and SEM. The measurements showed that the desired template mask is acquired on the surface by Au thermal evaporation and most of the PS nanospheres have left the surface. It is clearly seen on the SEM image (Figure 25.*d*) that the diameter of the PS nanospheres and the acquired voids on the Au does not have the same diameter. This is a result of the design of our thermal evaporation system. As mentioned above, the evaporation pots are placed at the corners and the evaporated material reaches the surface with a certain angle different from 90°. This fact, combined with the radius of curvature of the spheres have resulted in a finer structure than previously expected. This result is favourable in our case because the finer the mask on the surface, the higher aspect ratios are possible.

In order to acquire even finer structures on the surface, a set of experiments were carried out with nanospheres exposed to 3 sets (7.5 min. in total) oxygen plasma treatment. We found that the nanospheres with 148 nm diameter could not be removed from the evaporated Au layer. The prolonged sonication procedure removed the Au template from the surface.

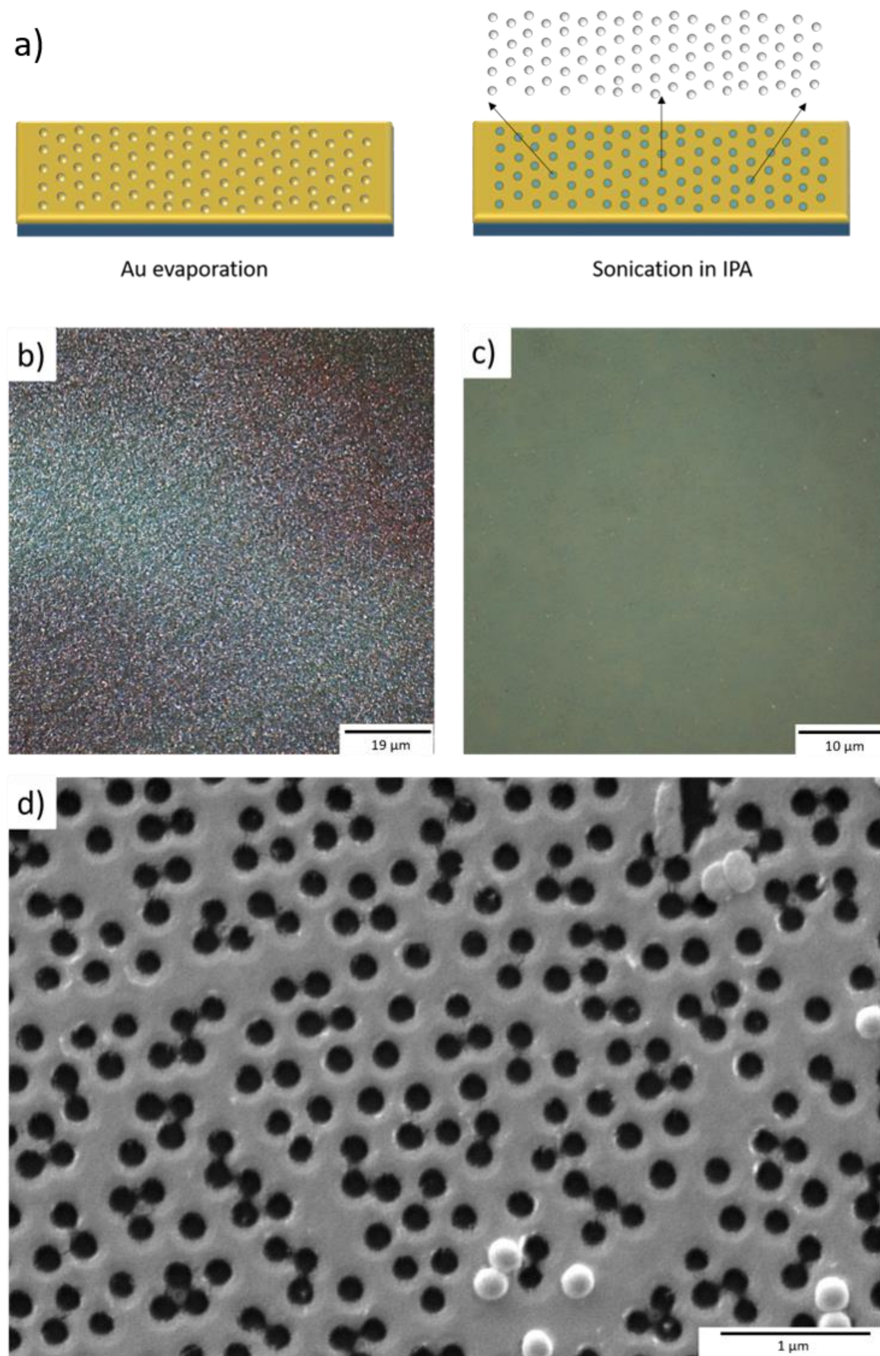

Figure 25. (a) The schematics of Au template production (b) Optical microscope image of Au coated PS nanospheres on the C-terminated face of 6H-SiC (c) After 90 sec. of sonication (d) SEM image of the Au template.

Table 9. The Au evaporation parameters.

Material	Pressure (mbar)	Current (A)	Rate (Å/s)	Thickness (nm)	Final Temperature (°C)
Au	2×10^{-6}	60	0.6	40	38

3.2.4. Step Four: Evaporation of Cr/Ni Etch Mask Material on Au Template

Table 10. The oxygen plasma treatment parameters for surface cleaning.

Gas	Power (W)	Flowrate (lt/h)	Duration (sec)	Pressure (mbar)
O_2	40	0.5	300	0.3

Table 11. Evaporation parameters for Cr and Ni.

Material	Pressure (mbar)	Current (A)	Rate (Å/s)	Thickness (nm)	Final Temperature (°C)
Cr	2×10^{-6}	60	0.2	10	62
Ni	1.2×10^{-6}	22	0.4	30	65

Nickel (Ni) masks are conventionally used for dry etching procedures of robust SiC material. Since there is an Au template on the surface with desired pattern, Ni can be evaporated on the surface. We evaporated an additional 10 nm Cr on the surface to stick the evaporated Ni on the surface.

Any left-over organic components on the surface might affect the sticking of Cr, thus of mask, to the substrate, so an additional 5 min O_2 plasma treatment was applied to get rid of any possible remainder of PS nanospheres prior to the evaporation procedure. The oxygen plasma treatment parameters are given in Table 10.

After the cleaning procedure, the samples were inserted in to NVTH-350 Thermal Evaporator. A tungsten basket was attached to Pot-1 for Cr and an alumina coated tungsten basket was attached to Pot 3 for Ni evaporation. A 99.9% purity Cr was loaded on to the tungsten basket and 99.9% purity Ni was loaded to the alumina coated tungsten basket. The pumps were then started. After the pressure inside the chamber reached 2×10^{-6} mbar, firstly 10 nm of Cr, then 30 nm of Ni was evaporated on the sample and then the samples were taken out of the evaporator. The evaporation parameters of Ni and Cr are given in Table 11.

3.2.5. Step Five: Removal of the Template and the Production of the Cr/Ni Etch Mask

The last step is the removal of the template layer to reveal Cr/Ni based nanoislands on the exact spots where the nanospheres once were. Since the Au template is loosely attached on the surface, and the Cr layer holds Ni and the SiC together at the voids, the template can be easily removed by using a sticky tape. For the experiments, we used a conventional silicon tape. The tape was cut in desired length, usually a few millimetres longer than the width and the height of the sample, and then was placed on the evaporated materials. A pressure to help the tape stick evenly on the surface is applied for about 10 seconds. Afterwards, the tape was peeled off with the Au layer. The Cr held the Ni cylinders on the surface, so the etch mask was fabricated. The optical microscopy and the SEM images of the produced mask is shown in Figure 26.

The SEM images revealed that the resulting Cr/Ni nanoislands on the surface has an average diameter of 162 nm. The statistics done on the nanoislands via SEM images are shown in Table 12.

The parameters given here are the optimized parameters for the proposed printing process. Although we tried acquiring thicker masks, but it becomes challenging to get with this technique due to various reasons. Firstly, for a thicker mask, a thicker Au layer is required, which needs a prolonged sonication process to remove the PS nanospheres underneath. Up to 80 nm of Au thickness, the spheres can be removed enough to satisfy a good resulting void density on the surface. But we could not remove the template after 20/60 Cr/Ni evaporation via sticky tape. Thus, a modification is required in order to apply this technique for thicker etch masks. We think that a controlled chemical etching of the Au template via an iodine solution may solve this problem.

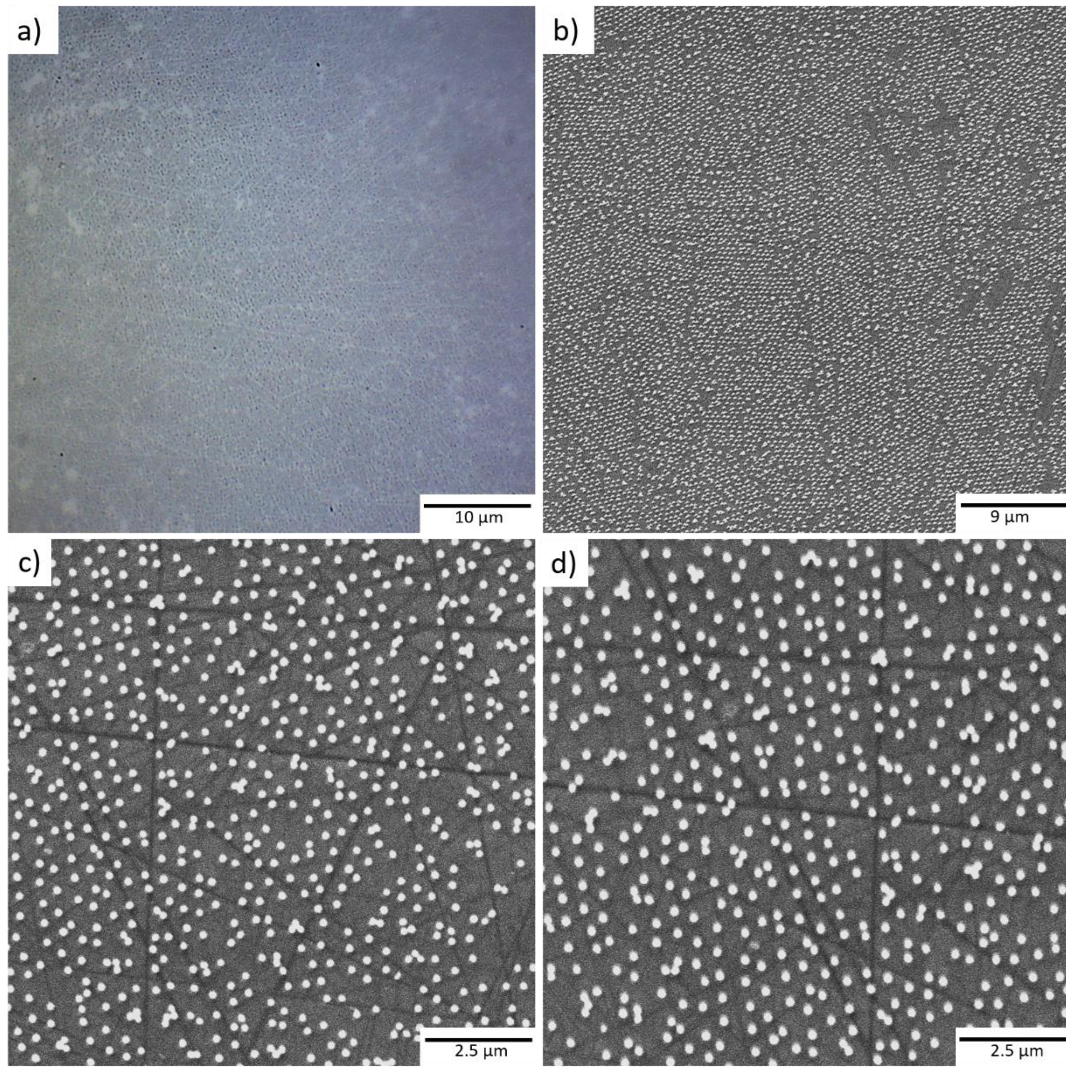

Figure 26. The (a) optical microscopy and (b,c,d) SEM images of Cr/Ni nanoisland based shadow mask on the 6H-SiC surface.

Table 12. Statistical data on the Cr/Ni nanoislands.

Cr/Ni Thickness (nm)	**Min. Diameter (nm)**	**Max. Diameter (nm)**	**Mean Diameter (nm)**	**Standard Deviation (nm)**
10/30	138	182	162	10

3.2.6. Step Six: Fabrication of 6H-SiC Nanopillars by Inductively Coupled Plasma Reactive Ion Etching Technique

The dry etching procedure for robust substrates such as SiC require aggressive etch techniques, which is possible with inductively-coupled plasma reactive ion etching (ICP-RIE) systems. ICP-RIE systems can generate very high density plasma by radio frequency (RF) powered magnetic field which results in higher etch rates than possible by conventional RIE systems. Additionally, the ICP-RIE systems operate at much lower pressures, which allows better directionality of the ion flux, thus promotes a more anisotropic etch profile.

A mixture of SF_6 and O_2 gasses are conventionally used to etch SiC substrates by ICP-RIE. SF_6 gas chemically etches the robust SiC substrate, where O_2 gas is thought to promote faster etching at the C rich areas (Plank et al. 2003) and to passivate the sidewalls of the structures by creating a thin oxide layer (Khan and Adesida 1999; Yih, Saxena, and Steckl 1997). In such highly directional system, most of the plasma ions reach the surface vertically. But a few of the non-vertical ions can etch the sidewalls, which leads to isotropic etching. Addition of O_2 gas in the mixture promotes the oxidation of the surface, and the forming silicon oxide has a lower etch rate than SiC, thus it helps protecting the sidewalls, which are bombarded with much fewer ions when compared to the horizontal components of the sample.

In the etch procedure, firstly, reactive fluorine ions are formed by an RF generator. The generated fluorine radicals and oxygen atoms chemically etch the SiC wafer by breaking the Si-C bonds by chemical reactions presented in Equations 3.1, 3.2 and 3.3 (Pan 1990).

$$SiC_{(s)} + xF_{(g)} + yO_{(g)} \rightarrow SF_{4(g)} + (CO, CO_2) \qquad 3.1$$

$$Si_{(s)} + 4F_{(g)} \rightarrow SiF_4 \qquad 3.2$$

$$C_{(s)} + xO_{(g)} \rightarrow CO, CO_2 \qquad 3.3$$

The resulting species are taken out of the chamber by the pumps attached to the system.

The etch behaviours of SiC by ICP-RIE is dependent on many process parameters, such as the gas species used, operating pressure and temperature, gas flowrates and the

RF power. Different fluorinated gasses have been applied to dry-etching of SiC substrates, including SF_6 (So, Lim, and Jackson 1999; Chabert 2001; Lazar et al. 2006), NF_3 (J. J. Wang et al. 1998) and CHF_3 (Jin et al. 2006). Among them, the most extensively studied etch gas is SF_6 owing to its high degree of F dissociation that allows relatively higher etch rates. The etch rate of SiC is found to increase with the increasing SF_6 gas flowrate, and saturate after a certain value. This trend can be attributed to many factors, such as insufficient dissociation of SF_6 gas due to limited RF power, and the recombination of the fluorine radicals before reaching the wafer surface.

The increasing RF power also increases the etch rate via enhancing the physical etching of the wafer by ion bombarding and promotes a higher directionality. But such aggressive etching results in surface roughness (J. J. Wang et al. 1998), thus in order to acquire smooth surfaces, RF power should be well-adjusted.

The pressure inside the chamber should also be well-evaluated to acquire optimum etch rates (Khan and Adesida 1999). Too low pressure may result in a decrease of the plasma radicals, thus limit the etch rate. High pressures also decreases the etch rate via decreasing the directionality of the ions and promoting recombination processes.

The ICP-RIE procedure for nanopillar fabrication was done in the Clean Room Facilities of Sabancı University Nanotechnology Research and Application Center (SUNUM) by readily optimized parameters for SiC etching procedures. Each wafer was placed inside Oxford PlasmaLab 100 ICP 300 ICP-RIE system separately (Figure 27). Firstly, in order to eliminate the effect of any organic contaminations, O_2 plasma treatment was applied on the samples for 60 sec at 60° C table temperature under 20 sccm of O_2 gas flow. Then the system was cooled down to the room temperature and the etch procedure was applied using a mixture of 6 sccm O_2 and 12 sccm SF_6 for one and two minutes for two different samples which are denoted as NPL and NPH, respectively. The ICP-RIE etch parameters are given in detail in Table 13.

Figure 27. Oxford PlasmaLab 100 ICP 300 ICP-RIE System in Sabancı University Nanotechnology Research and Application Center (SUNUM) used for dry anisotropic etching of 6H-SiC based samples retaining Cr/Ni nanoisland hard mask on their surfaces.

Table 13. The ICP-RIE parameters used to fabricate the nanopillar structures on the surface

ICP-RIE Step	**Gas**	**Flowrate (sccm)**	**RF Power (W)**	**Pressure (mT)**	**Time (sec)**
Cleaning	O_2	20	100	37.5	60
Etching	$SF_6 + O_2$	$SF_6 = 12$ $O_2 = 6$	250	3	60 (NPL) 120 (NPH)

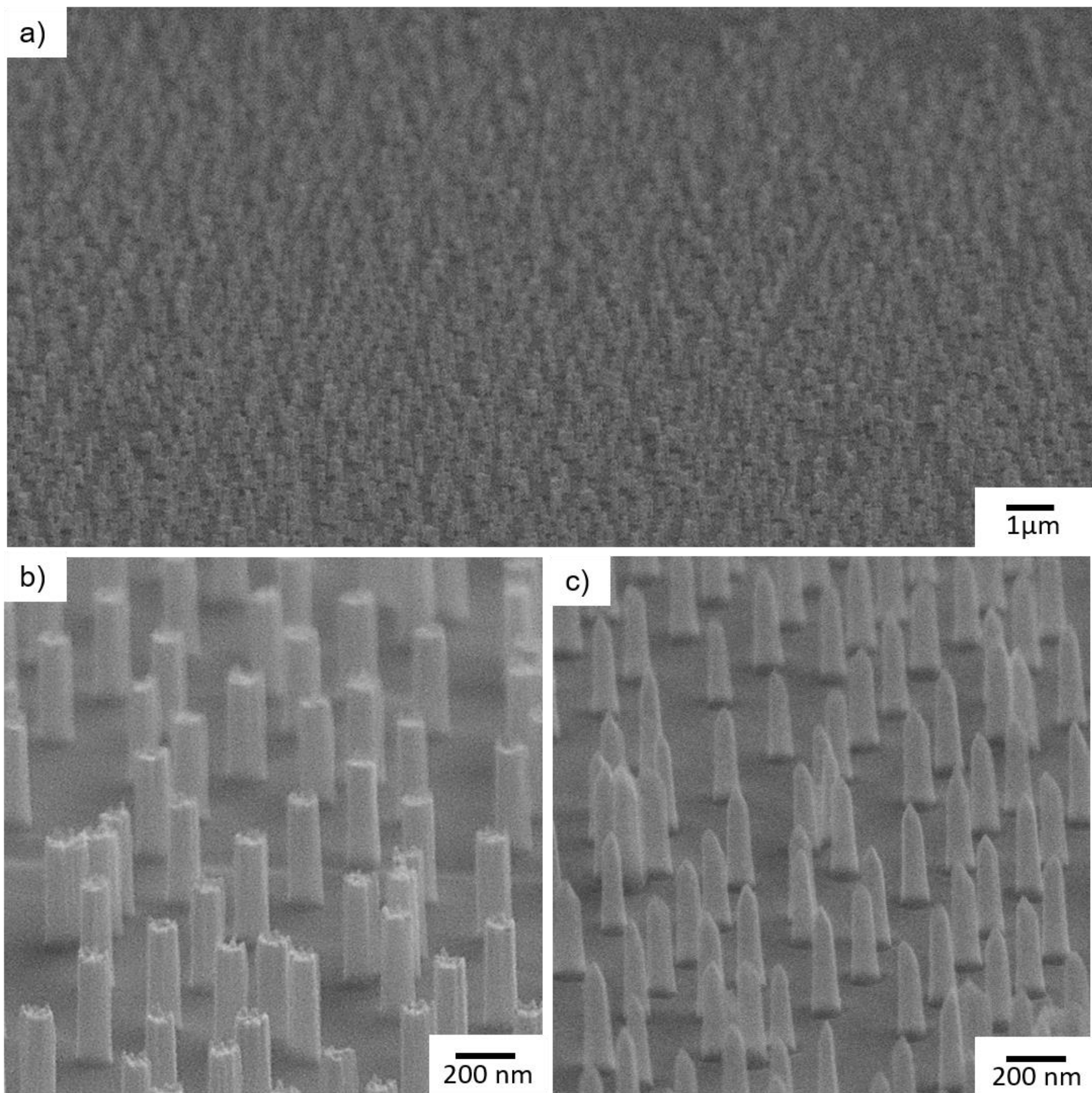

Figure 28. The SEM images taken with 70° angle from (a) sample etched for 60 sec. (NPL) low magnification (b) the sample surface of NPH at high magnification (c) sample etched for 120 sec. at high magnification.

Table 14. The statistical data obtained from the SEM images of nanopillars.

Sample	Average Height (nm)	Average Width (nm)	Aspect Ratio
NPL	376	111	3.4
NPH	417	85	4.9

The SEM measurements showed that that the nanopillars on the sample etched for 60 sec. have an aspect ratio of 3.4. And the tip apex of the nanopillars have blunt ends (Figure 28.*a, b*). On the other hand, the nanopillars on the sample etched for 120 sec. are found to have an aspect ratio of 4.9 and the tip apex of the nanopillars have sharp ends

with an estimated radius curvature of 18 ± 4 nm (Figure 28.*c*). These results suggest that the Cr/Ni shadow mask was completely etch during the second etch procedure, thus the resulting pillars have sharper tip apex with a lower aspect ratio than previously expected.

The 60 second-etched sample is named as NPL, to define low aspect ratio nanopillars and the 120 second-etched sample is named as NPH to define high aspect ratio nanopillars formed on the SiC surface. The statistical data extracted from the SEM measurements of both samples including the heights, widths and the aspect ratios are given in Table 14.

From the obtained values, it is calculated that the etch rate on the C-terminated face of 6H-SiC sample is 376 nm/min and the etch rate of the shadow mask is 35 nm/min. The shadow mask was completely etched after the first 7 sec. of the etch process, thus the resulting nanopillars had a height of 417 nm with sharp tip apex.

CHAPTER 4

FIELD EMISSION FROM SiC NANOPILLARS

4.1. The Experimental Set-up

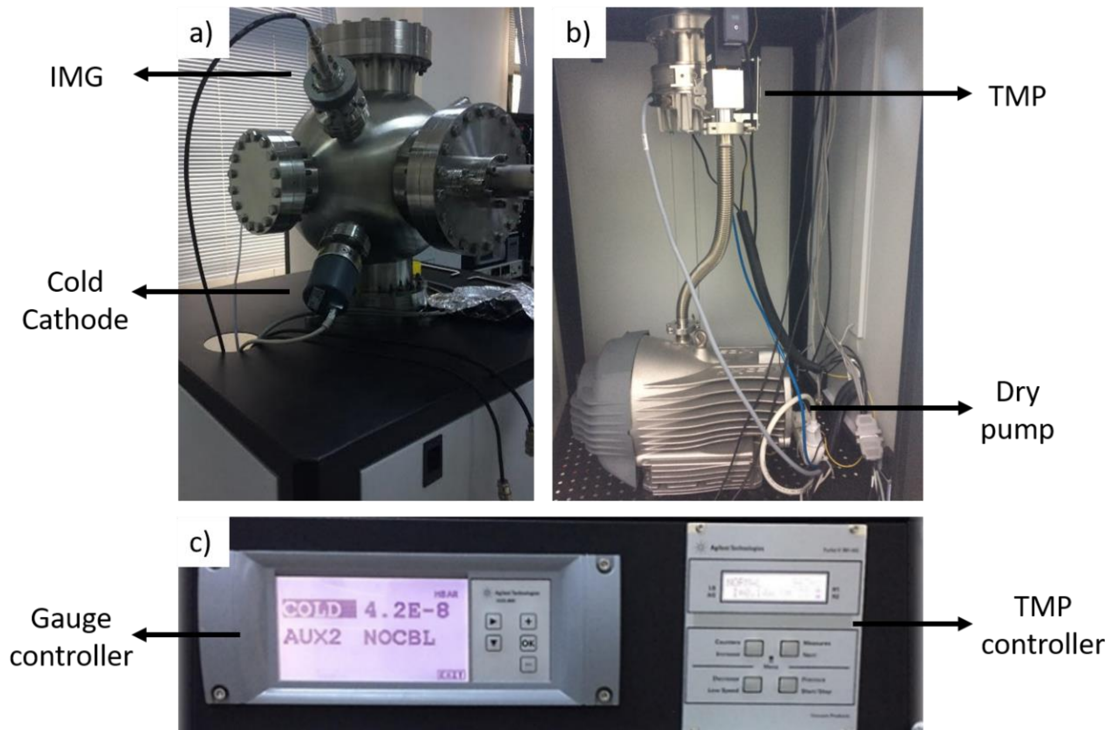

Figure 29. UHV system in Quantum Device Laboratory (a) The vacuum chamber (b) The pumps (c) The controller unit.

The field emission experiments in this study were conducted in an ultra-high vacuum (UHV) chamber with a base pressure in the range of 10^{-10} mbar (Figure 29.*a*). An Edwards nXDS6i dry pump is attached to the chamber to back Agilent Technologies Varian V-301 Navigator turbo molecular pump. The dry pump takes the pressure inside the chamber down to 10^{-2} mbar range by pumping the air away from the chamber, then the turbo molecular pump (TMP) is started to take the pressure inside the chamber down to 10^{-9} mbar (Figure 29.*b*).

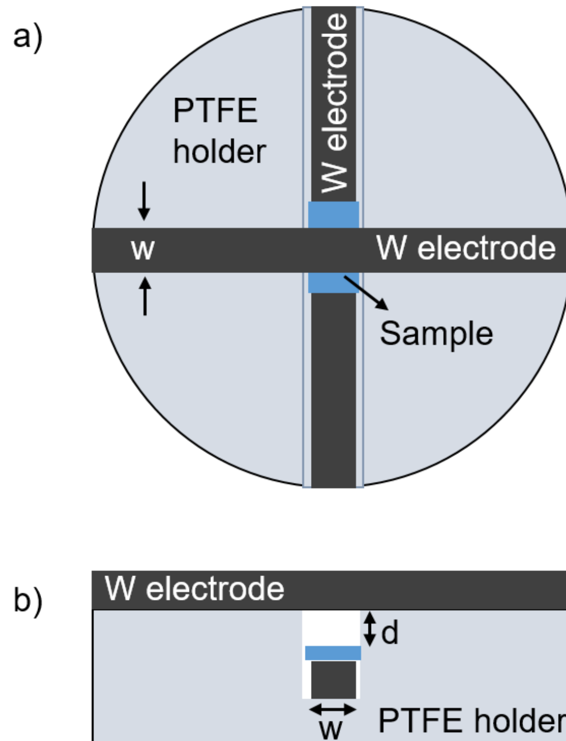

Figure 30. The schematic illustration of the sample stage for the electron field emission characterization of SiC nanopillar array (a) top view (b) side view.

Cold Cathode vacuum gauge attached to the chamber is used to detect the pressure inside the vacuum chamber in the range between 10^{3}-10^{-9} mbar. Inverted Magnetron Gauge (IMG) is used to read the pressure range between 10^{-3}-10^{-10} mbar (Figure 29.*c*)

For the field emission experiments, a home-made sample stage out of vacuum compatible polytetrafluoroethylene (PTFE) is designed as shown in Figure 30. The 6H-SiC substrate with vertically aligned nanopillars on its surface was bonded on a planar tungsten plate (width w = 3 mm) using a silver paste after being immersed to 6% HF solution for 3 min to remove the native oxide layer present on the wafer. As the anode electrode, another planar tungsten plate was placed at a distance of about d = 230 µm above the sample surface that covers approximately 9 mm^2 active emitting area at the middle of the sample. Both electrodes were placed on the PTFE sample holder in order to ensure the electrical isolation between the respective electrodes (Figure 30).

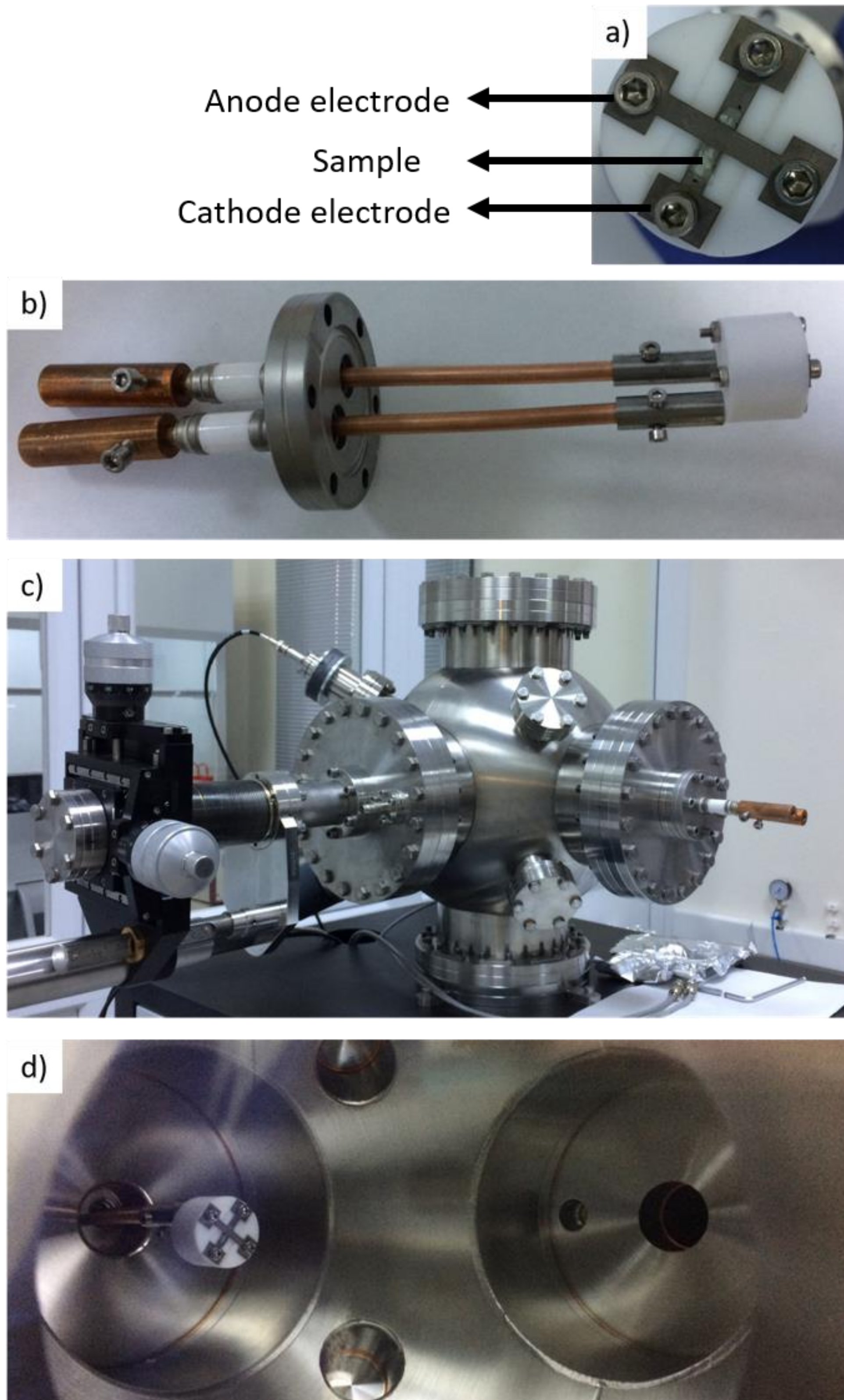

Figure 31. (a) The PTFE sample stage retaining the two electrodes (b) The feedthrough with the sample stage (c) The feedthrough mounted inside the UHV chamber (d) The view of the sample inside the UHV chamber from the viewport.

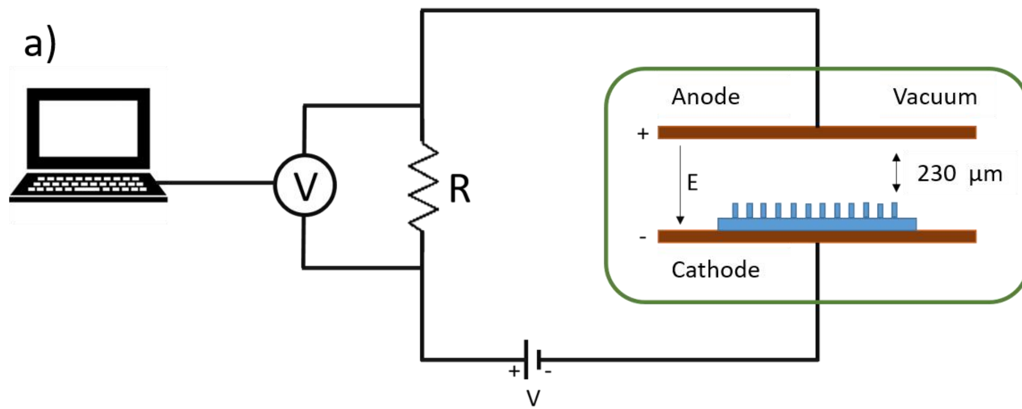

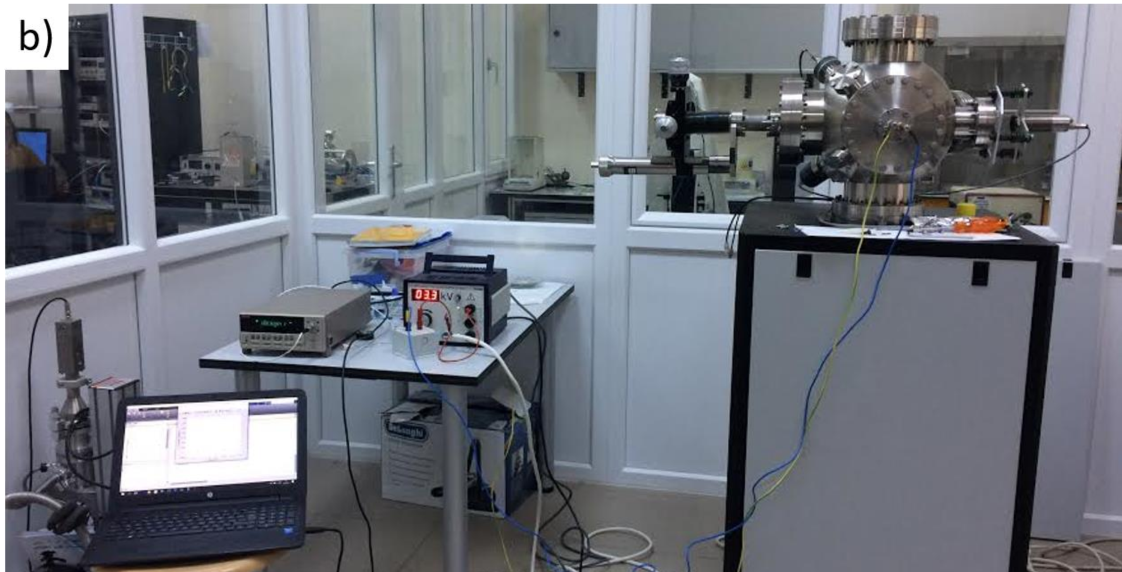

Figure 32. (a) The schematics and (b) the actual picture of the experimental set-up that was constructed for conducting the field emission experiments.

The sample stage retaining these two electrodes was then attached to a vacuum feedthrough that can withstand high voltages above 5 kV. In order to integrate the sample stage to the vacuum feedthrough, two cylindrical molybdenum apparatus was designed. The electrical contacts between the electrodes and the feedthrough was provided by stainless steel screws. The feedthrough was then inserted the UHV chamber through a DN 40 CF (2.75'') port (Figure 31).

After placing the electrical feedthrough with the sample inside the UHV chamber, the pumps were started and we waited overnight to achieve a pressure of 5 x 10^{-9} mbar inside the chamber. After abovementioned pressure is reached, the field emission characteristics of the SiC nanopillars were measured for an applied potential difference ranging between 0-4 kV. The applied voltage was gradually increased by 100 V per each

step. For the field emission experiments, we used PHYWE 13673-93 high voltage source that is manually controlled, and the acquired field emission currents were read through the voltage drop on a 50.68 kΩ load resistance by using KEITHLEY 2182A Nanovoltmeter. The schematics and the picture of the measurement set-up were given in Figure 32.

The nanovoltmeter was controlled by MATLAB 2016a, which is programmed to get 20 data for each applied voltage and save the mean values of the obtained measurement data to a log. Such data logging procedure provided us to eliminate the noise in the system and also the possible rippling present in the field emission currents.

4.2. Field Emission Measurements of SiC Nanopillars

The field emission current density (J) characteristics of both NPL and NPH samples as a function of applied electric field (E) were shown in Figure 33.

The turn-on and threshold electric fields, defined as the electric field required to obtain an electric current density of 1 μA/cm^2 and 10 μA/cm^2, respectively, are found to be 4.2 V/μm and 9.1 V/μm for the NPL samples. Owing to its sharp geometry and smaller radius of curvature at the tip apex of about 18 nm, the turn on electric field for NPH sample was found to be as low as 3.4 V/μm and the threshold electric field was measured as 7.2 V/μm. The measured total current for NPL is 6.3 μA and for NPH is 21.6 μA. Considering the active emitting area (9 mm^2) of the samples, the current densities are determined. At the maximum applied electric field of 17.4 V/μm, which is limited by our voltage-current measurement set-up, the field emission current densities were found as 70 μA/cm^2 and 240 μA/cm^2 for the NPL and NPH samples, respectively.

The emission current due to tunnelling of electrons under an applied electric field follows the Fowler-Nordheim (FN) equation given as:

$$J = \frac{A\beta^2 E^2}{\phi} \exp\left(-\frac{B\phi^{3/2}}{\beta E}\right) \tag{4.1}$$

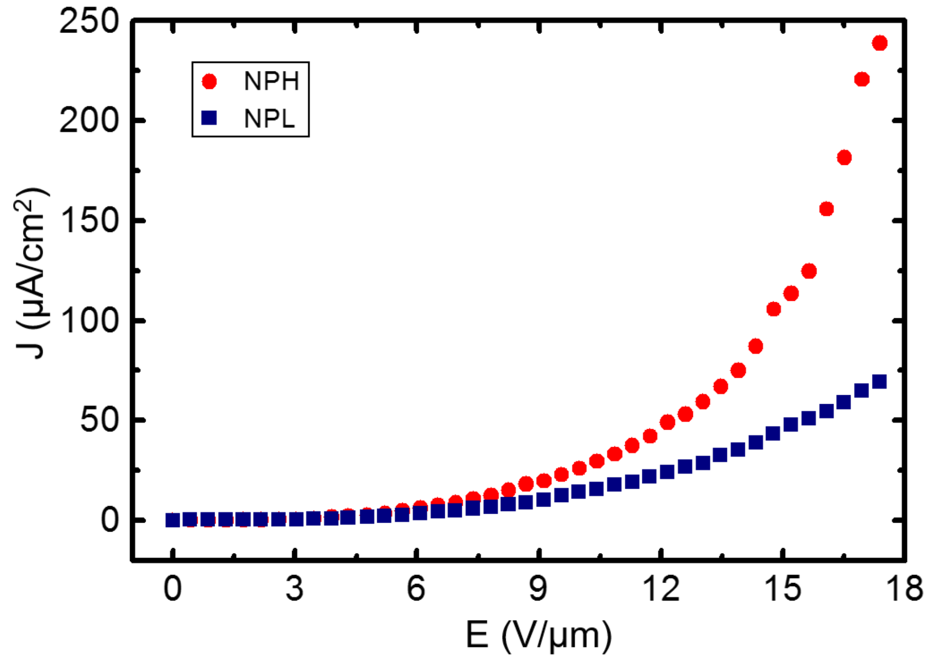

Figure 33. The change in the field emission current density with respect to the applied electric field for NPL and NPH samples.

where J is the current density, ϕ is the work function of the emitter material, E is the applied electric field, A and B are the FN constants (Mihalcea and Piot 2008) given as A = 1.546 x 10^{-6} $AV^{-2}eV$ and B = 6.83 x 10^{7} $eV^{-3/2}Vcm^{-1}$ and β is the field enhancement factor. For a metallic single emitter, β is in agreement with height to radius ratio of the emitter (Podenok et al. 2006; Forbes, Edgcombe, and Valdrè 2003). However, for the large area field emitter arrays, experimentally acquired values of the β factors are observed to have a two-fold hierarchy (Kang et al. 2012): (1) the local field enhancement that arise from the individual shape of the emitter structures (Bonard et al. 2001) and (2) the global electric field enhancement which is related to the spatial arrangement of the field emitters on the sample surface (X. Wang et al. 2007; Hwang et al. 2011). In the case of semiconductor based field emitters, β values calculated from the slopes of the FN plot is observed to deviate from the actual field enhancement of the structure due to field penetration effect, presence of shallow states arising from the doping of the semiconductor material (Y. J. Zhang, Li, and Chen 2008; Gubanov and Fong 1999; S. Chen et al. 2016) and the crystallinity of the sample (Hsieh et al. 2007). Combination of these effects may give rise to drastic variations on the experimentally obtained β values for large area semiconductor based field emitter arrays.

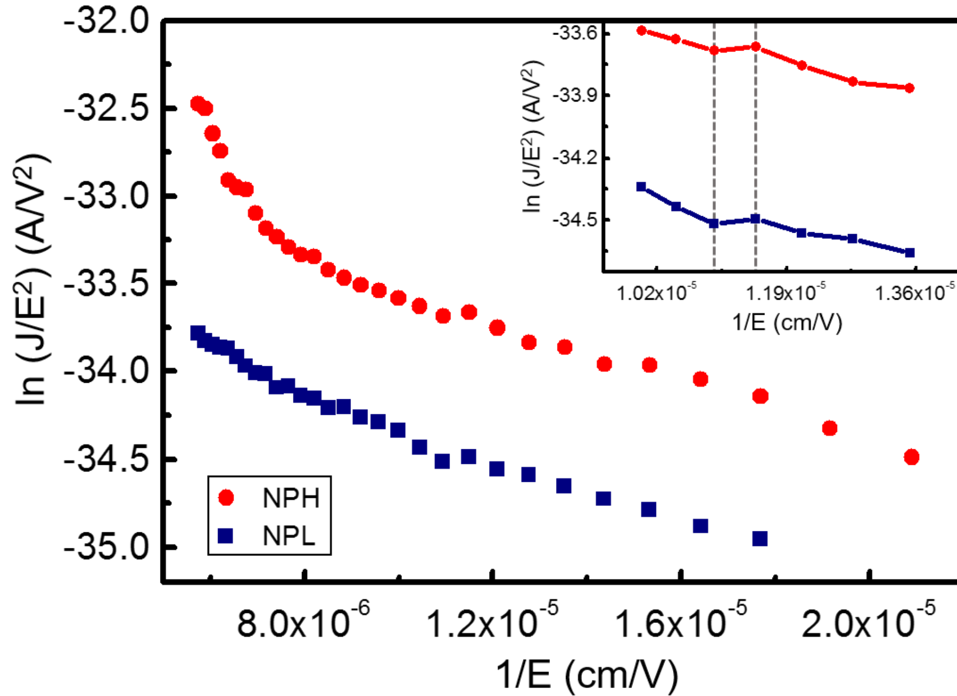

Figure 34. FN characteristics of the NPL and NPH samples. (Inset) Step like change observed between electric field values 8.7 V/µm and 9.1 V/µm.

The Equation 4.1 can also be written to fit the form $y = mx + n$:

$$\ln(J/E^2) = \ln\left(\frac{A\beta^2}{\phi}\right) - \frac{B\phi^{3/2}}{\beta E} \quad (4.2)$$

In the case of electron field emission, the slope (S) of $\ln(J/E^2)$ versus 1/E graph should give a straight line according to the Equation 4.2. In order to verify that the experimentally obtained J-E characteristics (Figure 33) are related to the electron field emission phenomenon from the produced SiC nanopillars, the graph, also called FN plot, was shown in Figure 34.

The linear behaviour of the FN plot for both samples agrees well with the electron field emission phenomenon at the tip apex of the SiC nanopillar emitters. But the FN plot of NPH shows a deviation from linearity at high electric fields above 15 V/µm. This phenomenon is attributed to the joule heating of the sample and thus to the generation of

hot electrons (Hallam et al. 2014). This effect was also observed as a slight increase in the pressure level of our vacuum system.

Table 15. The slopes and the corresponding field enhancement factors for NPL and NPH samples.

	NPL	**NPH**
Aspect Ratio	3.4	4.9
S^{LE}	-75100	-81076
β^{LE}	7828	7251
S^{HE}	-131636	-104253
β^{HE}	4466	5639

According to Equation 4.2, the slope of the FN plot can be written as:

$$S = -\frac{B\phi^{\frac{3}{2}}}{\beta} \tag{4.3}$$

The field enhancement factors can be calculated from the experimentally obtained slopes by using Equation 4.3. In our case, two distinct slopes were observed with a step-like change at the electric field values between 8.7 V/µm and 9.1 V/µm for both samples (inset of Figure 34). The slopes for both low electric field (LE) and high electric field (HE) values were determined by fitting our measurements. It is important to note that the fitting procedure for the HE region for NPH sample was done by using the linear part of the slope where the electron field emission phenomenon is present. The obtained slopes and the calculated β values are given in Table 15. The work function of the 6H-SiC was taken as ϕ = 4.2 eV for all the calculations (Kang et al. 2012).

There are two peculiarities that should be addressed in the experimentally obtained β factors.

Firstly, for low LE values, it is found that the field enhancement factor obtained for NPL are larger than the field enhancement factor obtained for NPH ($\beta_{NPL}^{LE} > \beta_{NPH}^{LE}$). This result is contrary to the fact that high aspect ratio structures lead to higher field enhancement. We think that the emitted electrons at low electric fields are more likely to be arising from the surface states where the work function is inherently lower. Thus, using ϕ = 4.2 eV for the calculation at this electric field range leads to an over-prediction of the

experimentally obtained field enhancement factors and results in a false perception that the field enhancement is unrelated to the aspect ratios of the acquired structures. For HE region, one can see that $\beta_{NPL}^{HE} < \beta_{NPH}^{HE}$ as initially expected from the aspect ratios of the nanopillars on the sample surface. At the HE region, the triangular barrier narrows down enough to let the electrons tunnel from the bulk and for this regime, using $\phi = 4.2$ eV for the calculations do not provide over-predicted results. In the vicinity of this phenomenon, we assumed that the step-like change observed in the FN plot arises from a step-like change in the work function.

Secondly, as expressed in Equation 2.14, the field enhancement factors are related to the height to radius ratio of the individual emitters; yet in our case, the experimentally obtained β values are much higher. The approximation $\left(\beta \approx 2 + \frac{h}{r}\right)$ assumes a metallic emitter with an atomically flat surface, thus disregards the field penetration and the initial surface roughness (Forbes, Edgcombe, and Valdrè 2003) on the emitter surfaces. It is thought that both the field penetration effect, and the initial roughness present on the nanopillars for NPL sample, and the sharp tip apex in the range of 18 ± 4 nm for NPH sample have acted as effective emission sites and further enhanced the electrical field at the nanopillar tips.

As for the last step, the stabilities of the field emission currents were measured as a function of time for 3 hours of period under an applied electric field of 8.7 V/µm for both samples (Figure 35).

The measurements have revealed a stable electron emission current densities of 8.8 $\mu A/cm^2$ for NPL and 18.5 $\mu A/cm^2$ for NPH with congruent fluctuations. There were not any abrupt changes or cut-offs in the acquired field emission currents. The percentage of the fluctuations were calculated from the minimum and maximum currents recorded during the measurements revealed a current stability in the range of ±8.1% and ±8.3% for NPL and NPH samples, respectively. The statistical data obtained from the stability measurements were given in Table 16.

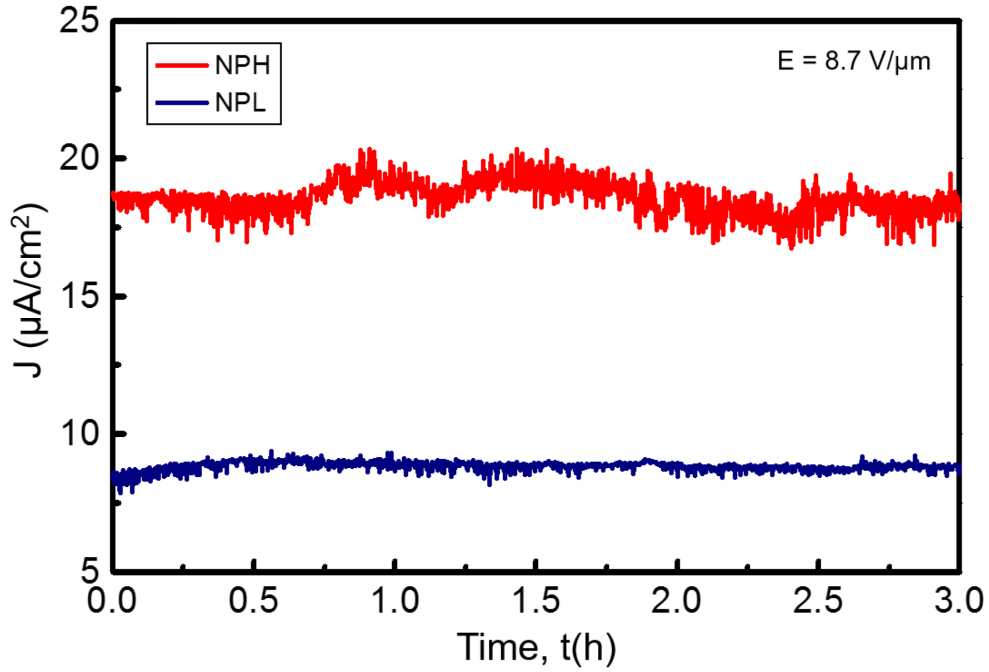

Figure 35. Time dependent measurements of the field emission current stability for NPL and for NPH samples acquired under an applied electric field of 8.7 V/µm.

Table 16. The statistical data obtained from the stability measurements of the NPL and NPH samples for a duration of 3 hours.

Sample	Min. current density (µA/cm²)	Max. current density (µA/cm²)	Mean current density (µA/cm²)	Standard deviation (µA/cm²)
NPL	7.8	9.4	8.8	0.2
NPH	16.7	20.3	18.5	0.6

The main reason for these fluctuations are attributed to the temporal changes in the work function of the emitter surface due to adsorption and desorption of the residual gasses under high applied electric fields (Valiev 2013). In the literature, the field emission current stabilities of nanoscale emitters are usually in the range of 5 - 20% (Hallam et al. 2014; Choi, Chung, Kang, et al. 1999; Y. B. Li et al. 2002). Thus the field emission current stabilities of our SiC nanopillar samples were found to be in the acceptable range.

4.3. Results and Discussion

In this chapter, we have investigated the field emission characteristics of the SiC based nanopillars with two different aspect ratios and geometries. The experimentally obtained field emission currents for both samples were compared with each other. The FN plots were drawn according to the collected data and the field enhancement factors were calculated. Finally, the stability of the field emission currents was investigated as a function of time for an interval of 3 hours.

The field emission experiments were carried out inside a UHV chamber, under a pressure level of 5×10^{-9} mbar. The electric field was generated by an applied voltage between the cathode electrode retaining the SiC nanopillar structures, and the extractor anode electrode placed at a constant spacing of 230 μm above the cathode. The voltage was applied by 100 V steps from 0 V up to 4 kV, and the corresponding field emission currents were measured indirectly through the voltage drop on a load resistance by a nanovoltmeter. The change in the field emission current densities with respect to the change in the applied electric field was then plotted for both samples. We found that the sample with high aspect ratio nanopillars with sharp tip apex yield larger field emission currents at each applied electrical field.

In order to verify the presence of field emission phenomenon and to obtain the field enhancement factors of the respective nanopillar structures, FN plot was drawn from the experimentally obtained data. The linearity of the FN plots agrees well with the electron field emission phenomenon at the nanopillar tips. A deviation from linear behaviour after 15 V/μm was observed for the sample with high aspect ratio nanopillars, accompanied by a slight increase in the pressure level of the vacuum chamber. This incident was attributed to the joule heating of the sample and the generation of hot electrons at high applied electric fields.

Two distinct slopes were observed in the FN plot of both samples for low and high applied electric field regions. The field enhancement factors of both samples for each slope were calculated. The slopes acquired for low electric field yielded over-predicted field enhancement factors when the calculations are made considering the work function value of $\phi = 4.2$ eV for 6H-SiC crystal. This phenomenon was attributed to the tunnelling of the electrons from the surface states at low electric fields, where the work function is relatively lower. The field enhancement factors for high electric field region yielded much

larger values than initially expected from the aspect ratios of the nanopillars on the surface. We think that the large enhancement factors are a result of initial surface roughness on the nanopillars (for NPL) and the sharp tip apex of about 18 nm (for NPH).

In order to determine the stability of the acquired field emission currents, a time dependent measurement was conducted for a duration of 3 hours. Both samples were found to produce stable currents with congruent fluctuations at a value around 8%.

CHAPTER 5

CONCLUSIONS

The research in this thesis was focused on the fabrication of SiC based nanopillar electron field emitters and the examination of their electron field emission characteristics. Within the scope of this thesis, we have proposed an easy and cost-effective way to produce the conventional Ni based shadow mask for dry etching of the robust SiC crystal. C-terminated faces of 6H-SiC wafers with the shadow mask acquired by utilizing the proposed method were etched by ICP-RIE for different etching durations. The resulting nanopillar structures with different aspect ratios and geometries were then investigated to determine their electron field emission capabilities.

The fabrication of the required nanoscale etch mask was done by the nanosphere lithography method. Although the PS nanospheres are not suitable for aggressive dry etching methods like ICP-RIE that are required to etch robust SiC, the monolayer structure the spheres form on the surface can be used as a template to produce the desired shadow mask. Firstly, the monolayer self-assembly of the nominally 453 nm PS nanospheres on the C-terminated face of 6H-SiC were investigated for spin coating technique. After forming a large area self-assembly pattern on the SiC surface, the diameter of the PS nanospheres were reduced by using O_2 plasma treatment. A 40 nm thick Au layer was deposited on the surface as a sacrificial layer, due to its poor adhesion to the native oxide layer on the SiC surface. Following the Au deposition stage, the PS nanospheres were removed from the SiC surface with ultrasonic bath in IPA. This process resulted in an inverse pattern on the Au layer with holes where the nanospheres left the surface. This inverse pattern was used as a template and thermally evaporated Cr/Ni (10/ 30 nm) layer was deposited on this template. The sacrificial layer was removed by a conventional sticky tape and the desired Cr/Ni nanoislands were produced on the SiC surface to be used as hard etch masks.

Two 6H-SiC wafers retaining these nanoscale shadow masks were then etched by ICP-RIE with SF_6 and O_2 gas mixture for 1 and 2 min durations. The resulting nanopillars obtained for 1 min etch duration had an aspect ratio of 3.4 and a blunt tip apex retaining the initial roughness of the wafer (NPL), whereas for 2 min. etch time the nanopillars had an aspect ratio of 4.9 and a sharp tip apex with a radius of curvature of about 18 nm

(NPH). Possible remaining traces of the Cr/Ni mask and the native oxide layer present on the nanopillars were chemically removed.

The samples were then placed into a UHV chamber and their electron field emission characteristics were investigated by applying electric field between two tungsten electrodes in a voltage range between 0 and 4 kV. The turn-on and threshold electric fields for NPL were determined to be 4.2 V/µm and 9.1 V/µm, respectively. These values were found to be lowered down to 3.4 V/µm and 7.2 V/µm for the NPH sample. The FN plots for both samples revealed a linear relationship that is consistent with the electron field emission phenomenon occurred at the tip apex of both samples. The slopes of the FN plot revealed large field enhancement values at the tip of the emitters. It is thought that along with the sufficient spatial arrangement of the field emitters, the initial surface roughness present on the top of the nanopillars for the NPL sample, and the sharp tip apex of the NPH sample have led to further enhancement at the emitter tip apexes. In addition, the stabilities of the field emission currents of both samples were also investigated under 8.7 V/µm applied electric field for a duration of 3 hours. NPL sample yielded a mean current density of about 8.8 $\mu A/cm^2$ with congruent fluctuations in the range of ±8.1%, whereas the NPH samples yielded a mean current density of 18.5 $\mu A/cm^2$ with congruent fluctuations in the range of ±8.3%. These obtained values are in good agreement with the reported values for nanoscale field emitter structures. The results obtained in this study were also published in JVST-B (Yesilpinar and Celebi 2017) .

Energy efficient electron sources with long life-times are crucial for many technological applications of the decade. The field emission electron sources have a vast number of desirable properties owing to their high efficiency, fast operating speed and longer life expectancies. Thus, a significant number of research investigating the electron field emission characteristics of various materials in numerous forms have been conducted worldwide to acquire field emission cold cathodes with stable and high current densities. Owing to its exceptional material properties, SiC stands out as a remarkable candidate to be used as a cathode element of electron field emitters that are meant to work in harsh environments, such as spacecraft neutralizers. The dry etching mechanisms of SiC wafers have been extensively investigated over the past years. We believe that the development of fast, easy and cost effective methods for large-area top-down fabrication of SiC based nanoscale and high aspect ratio structures will pioneer the utilization of this exceptional material as robust field emitter structures for high-end applications.

REFERENCES

Abdi, Yaser, Azadeh Malekan, and Sara Darbari. 2013. "High Sensitivity Field Emission Based Sensors Using Carbon Nanotubes on Silicon Tip for High Frequency Vibration Sensing." *Solid-State Electronics* 82: 6–10. doi:10.1016/j.sse.2013.01.008.

Alam, M M R Howlader, and M J Deen. 2014. "The Effects of Oxygen Plasma and Humidity on Surface Roughness, Water Contact Angle and Hardness of Silicon, Silicon Dioxide and Glass." *Journal of Micromechanics and Microengineering* 24 (3): 35010. doi:10.1088/0960-1317/24/3/035010.

Allen, F. G. 1957. "Emissivity at 0.65 Micron of Silicon and Germanium at High Temperatures [3]." *Journal of Applied Physics* 28 (12): 1510–11. doi:10.1063/1.1722688.

Aplin, K. L., B. J. Kent, W. Song, and C. Castelli. 2009. "Field Emission Performance of Multiwalled Carbon Nanotubes for a Low-Power Spacecraft Neutraliser." *Acta Astronautica* 64 (9–10): 875–81. doi:10.1016/j.actaastro.2008.10.012.

Aplin, K L, C M Collingwood, and B J Kent. 2004. "Reliability Tests of Gated Silicon Field Emitters for Use in Space." *Journal of Physics D: Applied Physics* 37 (14): 2009. doi: 10.1088/0022-3727/37/14/018.

Attolini, Giovanni, Francesca Rossi, Filippo Fabbri, Matteo Bosi, Giancarlo Salviati, and Bernard Enrico Watts. 2010. "Cubic SiC Nanowires : Growth , Characterization and Applications." *Nanowires*, no. March: 1–23. ISBN 978-953-7619-79-4, pp. 414

Babenko, Yu, T. Dideykin, and E. D. Eidelman. 2009. "Graphene Ladder: A Model of Field Emission Center on the Surface of Loose Nanocarbon Materials." *Physics of the Solid State* 51 (2): 435–39. doi:10.1134/S1063783409020371.

Bechelany, Mikhael, Arnaud Brioude, Pierre Stadelmann, Gabriel Ferro, David Cornu, and Philippe Miele. 2007. "Very Long SiC-Based Coaxial Nanocables with Tunable Chemical Composition." *Advanced Functional Materials* 17 (16): 3251–57. doi:10.1002/adfm.200700110.

Bodas, Dhananjay, and Chantal Khan-Malek. 2007. “Hydrophilization and Hydrophobic Recovery of PDMS by Oxygen Plasma and Chemical Treatment-An SEM Investigation.” *Sensors and Actuators, B: Chemical* 123 (1): 368–73. doi:10.1016/j.snb.2006.08.037.

Bonard, J.-M., Nicolas Weiss, Hannes Kind, Thomas Stöckli, Lμszló Forró, Klaus Kern, and A. Châtelain. 2001. “Tuning the Field Emission Properties of Patterned Carbon Nanotube Films.” *Advanced Materials* 13 (3): 184–88. doi:10.1002/1521-4095(200102)13:3<184::AID-ADMA184>3.0.CO;2-I.

Chabert, P. 2001. “Deep Etching of Silicon Carbide for Micromachining Applications: Etch Rates and Etch Mechanisms.” *Journal of Vacuum Science & Technology B: Microelectronics and Nanometer Structures* 19 (4): 1339. doi:10.1116/1.1387459.

Chang, Hsuan Chen;, Chien-Chang; Li, Shuo-Fang; Jen, Chun-Chieh; Lu, Ian Yi-yu; Bu, Po-Wen; Chiu, and Kuei-Yi; Lee. 2013. “All-Carbon Field Emission Device by Direct Synthesis of Graphene and Carbon Nanotube.” *Diamond and Related Materials* 31. Elsevier B.V.: 42–46. doi:10.1016/j.diamond.2012.10.011.

Chang, Yuan Ming, Mao Chen Liu, Pin Hsu Kao, Chih Ming Lin, Hsin Yi Lee, and Jenh Yih Juang. 2012. “Field Emission in Vertically Aligned ZnO/Si-Nanopillars with Ultra Low Turn-on Field.” *ACS Applied Materials and Interfaces* 4 (3): 1411–16. doi:10.1021/am201667m.

Chen, Jian, Peitao Dong, Di Di, Chaoguang Wang, Haoxu Wang, Junfeng Wang, and Xuezhong Wu. 2013. “Controllable Fabrication of 2D Colloidal-Crystal Films with Polystyrene Nanospheres of Various Diameters by Spin-Coating.” *Applied Surface Science* 270: 6–15. doi:10.1016/j.apsusc.2012.11.165.

Chen, S. Y., Miao H. Y., Lue J.T., and Ouyang M.S. 2003. “Fabrication and Field Emission Property Studies of Multiwall Carbon Nanotubes.” *Journal of Physics D: Applied Physics* 37: 273–79. doi:10.1088/0022-3727/37/2/017.

Chen, Shanliang, Minghui Shang, Zuobao Yang, Jinju Zheng, Lin Wang, Qiao Liu, Fengmei Gao, and Weiyou Yang. 2016. “Current Emission from P-Doped SiC Nanowires with Ultralow Turn-on Fields.” *J. Mater. Chem. C* 4 (31). Royal Society of Chemistry: 7391–96. doi:10.1039/C6TC01823H.

Cheung, C. L., R. J. Nikolic, C. E. Reinhardt, and T. F. Wang. 2006. "Fabrication of Nanopillars by Nanosphere Lithography." *Nanotechnology* 17: 1339–43. doi:10.1088/0957-4484/17/5/028.

Choi, W. B., D. S. Chung, J. H. Kang, H. Y. Kim, Y. W. Jin, I. T. Han, Y. H. Lee, et al. 1999. "Fully Sealed, High-Brightness Carbon-Nanotube Field-Emission Display." *Applied Physics Letters* 75 (20): 3129–31. doi:10.1063/1.125253.

Choi, W B, D S Chung, S H Park, and J M Kim. 1999. "L2.1: Late-News Paper: A 4.5-In. Fully Sealed Carbon Nanotube-Based Field-Emission Flat-Panel Display." *SID Symposium Digest of Technical Papers* 30 (1). Blackwell Publishing Ltd: 1134–37. doi:10.1889/1.1833969.

Colson, Pierre, Catherine Henrist, and Rudi Cloots. 2013. "Nanosphere Lithography: A Powerful Method for the Controlled Manufacturing of Nanomaterials." *Journal of Nanomaterials* 2013. doi:10.1155/2013/948510.

D'Asaro, L. A. 1958. "Field Emission from Silicon." *Journal of Applied Physics* 29 (1): 33–34. doi:10.1063/1.1722938.

Dowling, Karen and Shankar, Ashwin 2014. "Bulk Silicon Carbide Etching in PT-MTL" Web: https://snf.stanford.edu/SNF/processes/ee412/srping-14/final-reports/ee412-final-report-bulk-sic-etching-in-pt-mtl

Evans, Laura J, and Glenn M Beheim. 2006. "Deep Reactive Ion Etching (DRIE) of High Aspect Ratio SiC Microstructures Using a Time-Multiplexed Etch-Passivate Process." *Materials Science Forum* 527–529: 1115–18. doi:10.4028/www.scientific.net/MSF.527-529.1115.

Forbes, Richard G. 2004. "Use of Energy-Space Diagrams in Free-Electron Models of Field Electron Emission." *Surface and Interface Analysis* 36 (56): 395–401. doi:10.1002/sia.1900.

Forbes, Richard G, C.J Edgcombe, and U Valdrè. 2003. "Some Comments on Models for Field Enhancement." *Ultramicroscopy* 95: 57–65. doi:10.1016/S0304-3991(02)00297-8.

Fredriksson, Hans, Yury Alaverdyan, Alexandre Dmitriev, Christoph Langhammer, Duncan S. Sutherland, Michael Zäch, and Bengt Kasemo. 2007. “Hole-Mask Colloidal Lithography.” *Advanced Materials* 19 (23): 4297–4302. doi:10.1002/adma.200700680.

Ganguly, A. K., P. M. Phillips, and H. F. Gray. 1990. “Linear Theory of a Field-Emitter-Array Distributed Amplifier.” *Journal of Applied Physics* 67 (11): 7098. doi:10.1063/1.345060.

Gomer, Robert. 1994. “Field Emission, Field Ionization, and Field Desorption.” *Surface Science* 299–300 (C): 129–52. doi:10.1016/0039-6028(94)90651-3.

Gray, Henry F. 1994. "Regulatable Field Emitter Device And Method Of Production Thereof". *US*.

Gubanov, V. A., and C. Y. Fong. 1999. “Doping in Cubic Silicon–carbide.” *Applied Physics Letters* 75 (1): 88. doi:10.1063/1.124285.

Hallam, Toby, Matthew T. Cole, William I. Milne, and Georg S. Duesberg. 2014. “Field Emission Characteristics of Contact Printed Graphene Fins.” *Small* 10: 95–99. doi:10.1002/smll.201300552.

Hao, Ya Juan, Guo Qiang Jin, Xiao Dong Han, and Xiang Yun Guo. 2006. “Synthesis and Characterization of Bamboo-like SiC Nanofibers.” *Materials Letters* 60 (11): 1334–37. doi:10.1016/j.matlet.2005.10.115.

Harris, Gary L. 1995. "Properties of Silicon Carbide." ISBN 0 85296 870 1

Haynes, Christy L, Adam D Mcfarland, Matthew T Smith, John C Hulteen, and Richard P Van Duyne. 2002. “Angle-Resolved Nanosphere Lithography : Manipulation of Nanoparticle Size , Shape , and Interparticle Spacing Angle-Resolved Nanosphere Lithography : Manipulation of Nanoparticle Size , Shape , and Interparticle Spacing.” *Society*, 1898–1902. doi:10.1021/jp013570.

Heer, Walt A de, A Châtelain, and D Ugarte. 1995. “A Carbon Nanotube Field-Emission Electron Source.” *Science* 270 (5239): 1179–80. doi:10.1126/science.270.5239.1179.

Hsieh, Ho-Yen, Sheng-Huang Huang, Kao-Fen Liao, Sheng-Kai Su, Chih-Huang Lai, and Lih-Juann Chen. 2007. “High-Density Ordered Triangular Si Nanopillars with Sharp Tips and Varied Slopes: One-Step Fabrication and Excellent Field Emission Properties.” *Nanotechnology* 18 (50): 505305. doi:10.1088/0957-4484/18/50/505305.

Huczko, Andrzej, Michał Bystrzejewski, Hubert Lange, Agnieszka Fabianowska, Stanisław Cudziło, Andrzej Panas, and Mateusz Szala. 2005. “Combustion {Synthesis} as a {Novel} {Method} for {Production} of 1-{D} {SiC} {Nanostructures}.” *The Journal of Physical Chemistry B* 109 (34): 16244–51. doi:10.1021/jp050837m.

Hulteen, John C. 1995. “Nanosphere Lithography: A Materials General Fabrication Process for Periodic Particle Array Surfaces.” *Journal of Vacuum Science & Technology A: Vacuum, Surfaces, and Films* 13 (October 1994): 1553. doi:10.1116/1.579726.

Hwang, Jin Ok, Duck Hyun Lee, Ju Young Kim, Tae Hee Han, Bong Hoon Kim, Moonkyu Park, Kwangsoo No, and Sang Ouk Kim. 2011. “Vertical ZnO Nanowires/graphene Hybrids for Transparent and Flexible Field Emission.” *Journal of Materials Chemistry* 21 (10): 3432. doi:10.1039/c0jm01495h.

Jiang, P., J. F. Bertone, K. S. Hwang, and V. L. Colvin. 1999. “Single-Crystal Colloidal Multilayers of Controlled Thickness.” *Chemistry of Materials* 11 (8): 2132–40. doi:10.1021/cm990080.

Jin, Ning, Gong Quancheng, Sun Guosheng, and Liu Zhongli. 2006. “The ICP Etching Technology of 3C-SiC Films.” *Journal of Physics: Conference Series* 34: 511–15. doi:10.1088/1742-6596/34/1/084.

Kang, M. G., H. Lezec, R. L. Kallaher, and F. Sharifi. 2012. “Field Emission from Nanoporous Silicon Carbide.” *Proceedings of the IEEE Conference on Nanotechnology* 65201: 2–7. doi:10.1109/NANO.2012.6321952.

Khan, F. a., and I. Adesida. 1999. “High Rate Etching of SiC Using Inductively Coupled Plasma Reactive Ion Etching in SF[sub 6]-Based Gas Mixtures.” *Applied Physics Letters* 75 (15): 2268. doi:10.1063/1.124986.

Kim, Se Jung, Seol Ah Park, Young-Cho Kim, and Byeong-Kwon Ju. 2017. "Enhanced Field Emission Properties from Carbon Nanotube Emitters on the Nanopatterned Substrate." *Journal of Vacuum Science & Technology B, Nanotechnology and Microelectronics: Materials, Processing, Measurement, and Phenomena* 35 (1): 11802. doi:10.1116/1.4972119.

Kosiorek, A., W. Kandulski, P. Chudzinski, K. Kempa, and M. Giersig. 2004. "Shadow Nanosphere Lithography: Simulation and Experiment." *Nano Letters* 4 (7): 1359–63. doi:10.1021/nl049361t.

Kusdemir, E. 2015. *DEVELOPING EPITAXIAL GRAPHENE ELECTRODES FOR SILICON CARBIDE BASED OPTOELECTRONIC DEVICES*.

Kusdemir, Erdi, Dilce Özkendir, Volkan Fırat, and Cem Çelebi. 2015. "Epitaxial Graphene Contact Electrode for Silicon Carbide Based Ultraviolet Photodetector." *Journal of Physics D: Applied Physics* 48 (9). IOP Publishing: 95104. doi:10.1088/0022-3727/48/9/095104.

Lazar, M., H. Vang, P. Brosselard, C. Raynaud, P. Cremillieu, J. L. Leclercq, A. Descamps, S. Scharnholz, and D. Planson. 2006. "Deep SiC Etching with RIE." *Superlattices and Microstructures* 40 (4–6 SPEC. ISS.): 388–92. doi:10.1016/j.spmi.2006.06.015.

Lee, H. C., and R. S. Huang. 1992. "A Study on Field-Emission Array Pressure Sensors." *Sensors and Actuators* A34: 137–54.

Li, Wei, Jiang Zhou, Xian-Gao Zhang, Jun Xu, Ling Xu, Weiming Zhao, Ping Sun, Fengqi Song, Jianguo Wan, and Kunji Chen. 2008. "Field Emission from a Periodic Amorphous Silicon Pillar Array Fabricated by Modified Nanosphere Lithography." *Nanotechnology* 19: 135308. doi:10.1088/0957-4484/19/13/135308.

Li, Y. B., Y. Bando, D. Golberg, and K. Kurashima. 2002. "Field Emission from MoO3 Nanobelts." *Applied Physics Letters* 81 (26): 5048–50. doi:10.1063/1.1532104.

Liu, Jing, Chaoyang Chen, Guangsong Yang, Yushan Chen, and Cheng-Fu Yang. 2017. "Effect of the Fabrication Parameters of the Nanosphere Lithography Method on the Properties of the Deposited Au-Ag Nanoparticle Arrays." *Materials* 10 (4): 381. doi:10.3390/ma10040381.

Liu, Lei, Yingli Zhang, Wenlong Wang, Changzhi Gu, Xuedong Bai, and Enge Wang. 2011. "Nanosphere Lithography for the Fabrication of Ultranarrow Graphene Nanoribbons and on-Chip Bandgap Tuning of Graphene." *Advanced Materials* 23: 1246–51. doi:10.1002/adma.201003847.

M. Holgado, F. García-Santamaría, A. Blanco, M. Ibisate, A. Cintas, H. Míguez, C. J. Serna, et al. 1999. "Electrophoretic Deposition To Control Artificial Opal Growth," no. 20: 4701–4. doi:10.1021/LA990161K.

Meng, Q. B., C. H. Fu, Y. Einaga, Z. Z. Gu, A. Fujishima, and O. Sato. 2002. "Assembly of Highly Ordered Three-Dimensional Porous Structure with Nanocrystalline TiO2 Semiconductors." *Chemistry of Materials* 14 (1): 83–88. doi:10.1021/cm0101576.

Mihalcea, D, and P Piot. 2008. "Simulation of Field-Emission Cathodes for High Current Electron Injectors." *Linac*, 652–54.

Narasimhamorti, C C. 1995. "Self-aligned 6H-SiC MOSFETs with improved current drive" *Electronics Letters*. 31-14. doi: 10.1049/el:19950800

Nordheim, L W. 1928. "The Effect of the Image Force on the Emission and Reflexion of Electrons by Metals." *Proceedings of the Royal Society of London A: Mathematical, Physical and Engineering Sciences* 121 (788): 626–39. doi:10.1098/rspa.1928.0222.

P. N. Pusey, W. van Megen. 1987. "Observation of a Glass Transition in Suspensions of Spherical Colloidal Particles." *Physical Review Letters* 59 (18): 2083–86.

Pan, W. -S. 1990. "Reactive Ion Etching of SiC Thin Films by Mixtures of Fluorinated Gases and Oxygen." *Journal of The Electrochemical Society* 137 (1): 212. doi:10.1149/1.2086368.

Plank, N. Blauw, E. W. van der Drift, and R. Cheung. 2003. “The Etching of Silicon Carbide in Inductively Coupled SF 6 /O 2 Plasma.” *Journal of Physics D: Applied Physics* 36 (5): 482. http://stacks.iop.org/0022-3727/36/i=5/a=310.

Podenok, S., M. Sveningsson, K. Hansen, and E. E. B. Campbell. 2006. “Electric Field Enhancement Factors around a Metallic, End-Capped Cylinder.” *Nano* 1 (1): 87–93. doi:10.1142/S1793292006000112.

Ramsdell, Lewis. 1946. “Studies on Silicon Carbide.” *University of Michigan Official Publication*.

Rogach, L, N. Kotov, D. Koktysh, J. Ostrander, and G Ragoisha. 2000. “Electrophoretic Deposition of Latex-Based 3D Colloidal Photonic Crystals : A Technique for Rapid Production of High-Quality Opals Electrophoretic Deposition of Latex-Based 3D Colloidal Photonic Crystals : A Technique for Rapid Production of.” *Chemistry of Materials*, no. 16: 2721–26. doi:10.1021/cm000274l.

Rybczynski, J., U. Ebels, and M. Giersig. 2003. “Large-Scale, 2D Arrays of Magnetic Nanoparticles.” *Colloids and Surfaces A: Physicochemical and Engineering Aspects* 219 (1–3): 1–6. doi:10.1016/S0927-7757(03)00011-6.

S. Bhattacharya, A. Datta, J. M. Berg, and S. Gangopadhyay. 2005. “Studies on Surface Wettability of Poly (Dimethyl) Siloxane (PDMS) and Glass Under Oxygen-Plasma.” *J.MicroElecMechSys* 14 (3): 590–97. doi:10.1109/JMEMS.2005.844746.

Saito, Y. 2010. *Carbon Nanotube and Related Field Emitters: Fundamentals and Applications*. Wiley. https://books.google.com.tr/books?id=s8Nhe1wMq7QC.

Saito, Yahachi, and Sashiro Uemura. 2000. “Field Emission from Carbon Nanotubes and Its Application to Electron Sources.” *Carbon* 38 (2): 169–82. doi:10.1016/S0008-6223(99)00139-6.

Schreiner, R., F. Dams, C. Prommesberger, B. Bornmann, P. Serbun, A. Navitski, and G. Muller. 2011. “Silicon-Based Integrated Field Emission Electron Sources for Sensor Application.” *2011 24th International Vacuum Nanoelectronics Conference*, 19–20.7

Seong, Han-Kyu, Heon-Jin Choi, Sang-Kwon Lee, Jung-Il Lee, and Doo-Jin Choi. 2004. "Optical and Electrical Transport Properties in Silicon Carbide Nanowires." *Applied Physics Letters* 85 (7): 1256. doi:10.1063/1.1781749.

Shen, Guozhen, Yoshio Bando, Changhui Ye, Baodan Liu, and Dmitri Golberg. 2006. "Synthesis, Characterization and Field-Emission Properties of Bamboo-like β-SiC Nanowires." *Nanotechnology* 17 (14): 3468–72. doi:10.1088/0957-4484/17/14/019.

Sheppard, T, M. Melloch, and J. Cooper. 1996. "Experimental Demonstration of a Buried- Charge-Coup1e : D Device in 6H Silicon Carbide." *IEEE Electron Device Letters* 17 (1): 17–19. doi: 10.1109/55.475559.

Shur, M, S. Rumyantsev, and Levinshte. 2005. *SiC Materials and Devices*. ISBN 9812703837

Slater, D.B., Jr., G.M. Johnson, L. Lipkin, V. Suvorov, and J.W. Palmour. 1996. "Demonstration of a 6H-SiC CMOS Technology." *1996 54th Annual Device Research Conference Digest* 1 (919): 162–63. doi:10.1109/DRC.1996.546421.

So, Myeong S., Seung-Gu Lim, and Thomas N. Jackson. 1999. "Fast, Smooth, and Anisotropic Etching of SiC Using SF6/Ar." *Journal of Vacuum Science & Technology B: Microelectronics and Nanometer Structures* 17 (5): 2055–57. doi:10.1116/1.590871.

Solymar, L, and D Walsh. 2009. *Electrical Properties of Materials*. OUP Oxford. ISBN: 978-0-19-870277-1.

Stratton, R. 1955. "Field Emission from Semiconductors." *Proceedings of the Physical Society. Section B* 68 (10): 746. doi:10.1088/0370-1301/68/10/307.

———. 1962. "Theory of Field Emission from Semiconductors." *Physical Review* 125 (1). https://doi.org/10.1103/PhysRev.125.67

Sze, S M. 1981. *Physics of Semiconductor Devices*. Wiley-Interscience Publication. John Wiley & Sons. doi: 10.1002/0470068329.

Uemura, S., J. Yotani, T. Nagasako, H. Kurachi, H. Yamada, T. Ezaki, T. Maesoba, et al. 2003. "Carbon Nanotube Emitters for Field Emission Displays."

IEEE/CPMT/SEMI. 28th International Electronics Manufacturing Technology Symposium (Cat. No.03CH37479). doi:10.1109/IVMC.2003.1222976.

Valiev, K.A. 2013. *The Physics of Submicron Lithography*. Vol. 53. doi:10.1017/CBO9781107415324.004.

Vibrans, Gerwig E. 1964. “Vacuum Voltage Breakdown as a Thermal Instability of the Emitting Protrusion.” *Journal of Applied Physics* 35 (10): 2855–57. doi:10.1063/1.1713118.

Wang, J. J., E. Lambers, S. Pearton, and M. Ostling. 1998. “Inductively Coupled Plasma Etching of Bulk 6H-SiC and Thin-Film SiCN in NF3 Chemistries.” *Journal of Vacuum Science & Technology A: Vacuum, Surfaces, and Films* 16 (4): 2204. doi:10.1116/1.581328.

Wang, Xudong, Jun Zhou, Changshi Lao, Jinhui Song, Ningsheng Xu, and Zhong L. Wang. 2007. “In Situ Field Emission of Density-Controlled ZnO Nanowire Arrays.” *Advanced Materials* 19 (12): 1627–31. doi:10.1002/adma.200602467.

Weekes, Shemaiah M., Feodor Y. Ogrin, William A. Murray, and Paul S. Keatley. 2007. “Macroscopic Arrays of Magnetic Nanostructures from Self-Assembled Nanosphere Templates.” *Langmuir* 23 (3): 1057–60. doi:10.1021/la061396g.

Williams, Logan T., Victor S. Kumsomboone, W. Jud Ready, and Mitchell L R Walker. 2010. “Lifetime and Failure Mechanisms of an Arrayed Carbon Nanotube Field Emission Cathode.” *IEEE Transactions on Electron Devices* 57 (11): 3163–68. doi:10.1109/TED.2010.2069563.

Wu, Renbing, Kun Zhou, Jun Wei, Yizhong Huang, Fei Su, Jianjun Chen, and Liuying Wang. 2012. “Growth of Tapered SiC Nanowires on Flexible Carbon Fabric: Toward Field Emission Applications.” *Journal of Physical Chemistry C* 116: 12940–45. doi:10.1021/jp3028935.

Wu, Z. S., S. Z. Deng, N. S. Xu, Jian Chen, J. Zhou, and Jun Chen. 2002. “Needle-Shaped Silicon Carbide Nanowires: Synthesis and Field Electron Emission Properties.” *Applied Physics Letters* 80 (20): 3829–31. doi:10.1063/1.1476703.

Xianqi, W E I, L I Xin, L I U Weihua, and Wang Xiaoli. 2014. “Laser Tuned Field Emission of the Carbon Nanotube Arrays Grown on an Optical Fiber” 57 (10): 1936–40. doi:10.1007/s11431-014-5630-1.

Xu, Jinzhuo, Rong Pan, Yiwei Chen, Xianqin Piao, Min Qian, Tao Feng, and Zhuo Sun. 2013. “Electron Field Emission from Screen-Printed graphene/DWCNT Composite Films.” *Journal of Alloys and Compounds* 551. Elsevier B.V.: 348–51. doi:10.1016/j.jallcom.2012.10.095.

Yang, T. H., C. H. Chen, A. Chatterjee, H. Y. Li, J. T. Lo, C. T. Wu, K. H. Chen, and L. C. Chen. 2003. “Controlled Growth of Silicon Carbide Nanorods by Rapid Thermal Process and Their Field Emission Properties.” *Chemical Physics Letters* 379 (1–2): 155–61. doi:10.1016/j.cplett.2003.08.001.

Yang, Yajun, Guowen Meng, Xianyun Liu, Lide Zhang, Zheng Hu, Chengyu He, and Yemin Hu. 2008. “Aligned SiC Porous Nanowire Arrays with Excellent Field Emission Properties Converted from Si Nanowires on Silicon Wafer.” *Journal of Physical Chemistry C* 112 (51): 20126–30. doi:10.1021/jp809359v.

Yesilpinar Damla, and Celebi Cem 2017. "Electron Field Emission from SiC Nanopillars Produced by Nanosphere Lithography." *Journal of Vacuum Science & Technology B, Nanotechnology and Microelectronics: Materials, Processing, Measurement, and Phenomena* 35, 041801 (2017); doi: 10.1116/1.4989853

Yih, P H, V Saxena, and A J Steckl. 1997. “A Review of SiC Reactive Ion Etching in Fluorinated Plasmas.” *Physica Status Solidi (B)* 202 (1). WILEY-VCH Verlag: 605–42. doi:10.1002/1521-3951(199707)202:1

Zeng, Qinghua, Aibing Yu, and Gaoqing Lu. 2010. “Evaluation of Interaction Forces between Nanoparticles by Molecular Dynamics Simulation.” *Industrial and Engineering Chemistry Research* 49 (24): 12793–97. doi:10.1021/ie101751v.

Zhang, Hui, Dong Hoon Shin, Heon Sang Lee, and Cheol Jin Lee. 2007. “High-Quality Single-Walled Carbon Nanotubes Synthesized by Catalytic Decomposition of Xylene over Fe-Mo / MgO Catalyst and Their Field Emission Properties.” *Society*, 12954–59.

Zhang, Xinni, Youqiang Chen, Zhipeng Xie, and Weiyou Yang. 2010. “Shape and Doping Enhanced Field Emission Properties of Quasialigned 3C-SiC Nanowires.” *The Journal of Physical Chemistry C* 114 (18): 8251–55. doi:10.1021/jp101067f.

Zhang, Y. J., W. Li, and K. J. Chen. 2008. “Application of Two-Dimensional Polystyrene Arrays in the Fabrication of Ordered Silicon Pillars.” *Journal of Alloys and Compounds* 450 (1–2): 512–16. doi:10.1016/j.jallcom.2006.11.184.

Zhou, W. M., Y. J. Wu, Eric Siu Wai Kong, F. Zhu, Z. Y. Hou, and Y. F. Zhang. 2006. “Field Emission from Nonaligned SiC Nanowires.” *Applied Surface Science* 253 (4): 2056–58. doi:10.1016/j.apsusc.2006.03.088.

Zhou, X.T., H.L. Lai, H.Y. Peng, Frederick C.K. Au, L.S. Liao, N. Wang, I. Bello, C.S. Lee, and S.T. Lee. 2000. “Thin β-SiC Nanorods and Their Field Emission Properties.” *Chemical Physics Letters* 318 (1–3): 58–62. doi:10.1016/S0009-2614(99)01398-6.

Zhu, Jixiang, Min Li, R Rogers, and W Meyer. 1997. “Crystallization of Hard-Sphere Colloids in Microgravity.” *Nature* 387 (June): 883–85. doi:10.1038/43141.

Zhu, W. 2001. *Vacuum Microelectronics*. A Wiley-Interscience Publication. Wiley. ISBN: 978-0471322443 pp.73-80.